Doctoral Thesis

Structural Modification of Isoindigo-based Conjugated Materials towards Optoelectronic Applications

Gyoungsik Kim

Department of Energy Engineering

Graduate School of UNIST

2016

Structural Modification of Isoindigo-based Conjugated Materials towards Optoelectronic Applications

Gyoungsik Kim

Department of Energy Engineering

Graduate School of UNIST

Structural Modification of Isoindigo-based Conjugated Materials towards Optoelectronic Applications

A dissertation
submitted to the Graduate School of UNIST
in partial fulfillment of the
requirements for the degree of
Doctor of Philosophy

Gyoungsik Kim

01. 13. 2016 of submission
Approved by

Advisor
Changduk Yang

Structural Modification of Isoindigo-based Conjugated Materials towards Optoelectronic Applications

Gyoungsik Kim

This certifies that the dissertation of Gyoungsik Kim is approved.

01. 13. 2016 of submission

Advisor: Changduk Yang

Jin Young Kim: Thesis Committee Member #1

Kwanyong Seo: Thesis Committee Member #2

Ji Seok Lee: Thesis Committee Member #3

Joon Hak Oh: Thesis Committee Member #4;

Abstract

Organic semiconductors have attracted significant attention due to their potential for easy fabrication, light weight, low cost, and better compatibility with the solution and roll-to-roll processes for making flexible large area devices such as organic photovoltaics (OPVs) and organic field-effect transistors (OFETs). Moreover, many attempts have been made to design and synthesize state-of-the-art organic semiconductors to enhance device performance. Nowadays, almost all active materials of organic semiconductors are based on π-conjugated molecular backbones synthesized by cross-coupling reaction methodologies.

Recently, organic dyes have emerged as high-performance conjugated materials that have strong electron-withdrawing characters, intermolecular interaction, good planarity, relatively reduced energy band gaps, and high charge carrier transports. However, the confident performance in exceeds of inorganic semiconductors is the most important requirement for enabling the realization of the aforementioned near-future products.

Here, a synthesis method for the structural modification of isoindigo (IIG)-based conjugation materials (e.g., *counterpart*, *thiophene-implanted thienoisoindigo* (TIIG), and *side-chain*) and their optoelectronic applications are introduced.

First, I present *n*-type charge carrier transports *via* IIG-based acceptor-acceptor (A-A type) copolymers, which can be extended to the design of new *n*-type materials. In addition, the implantation of heteroaromatic spacers into the A-A type copolymer makes donor-acceptor alternating copolymers for the polarity tuning of the OFETs.

In the second part, TIIG alternate naphthalene copolymers are synthesized for *p*-type OFETs. The TIIG copolymers exhibit the highest *p*-type charge carrier mobility and a unique crystalline orientation.

Finally, non-ionic phosphonate side-chains combined with IIG copolymers are synthesized to improve inverted OPVs, improving power conversion efficiency compared to without modified copolymers.

This is a promising method for either the modification of IIG-based organic semiconducting materials or the enhancement of organic optoelectronics.

Contents

List of Figure

transistor operating in {(a),(c)} hole- and {(b),(d)} electron-enhancement mode at $|V_{DS}|$=100V, respectively.

Figure 2.2.7. FET characteristics obtained from spacer-tuned BT polymer films annealed at 220 °C. Transfer curves of {(a),(b)} PIIG-DTBT and {(c),(d)} PIIG-DSeBT films at {(a),(c)} hole-, {(b),(d)} electron-enhancement operation with V_{DS} = −100 and +100 V, respectively. Output curves of {(e),(f)} PIIG-DTBT and {(g),(h)} PIIG-DSeBT films at {(e),(g)} *p*-, {(f),(h)} *n*-channel operation, respectively.

Figure 2.2.8. (a) Schematic of the complementary inverter structure. CMOS-like inverter characteristics of (b) PIIG-DTBT and (c) PIIG-DSeBT inverter (V_{DD} = 100 V).

Figure 3.1. Chemical structure, Ultraviolet absorption spectra, Energy-level diagrams, and Energy-minimized structure at the B3LYP/6-31G** level. a, Structure of PTIIG-Np. (b) Normalized ultraviolet-visible absorption spectra of PTIIG-Np in $CHCl_3$ solution and as a thin film on quartz substrate. c, HOMO and LUMO levels determined by the thin films using cyclic voltammetry (CV) calibrated by the Fc/Fc^+ redox couple as an external standard. IP was also measured by ultraviolet photoelectron spectroscopy (UPS) technique. d, DFT-optimized geometries and charge-density isosurfaces for the trimeric system with a visualization of the HOMO and LUMO molecular orbitals (green and red represent the isosurfaces (iso value = 0.02) of the opposite phase of the wave functions). e, Calculated dihedral angles of the trimer structure.

Figure 3.2. Device geometry of solution-processed PTIIG-Np TFTs and their electrical characteristics. a, Schematic cross-section of the top-gate and bottom-contact (TG-BC) geometry and the chemical structures of PMMA and P(VDF-TrFE) (as the gate dielectric layer. b,c, Transfer curves of PTIIG-Np devices with PMMA dielectric at -100 V of V_{DS} (channel width (W): 1 mm, length (L): 20 μm), of which semiconductor films were annealed at different temperatures (b) and hole and electron charge carrier mobility distributions based on various annealing temperatures (c). d,e, Transfer (d) and output (e) characteristics for PTIIG-Np TFTs after thermal annealing at 310 °C with P(VDF-TrFE) gate insulator (channel width (W): 1 mm, length (L): 50 μm), where the devices were additionally cured at 160 °C after spin-coating of the gate dielectric layer on the top of semiconductor surface, in order to suppress the crystalline β-phase induced by the large ferroelectric properties.

Figure 3.3. Electrical characteristics of solution-processed PIIG-Np TFTs with PMMA dielectric. a, hole and electron mobility distributions based on various annealing temperatures. b, Threshold voltage (V_{th}) distributions. c, Channel width normalized *p*-channel contact resistance (R_cW) values, which was derived from a Y-function method, depending on the thermal-annealing temperatures of PIIG-Np. d, The transfer characteristics for PIIG-Np devices at -100 V of V_{DS} (channel length (L): 20 μm, width (W): 1 mm).

Figure 3.4. Optical and electrochemical properties and DFT calculated structure at the B3LYP/6-31G** level. a, Normalized ultraviolet–visible absorption spectra of PIIG-Np in $CHCl_3$ solution and as a thin film on quartz substrate. b, HOMO and LUMO levels determined by the thin film using cyclic voltammetry (CV) that calibrated by the Fc/Fc^+ redox couple as an external standard. c, Calculated dihedral angles of the trimer structure.

Figure 3.5. XRD patterns of P(VDF-TrFE) layer depending on annealing temperatures (80, 160, and 200 °C). The upper inset indicates the chemical structure of P(VDF-TrFE).

Figure 3.6. Microstructure analysis of PTIIG-Np. GIXD profiles and AFM images of solution-processed PTIIG-Np films annealed at 310 °C. a,b, GIXD image (a) and pattern (out-of plane) (b) of thin films (Inset is the corresponding in-plane GIXD pattern). c, AFM height (top) and phase (bottom) images. d,e, The local GIXD diffraction data ranged from -0.5 to 0.5 $Å^{-1}$ in q_{xy} and from 0 to 0.5 $Å^{-1}$ in

2.34 nm of PIIGDT-P5; (c) 8.18 nm, (g) 2.26 nm of PIIGDT-P15; (d) 11.14 nm, (h) 2.43 nm of PIIGDT-P30.

List of Schemes

List of Table

Glossary of Abbreviations

A-A	Acceptor-acceptor
AFM	Atomic force microscopy
BHJ	Bulk-heterojunction
BT	2,1,3-Benzothiadiazole
CF	Chloroform
CV	Cyclic voltammetry
D-A	Donor-acceptor
DFT	Density Functional theory
DIO	1,8-Diiodooctane
DPE	Diphenylether
DT	Bithiophene
DTBT	Dithienylbenzothiadiazole
DSeBT	Diselenienylbenzothiadiazole
FF	Fill factor
GIXD	Grazing incident X-ray diffraction
GPC	Gel-permeation chromatography
HOMO	Highest occupied molecular orbital
ICT	Intramolecular charge transfer
IIG	Isoindigo
IPCE	Incident photon-to-electron conversion efficiency
ITO	Indium tin oxide
$\boldsymbol{J_{sc}}$	Short-circuit current
LUMO	Lowest unoccupied molecular orbital
Mn	Number-averaged molecular weight
NMR	Nuclear magnetic resonance
Np	Naphthalene
***o*-DCB**	*o*-Dichlorobenzene
OFETs	Organic field-effect transistors
OTS	*n*-Octadecyltrimethoxysilane
PMMA	Poly(methyl methacrylate)
$PC_{71}BM$	[6,6]-Phenyl C_{71}-butyric acid methyl ester
PCE	Power conversion efficiency
PDI	Polydispersity index
PSCs	Polymer solar cells

P(VDF-TrFE)	Poly(vinylidenefluoride-trifluoroethylene)
SCLC	Space-charge-limited current
TCB	Trichlorobenzene
TG-BC	Top-gate and bottom-contact
THF	Tetrahydrofuran
TIIG	Thienoisoindigo
TPD	Thieno[3,4-*c*]pyrrole-4,6-dione
V_{oc}	Open-circuit voltage
XRD	X-ray diffraction

Chapter 1 Introduction

1.1 Organic Semiconductors

Organic semiconductors, including small molecules and polymers, have attracted significant attention due to their advantages, such as easy fabrication, low cost, flexibility, and large area via the solution process.[1-5] Since the properties of polyaniline were unveiled through anodic oxidation under acidic conditions by Letheby's, significant research progress has been reported due to efforts to find new materials with high efficiency in charge transport. Shirakawa, MacDiarmid, and Heeger investigated oxidized and iodine-doped polyacetylene to exhibit high conductivity with the simple structures in a π-conjugated system of polyacetylene and produce a successful explanation of the insertion of doping concept,[6] resulting in the subsequent development of conducting polymers. They were rewarded with the 2000 Nobel Prize in chemistry "for the discovery and development of electrically conductive polymers." Following the conjugation concepts they discovered, π-conjugated systems in which π-electrons are delocalized along the connected p_z-orbitals of continuous sp^2-hybridized carbon atoms should be composed of alternating single and multi-bonds (double and triple bonds) in the polymer backbones. In addition, the heteroatoms in the carbon-only materials are well known to be beneficial due to their efficient charge-transporting properties in conjugated compounds, such as polyfluorene, polyphenylene, polycarbazole, polypyrrole, poly(*p*-phenylene vinylene), poly(3,4-ethylenedioxythiophene), polyacetylene, polyaniline, and polythiophene (see Figure 1.1.1 and Table 1.1.1).[7] Many π-conjugated organic semiconductors have been thoroughly studied to date and opened up huge possibilities for a variety of electronic applications, such as organic light-emitting diodes (OLEDs),[8-13] organic photovoltaic cells (OPVs),[3,14,15] and organic field-effect transistors (OFETs).[16-18] Organic semiconductors operate like inorganic semiconductors with similar conduction for the charge-transfer mechanisms in π-conjugated systems. As follow the mechanisms, electrons can move through overlapped π-electron clouds by a hopping and tunneling process.[19] In common organic semiconductors with no dominant orientation of molecular packing, in which there is a limitation of overlapping between π-bonds of molecules, conduction can be mainly attributed to the hopping of charge carriers, which depends on the energy gap between the highest occupied molecular orbital (HOMO) and lowest unoccupied molecular orbital (LUMO). Moreover, many key factors have important bearing on charge carrier mobility, including molecular packing, disorder, impurities, temperature, electric field, molecular weight, and so forth. In particular, molecular packing orientation in organic molecules is of great significance to the modification of energy barriers at molecular boundaries owing to their relatively weak intermolecular electronic couplings.

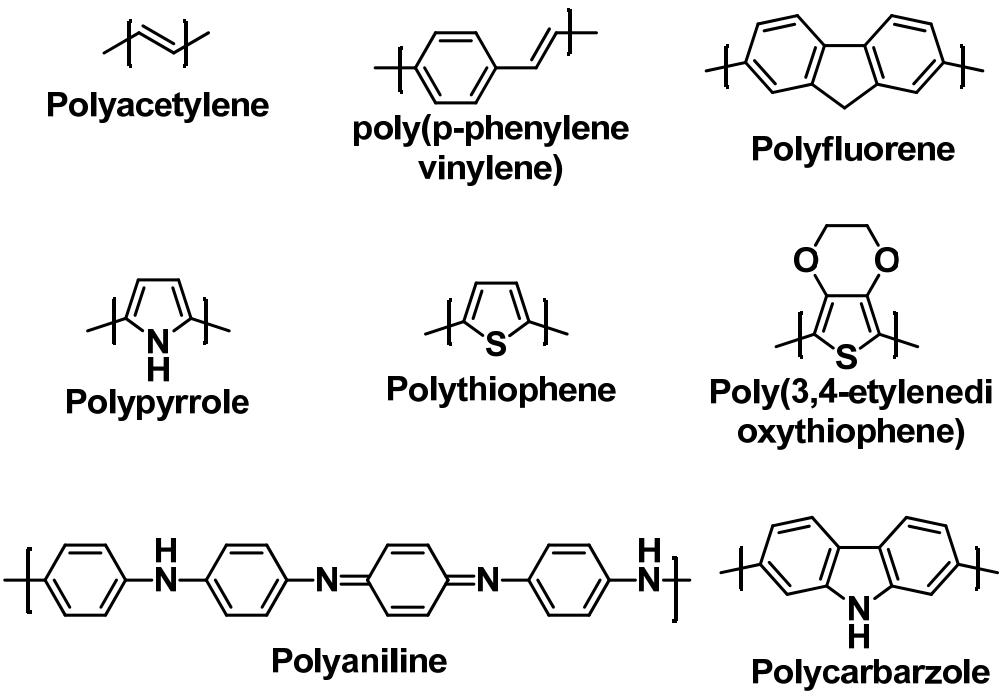

Figure 1.1.1. Chemical structure of semiconducting conjugated polymer

Table 1.1.1. Various polymer types by consist atom with main chain

Main chain contains	Heteroatoms present		
	No heteroatom	**Nitrogen-containing**	**Sulfur-containing**
Aromatic cycle	Polyfluorenes Polyphenylenes Polypyrenes Polyazulenes Polynaphthalenes	Polypyrroles Polycarbarzoles Polyindoles Polyazepines Polyanilines	Polythiophene Poly(3,4-etylenedioxythiophene) Poly(*p*-phenylene sulfide)
Double bond	Polyacetylene	-	-
Aromatic cycle and double bond	Poly(*p*-phenylene vinylene)	-	-

Over the past decade, many organic semiconductors have been developed for various optoelectric applications because of the above-mentioned advantages. Recently, organic dyes, such as isoindigo (IIG),[20,21] diketopyrrolopyrole (DPP),[22,23] naphtalenediimide (NDI),[24,25] have emerged as high-performance conjugated materials with strong electron-withdrawing characters, optical absorption, charge transport properties, solution processability, and stability. Each conjugated material has unique optical and electrochemical properties and is suitable for ubiquitous applications.

This chapter has provided a basic background of organic electronics and the methodologies of synthesizing organic semiconductors along with a short review of cross-coupling reactions and reaction mechanisms. Further, several advantages with electronic properties and promising examples of organic semiconductors based on IIG-based molecules were presented following from the various synthetic methods. Then, the theories for OPVs and OFETs are simply briefed and the representative cases with organic semiconductors based on the modification of IIG polymers are presented.

1.2 Palladium-catalyzed Aryl-Aryl Cross Coupling

1.2.1 Background

Aryl (Ar) group-based Ar-Ar cross-couplings were discovered with the development of organic semiconductors. In this regard, an understanding of coupling reactions is needed for various molecular designs and the synthesis of organic semiconductors. These coupling reactions are categorized into two classes: homo-coupling of only one compound (e.g., the conversion of 2-bromobenzene to biphenyl (Yamamoto coupling)) and cross-coupling of two or more different counterparts (e.g., bromobenzene and trimethyltin thiophene to make phenylthiophene (Stille coupling)). Based on the high level of strength required to form C-C and C-heteroatom bonds, various types of synthetic reactions for the coupling of organic conjugated materials have been devised and established with several conditions (see Table 1.2.1).[26,27] At present, palladium-, nickel-, and copper-based catalysts are often used in coupling reactions.[26,28] Heck, Negishi, and Suzuki developed a palladium-assisted coupling reaction, and they were awarded the Nobel Prize in chemistry in 2010 “for palladium-catalyzed cross-coupling in organic synthesis,” an immense contribution to coupling reactions.[28-30] Palladium-catalyzed coupling reactions are ideal for optoelectronic applications because of the ease with which organic semiconductors are synthesized.

1.2.2 Reaction Mechanism

Typically, palladium-catalyzed coupling reactions are initiated with the “oxidative addition” of organic halide (electrophile) to the palladium-based catalyst.[31] After that, the “transmetallation” and “reductive elimination” steps follow in order. (Figure 1.2.1) The process of increasing both the oxidation state and the coordination number of a centered metal is called “oxidative addition,” in which the reactivity of the leaving groups on the organic halides can control the rate of (order of

reactivity: I > OTf > Br >> Cl, alkenyl-OTf >> aryl-OTf, where OTf is the triflate group). Transmetallation is the transfer of a ligand from one metal to another part, which places both coupling counterparts on the same metal position. Finally, in reductive elimination, two coupling partners regenerate the catalyst and create the new-coupled fragments.

Table 1.2.1. Coupling reaction overview

Reaction	Year	Reactant A		Reactant B		Type	Catalyst	Remark
Wurtz reaction	1855	R-X	sp^3	R-X	sp^3	homo		Na
Glaser coupling	1869	RC≡CH	sp	RC≡CH	sp	homo	Cu	O_2
Ullmann reaction	1901	Ar-X	sp^2	Ar-X	sp^2	homo	Cu	
Gomberg-Bachmann reaction	1924	Ar-H	sp^2	Ar-N_2X	sp^2	homo		base
Cadiot-Chodkiewicz coupling	1957	RC≡CH	sp	RC≡CX	sp	cross	Cu	base
Castro-Stephens coupling	1963	RC≡CH	sp	Ar-X	sp^2	cross	Cu	
Gilman reagent coupling	1967	R_2CuLi		R-X		cross		
Cassar reaction	1970	Alkene	sp^2	R-X	sp^3	cross	Pd	base
Kumada coupling	1972	Ar-MgBr	sp^2, sp^3	Ar-X	sp^2	cross	Pd or Ni or Fe	
Heck reaction	1972	alkene	sp^2	R-X	sp^2	cross	Pd or Ni	base
Sonogashira coupling	1975	RC≡CH	sp	R-X	sp^3 sp^2	cross	Pd and Cu	base
Negishi coupling	1977	R-Zn-X	sp^3, sp^2, sp	R-X	sp^3 sp^2	cross	Pd or Ni	
Stille cross coupling	1978	R-SnR_3	sp^3, sp^2, sp	R-X	sp^3 sp^2	cross	Pd	
Suzuki reaction	1979	R-$B(OR)_2$	sp^2	R-X	sp^3 sp^2	cross	Pd or Ni	base
Hiyama coupling	1988	R-SiR_3	sp^2	R-X	sp^3 sp^2	cross	Pd	base
Buchwald-Hartwig reaction	1994	R_2N-H	sp	R-X	sp^2	cross	Pd	N-C coupling
Fukuyama coupling	1998	R-Zn-I	sp^3	RCO(SEt)	sp^2	cross	Pd	

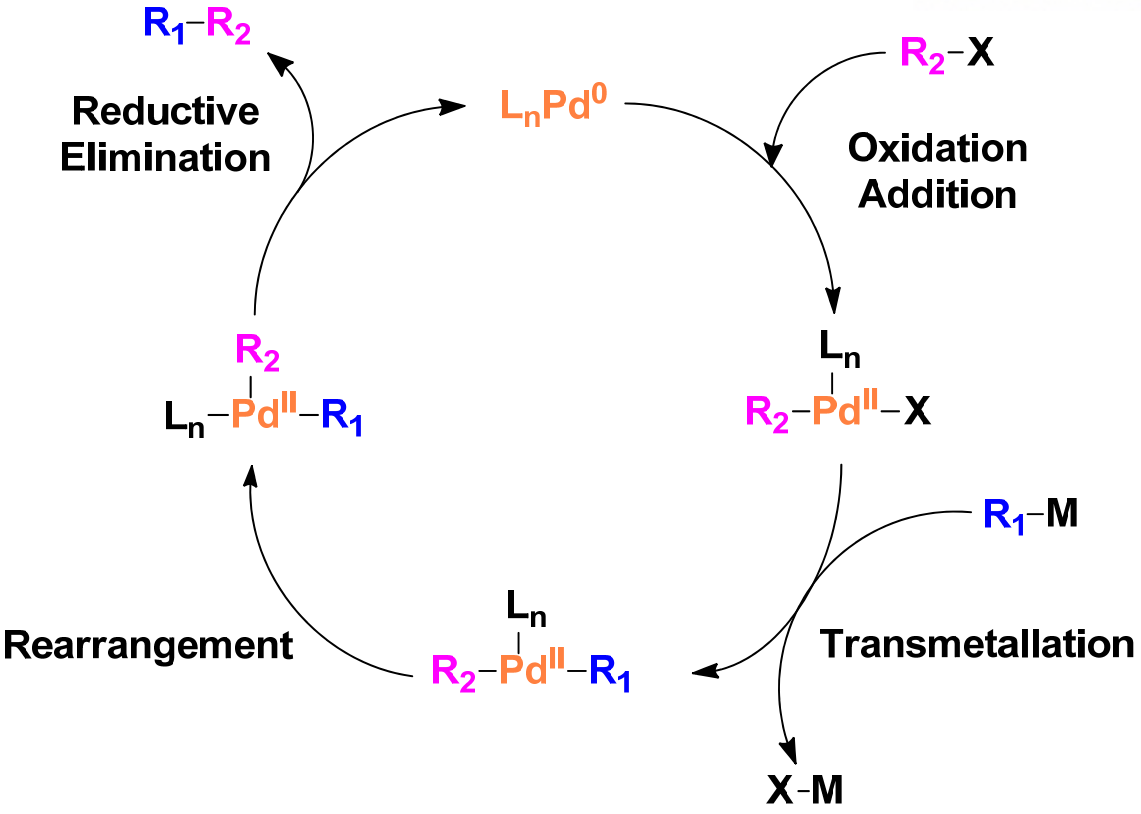

Figure 1.2.1. Typical palladium-catalyzed cross-coupling reaction mechanism.

1.2.3 Example of Coupling Reaction

This part simply introduces some coupling reactions, such as the Suzuki, Stille, Negishi, and Heck coupling reactions.

Suzuki Reaction

The Suzuki reaction (Suzuki-Miyaura reaction) was first announced in 1979 by Suzuki, and it involves cross-coupling of aryl boronic acid or boronic ester, such as organoboron species (R_1-BY_2), with aryl halide (R_2-X) in the basic condition with a palladium catalyst.[32-34] (Scheme 1.2.1) The Suzuki reaction generated a new carbon-carbon bond by removing the organoboron species and the halide atom. In the mechanism of Suzuki coupling, firstly, palladium (0) implants between the aryl halide to make organopalladium, which is called oxidative addition. After that, base chemicals with organopalladium are made intermediate. During the same process, organoboron reacts with the base reactant, which generates the boron-ate complex intermediate, and then the transmetallation with the boron-ate complex forms the organopalladium fragment. Reductive elimination of the desired product of the new carbon-carbon bond is performed, and the original palladium catalyst palladium (0) form is recovered, which completes the catalytic cycle. (Figure 1.2.2)

Scheme 1.2.1. Scheme of general Suzuki coupling reaction

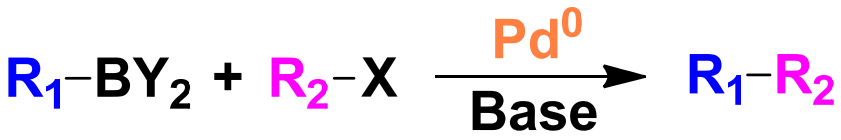

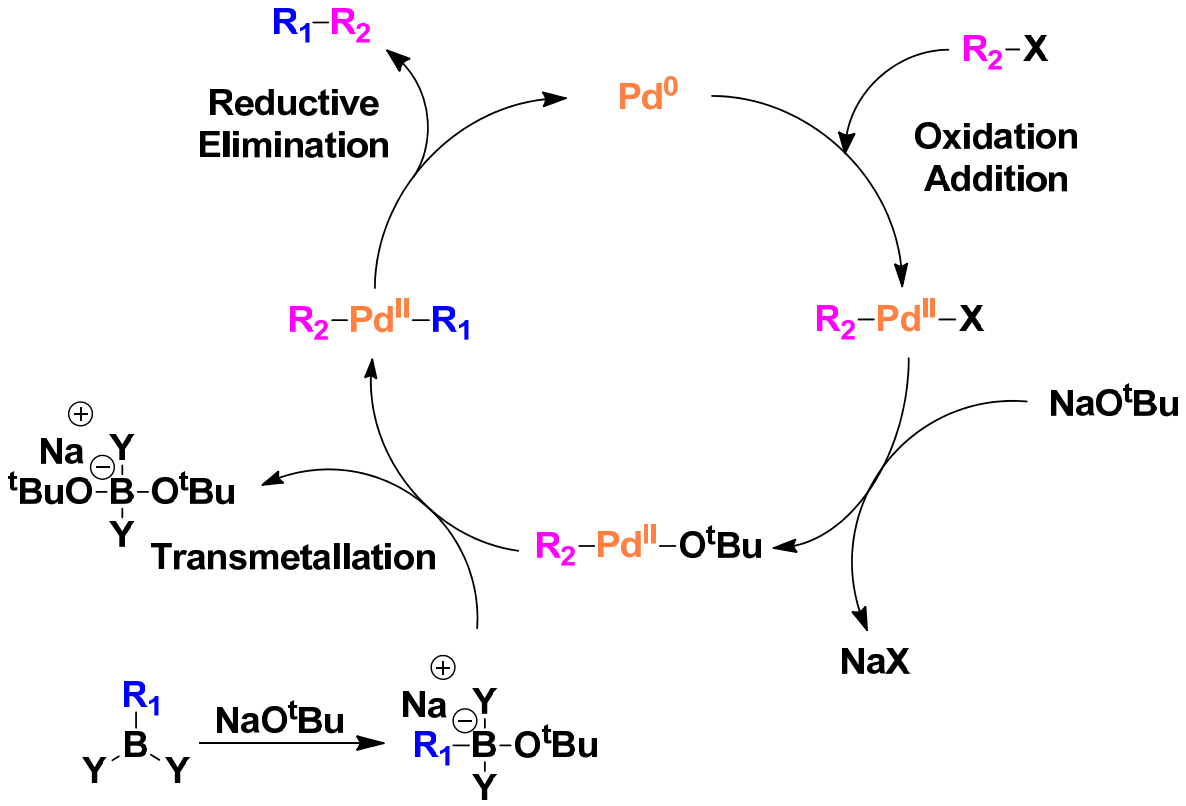

Figure 1.2.2. Schematic mechanism of Suzuki coupling reaction

The strength of Suzuki coupling over other coupling reactions include its higher reactivity, the availability of common organoboron compounds, the mild reaction conditions, and its less toxic nature.

Stille Coupling

The Stille coupling reaction (Migita-Kosugi-Stille coupling), first announced in 1979 by Suzuki and Milstein, occurs between organostannanes (R_1-SnR_3) with aryl halide (R_2-X) in the presence of a palladium (0) catalyst such as tetrakis(triphenylphosphine)palladium(0), ($Pd(pph_3)_4$), and

tris(dibenzylideneacetone)dipalladium(0) ($Pd_2(dba)_3$), which are broadly used in organic synthesis.[35-37] (Scheme 1.2.2) Stille coupling generates a new carbon-carbon bond by removing the organostannanes species and the halide atom.

The Stille coupling reaction usually progresses in a block of moisture and air, since oxygen causes the oxidation of palladium (0) and promotes unwanted organostannanes homo-coupling, leading to a decreased yield.[34,38] As organostannane reagents, a trialkylstannyl (trimethylstannyl and tributylstannyl) compound is commonly used, and these are known to be quite toxic organoreagents.

Scheme 1.2.2. Scheme of general Stille coupling reaction

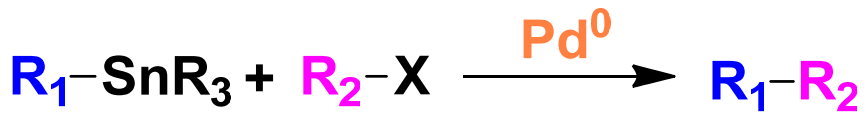

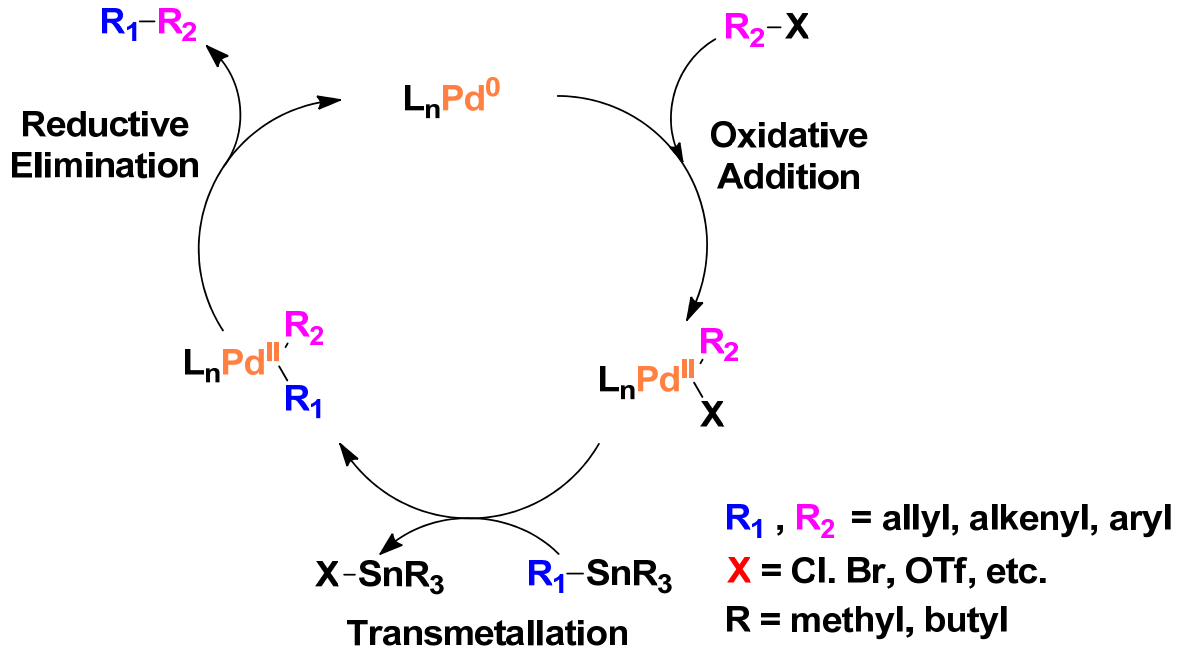

Figure 1.2.3. Schematic mechanism of Stille coupling reaction

The Stille coupling mechanism, a simple catalytic cycle, involves an oxidative addition, transmetallation, and reductive elimination. First, a palladium catalyst implants into the aryl halide or pseudohalide during the oxidative addition step, and these intermediates undergo transmetallation with the trialkylstannyl compound. Finally, the trialkylstannyl group produces the trialkylstannyl-halide complex byproduct and generates the new carbon-carbon bond. (Figure 1.2.3)

Negishi Coupling

Negishi coupling is broadly used with transition metal-catalyzed chemical reactions of organic halides or triflates with organozinc (ZnAr) compounds to make Ar-Ar fragments.[39] This coupling reaction, first reported in 1977 and leading to the Nobel Prize in Chemistry in 2010, generally uses palladium- and nickel-based organometallic catalysts. (Scheme 1.2.3)

Scheme 1.2.3. Scheme of general Negishi coupling reaction

The leaving groups X and X' consist of chloride, bromide, or iodide. The X group can use a triflate or acetyloxy group, and organozinc precursors of X' groups use chloride, bromide, or iodide. The organic compound R can be an alkenyl, aryl, allyl, or propargyl, and R' involves an alkenyl, aryl, allyl, alkyl benzyl, homoallyl, or homopropargyl. The metal M in the catalyst is palladium or nickel, and the ligand L_n in the catalyst can be triphenylphosphine, 1,2-bis(diphenylphosphino)ethane (dppe), 2,2'-bis(diphenylphosphino)-1,1'-binaphthyl (BINAP), or chiraphos to make a Pd(0) species. The reaction mechanism is described in Figure 1.2.4 and is composed of three steps: oxidative addition, transmetallation, and reductive elimination.

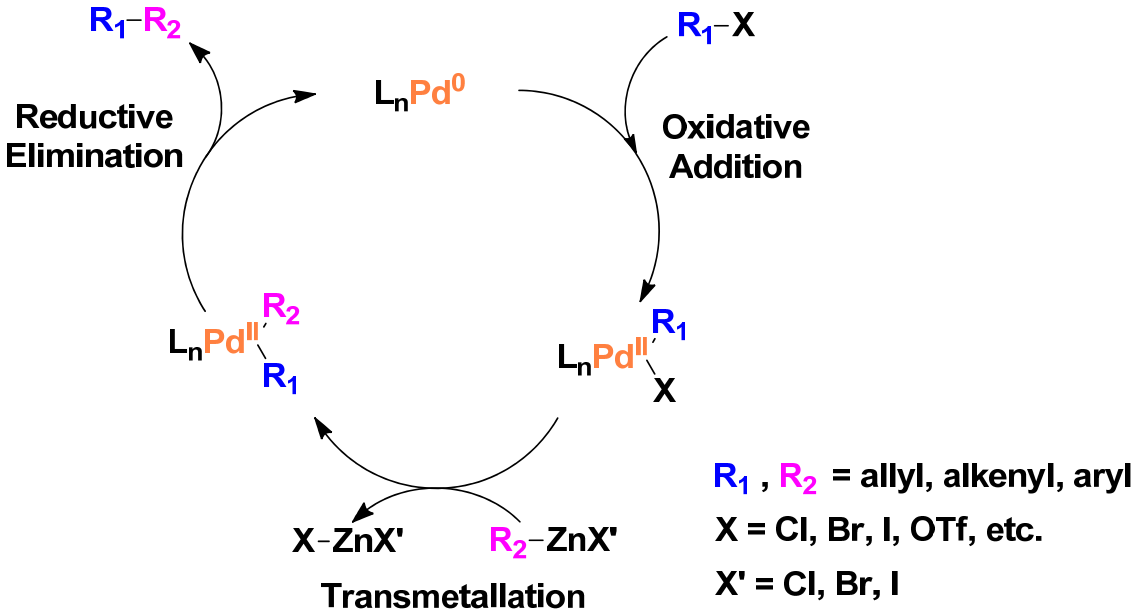

Figure 1.2.4. Schematic mechanism of Negishi coupling reaction

Heck Reaction

The Heck reaction (Mizoroki-Heck reaction) operates between the unsaturated halide or triflate with the alkene in the basic condition with a palladium catalyst.[40-43] A carbon-carbon bond was firstly formed by this coupling reaction, which follows a cycle similar to the Pd(0)/Pd(II) catalytic cycle seen in other Pd(0)-catalyzed cross-coupling reactions. The substitution reactions on planar sp^2-hybridized carbon atoms in the Heck reaction make this of great importance. (Scheme 1.2.4)

Scheme 1.2.4. Scheme of general Heck coupling reaction

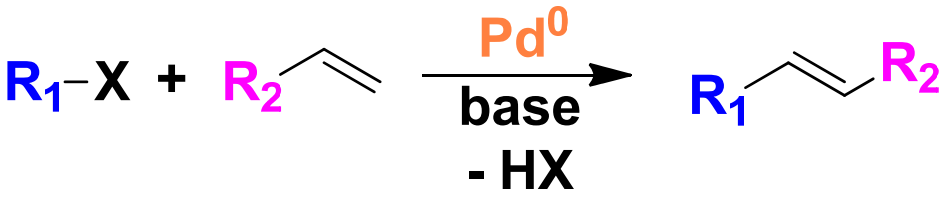

The catalytic cycle of the Heck reaction entails a series of transformations around the palladium catalyst, and the palladium (0) compound required in this cycle is generally prepared *in situ* from a palladium (II) precursor. When palladium (II) acetate ($Pd(OAc)_2$) is used as a catalyst, palladium (II) acetate is reduced by triphenylphosphine to bis(triphenylphosphine)palladium (0), and triphenylphosphine is oxidized to triphenylphosphine oxide. The palladium is implanted in the aryl to halide bond during oxidative addition, followed by the formation of a π-complex with the alkene. The insertion of alkene in the palladium-carbon bond by a *syn* addition is in the second place with a torsional strain-relieving rotation to the *trans* isomer. The beta-hydride elimination forms the product of a new palladium-alkene π-complex. This complex is destroyed in the next step in which the palladium (0) compound is regenerated by reductive elimination of the palladium (II) compound by potassium carbonate. Following the subsequent catalytic cycles, the palladium is truly a catalyst as only the catalytic amount is used, and the potassium carbonate is finally stoichiometrically consumed. (Figure 1.2.5)

1.3 Organic Semiconductors for Optoelectronic Application

1.3.1 Background

Organic optoelectronic devices are developed with the advantages of organic semiconductors, such as easy fabrication, low cost, flexibility, and large area via the solution process.[1-5] Inorganic semiconductors show superior performance in optoelectronic applications but have an intricate and expensive process, heavy weight, and brittle characteristic. Even so, the organic optoelectronic application field is growing explosively, because improvement possibility of performance, high cost-effective and solution of environmental problems.

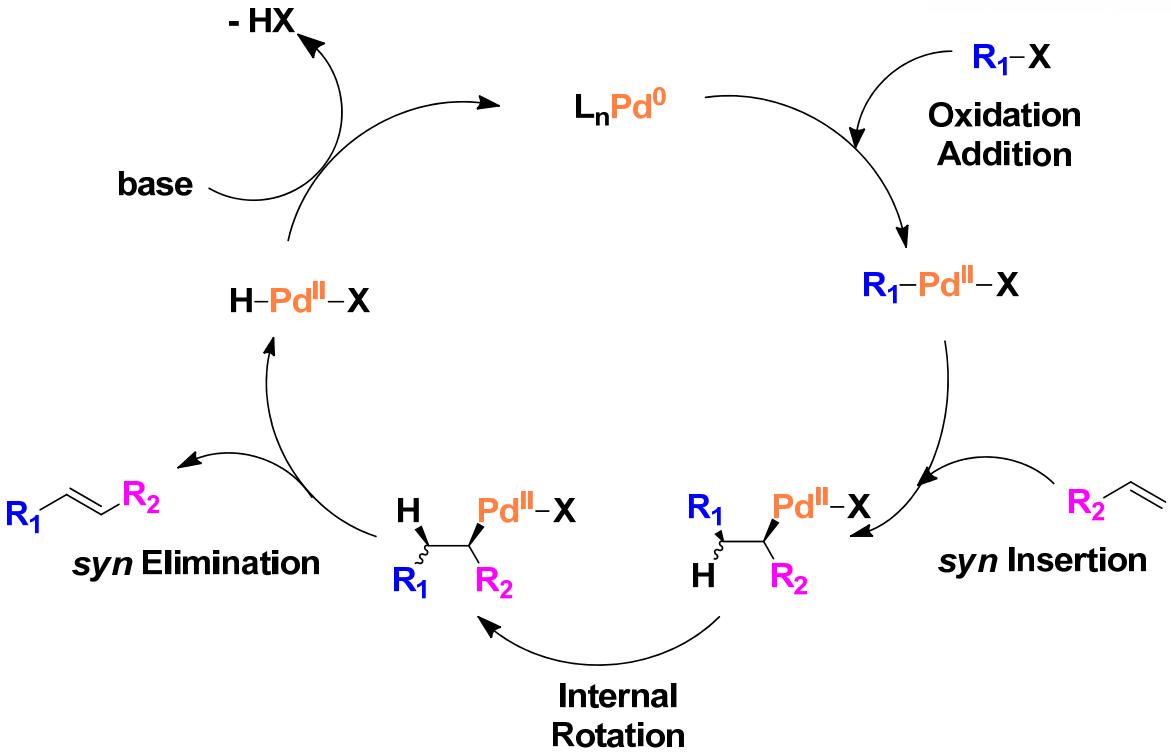

Figure 1.2.5. Schematic mechanism of Heck coupling reaction

This chapter briefly introduces the organic optoelectronic applications, such as OPVs and OFETs.

1.3.2 Organic Photovoltaics (OPVs)

Research Background

Today, almost all sources of energy use finite fossil fuels such as coal, natural gas, and oil, which is causing environmental problems. In addition, the disasters of the Fukushima nuclear plant and Chernobyl nuclear plant shocked the international community. Cleaner, stable, and cost-effective next-generation energy sources are needed, and OPVs are one such source.

The first OPV discovered by Tang in 1986 was a bilayer device consisting of copper phthalocyanine (CuPc) and a perylenetetracarboxylic derivative with an efficiency of 1%.[44] Successively, Sariciftci *et al*. proposed and demonstrated that C60-fullerene is a promising acceptor utilized with conjugated polymers to explain photo-induced electron transfer,[45] leading to the development of polymer-fullerene-based OPVs, and Yu *et al*. made new OPV devices by reporting a bulk-heterojunction (BHJ) structure that uses a blend of an electron-donor polymer and an electron-acceptor fullerene in 1994.[3] Recent years have witnessed the rapid advancement in the development of promising organic photoactive materials with very high power conversion efficiencies of OPVs.

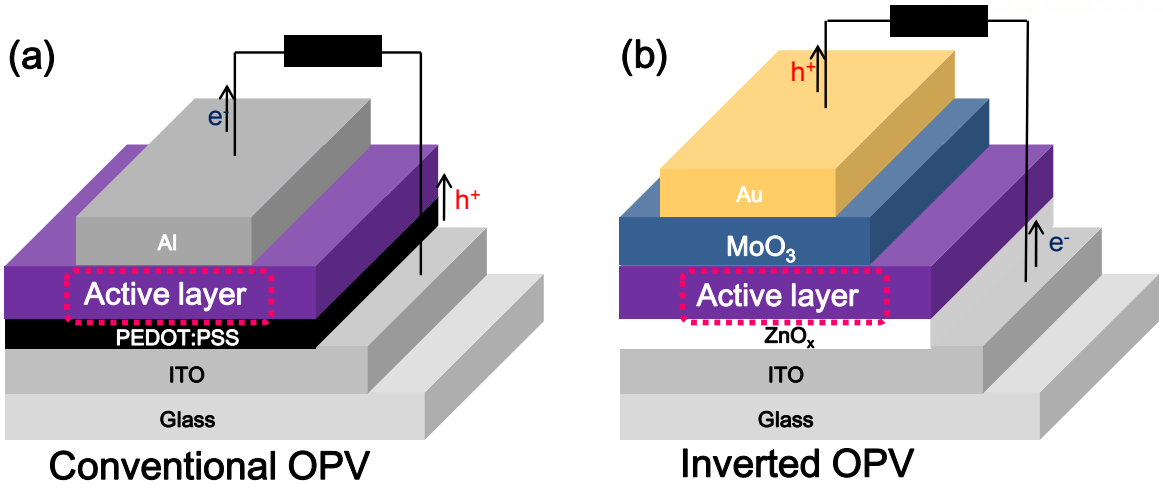

Figure 1.3.1. Schematic conventional (a) and inverted (b) of OPVs

Structure of BHJ-OPVs

In the case of BHJ-OPVs, device structures are divided into conventional and inverted structures. (Figure 1.3.1) Typically, conventional OPVs are comprised of a BHJ active layer sandwiched between an acidic poly(3,4-ethylenedioxythiophene):poly(styrenesulfonate)- (PEDOT: PSS-) coated indium tin oxide (ITO) anode and a low work-function metal cathode (e.g., Al and Ca). In such a device structure, not only are the cathodes easily oxidized in air but also the acidic PEDOT:PSS-ITO can suffer interfacial degradation over the operating lifetime.[46] As an alternative to the regular device configuration, PSCs with an inverted device structure have been developed, which enables the use of stable and printable high work-function metals (e.g., Ag and Au) as hole-collecting top electrodes and n-type low work-function metal oxides (e.g., TiO_x and ZnO) as electron-collecting bottom electrodes.[47,48] Thus, with the advances made on the aforementioned efficiency front, the lifetime and reliability of PSCs are also improved by utilizing the inverted PSC configuration through the replacement of the low work-function metal cathode and the elimination of the PEDOT:PSS layer.[49]

Principle of BHJ-OPVs

OPV operation can progress from sunlight to electricity in the following four steps:[50] (Figure 1.3.2)

(i) Light absorption (η_A)
(ii) Exciton diffusion (η_D)
(iii) Charge transport (η_{CT})
(iv) Collection of charge carriers (η_{CC})

The four-step process of OPVs is affected by the photovoltaic performance and external quantum

(EQE) of the device. The EQE can be calculated by the following equation:[51]

$$EQE = \eta_A \times \eta_D \times \eta_{CT} \times \eta_{CC}$$

(i) *Light absorption (η_A)*

Researchers have focused on and developed efficient semiconductors to broaden the absorption band of sunlight in several aspects: well-matched energy band gap between electron-donors and -acceptors, enhanced absorption coefficients, and optimized thickness of an active layer within 100 nm to avoid exciton recombination charge transport loss.

(ii) *Exciton diffusion (η_D)*

One of the factors determining the efficiency of exciton diffusion to a donor-acceptor interface is the exciton diffusion length (L_D) compared with the diffusion distance (L_i) between the photo-exciton location and donor-acceptor interface.[52] The distance, L_i, between them should be smaller than L_D; otherwise, the number of excitons will be generally decreased by radiative and non-radiative recombination.

(iii) *Exciton dissociation and charge transport (η_{CT})*

To dissociate the generated excitons into each electrode in the form of free holes and electrons, the minimum exciton binding energy (~0.3 eV)[53] should be overcome at the interface. This binding energy is determined from the offset of LUMO energy levels of donors and acceptors. Therefore, optimization of LUMO energy offsets and the internal electric field should be followed for the efficient dissociation of excitons. In addition, the charge transport efficiency (η_{CT}) indicates the number of transported free charges from the generated excitons.

(iv) *Collection of charge carriers (η_{CC})*

The charges transferred from the active layer to the electrodes are compared with the total free charges generated at the interface to transfer to the electrodes, the ratio of which is called the collection of charge carriers (η_{CC}). This indication significantly depends on the alignment between the energy level of the active layer and the work function of the electrodes.

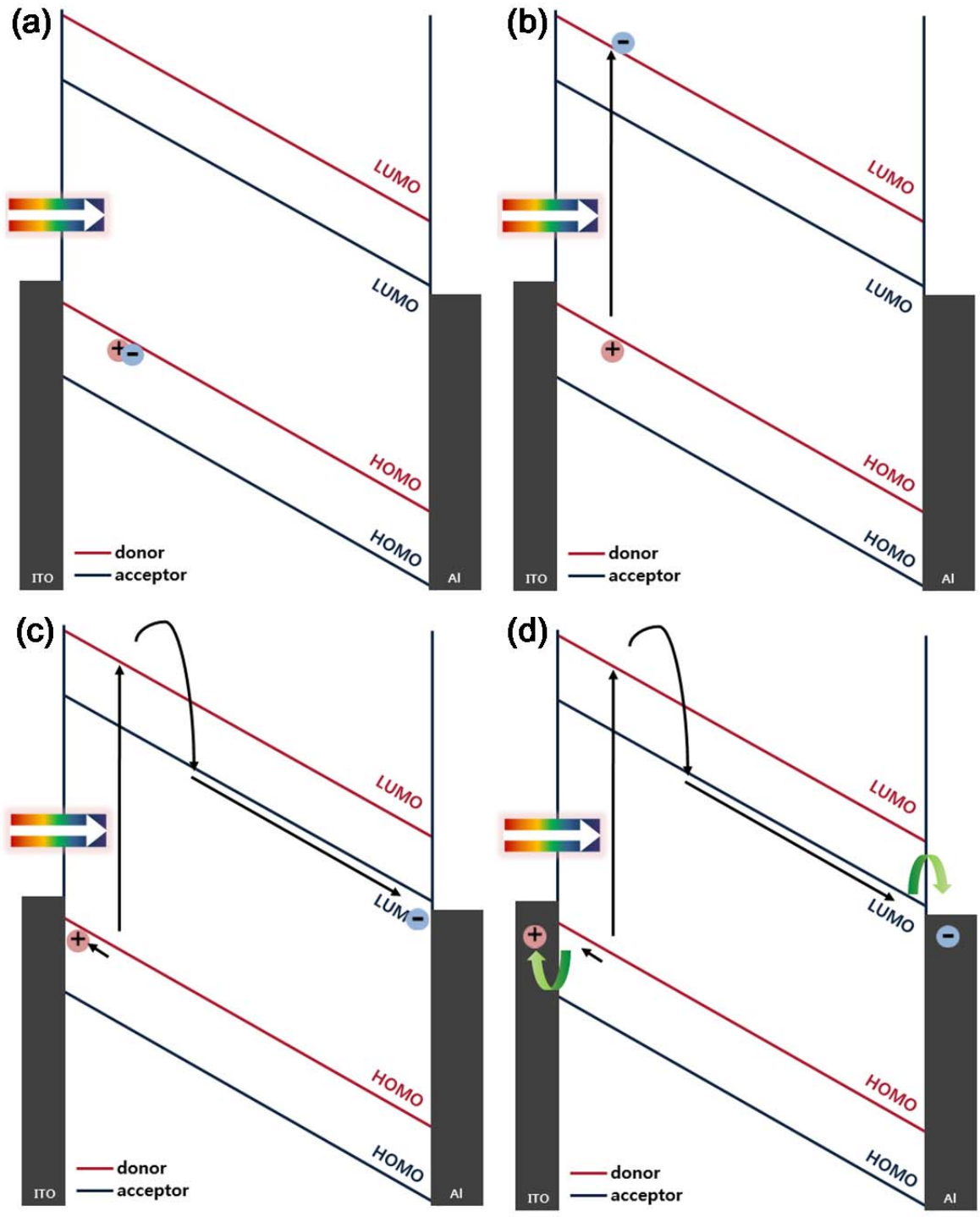

Figure 1.3.2. Operating mechanism of OPVs; (a) Light absorption, (b) Exciton diffusion (c) Charge transport and (d) Charge collection.

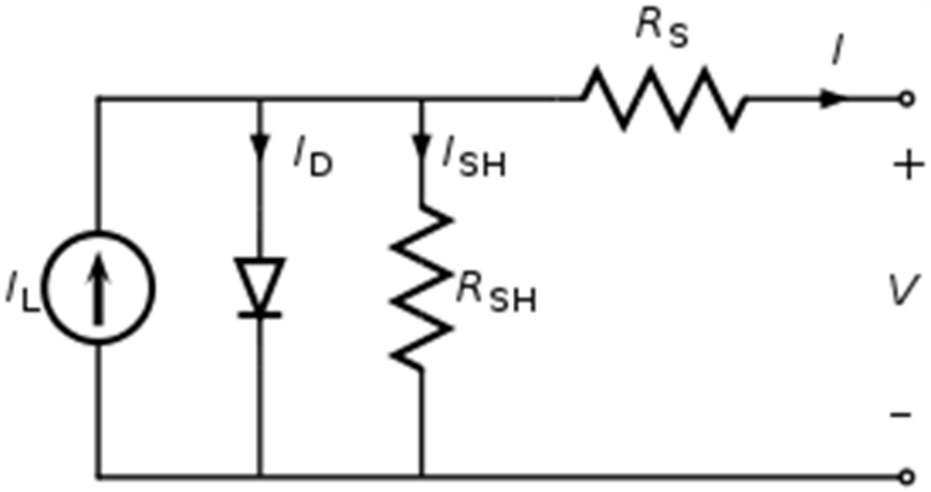

Figure 1.3.3. Equivalent circuit of a solar cell.

The power conversion efficiency (η) is calculated as shown in the given equation: η (%) = (J_{SC} × V_{OC} × *FF*) × 100 (%) / P_{in}, where P_{in} is the incident light power density, J_{SC} is the short-circuit current density determined by short-circuit conditions (V = 0), V_{OC} is the open-circuit voltage obtained when there is no external electric current flow between the terminals, and *FF* is determined by the ratio of its maximum power to the product of J_{SC} and V_{OC}. Each factor determining the efficiency in OPVs is related to the optical and electronic properties of organic semiconducting materials and device conditions; J_{SC} is influenced by the characteristics of light absorption in the photoactive organic materials and the thickness of each layer coated in electrodes.[54-58] V_{OC} is strongly decided by the difference in the energy levels between the HOMO of donors and LUMO of acceptors,[59,60] equated by: V_{OC} = (1/e)[|HOMO(donor)-LUMO(acceptor)| (eV) + Δ], where Δ is the exciton dissociation energy, 0.3 eV. *FF* is mainly demonstrated by the carrier mobility of active materials, shunt resistance (R_{SH}) originating from poor diode contact, and series resistance (R_S), which comes from contact and bulk semiconductors.[61] The *J*-*V* characteristics can be described by the following equation: $J = J_0[\exp(q(V-JR_SA))/(nkT) - 1] + (V-JR_SA))/(R_{SH}A) - J_{ph}$, where k is Boltzmann's constant, T is temperature, q is elementary charge, A is device area, n is the ideality factor of the diode, J_0 is reverse saturation current density, J_{ph} is photocurrent, R_S is series resistance, and R_{SH} is shunt resistance.[62]

1.3.3 Organic Field Effect Transistors (OFETs)

OFETs have received attention, as they have the same advantages as the other organic optoelectronic devices created in 1986 by Tsumura using polythiophene.[63] Unlike inorganic semiconductors, organic semiconductors can be readily modified and the charge transport and energy band gap can be optimized by changing the molecular design. OFETs operate with three electrodes (gate, source, and drain electrodes) in organic semiconductors, and an insulating layer (gate dielectric) is used between

the electrodes.[64] OFETs can be divided into four architectures based on electrode position structure: bottom-gate and top-contact (BG-TC), bottom-gate and bottom-contact (BG-BC), top-gate and top-contact (TG-TC), and top-gate and bottom-contact (TG-BC). (Figure 1.3.4) In this study, the OFET structure of focus is the BG-TC architecture with SiO_2 dielectric and TG-BC architectures with organic polymers,[65,66] such as poly(methyl methacrylate) and poly(vinylidene fluoride-trifluoroethylene),[67] as they have a high dielectric constant (k). In addition, newly synthesized organic semiconductors are applied to OFET devices.

Secondly, a TG-BC architecture can be made on an insulated substrate such as glass, and therefore, the organic semiconductor is coated on the glass substrate with lithographically patterned source and drain electrodes. After that, the insulator layer is coated on top of the prepared substrate. Finally, gate electrodes are thermally evaporated on top of the insulator layers to complete the TG-BC architecture.[67,71] The TG-BC architecture is especially suitable for printed transistors and insulators because of its self-encapsulation and improved environmental stability.

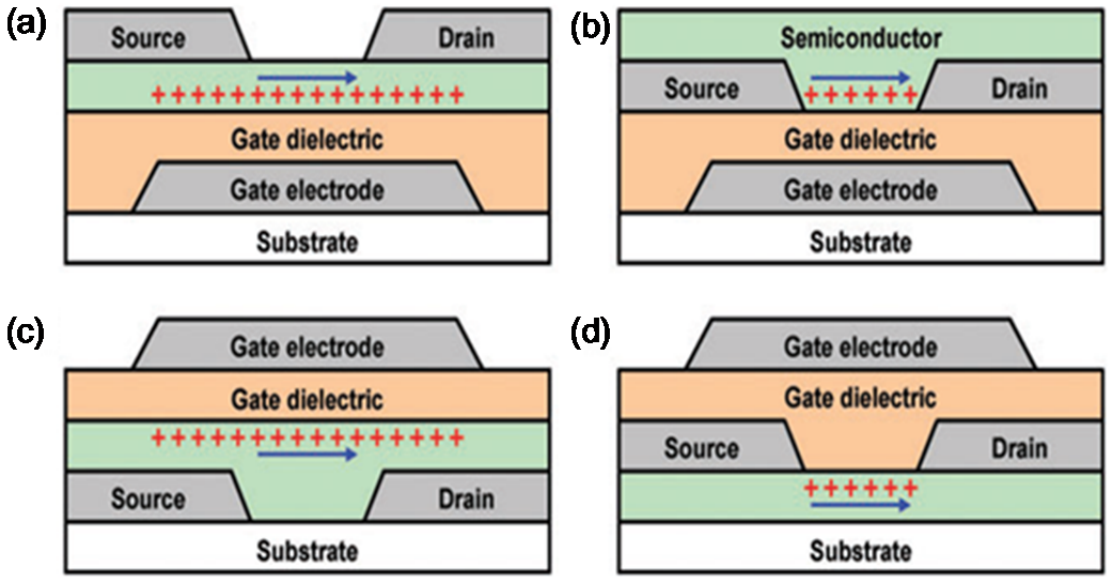

Figure 1.3.4. Schematic architectures of organic transistors. (a) bottom-gate and top-contact (BG-TC), (b) bottom-gate and bottom-contact (BG-BC), (c) top-gate and top-contact (TG-TC) and (d) top-gate and bottom-contact (TG-BC).

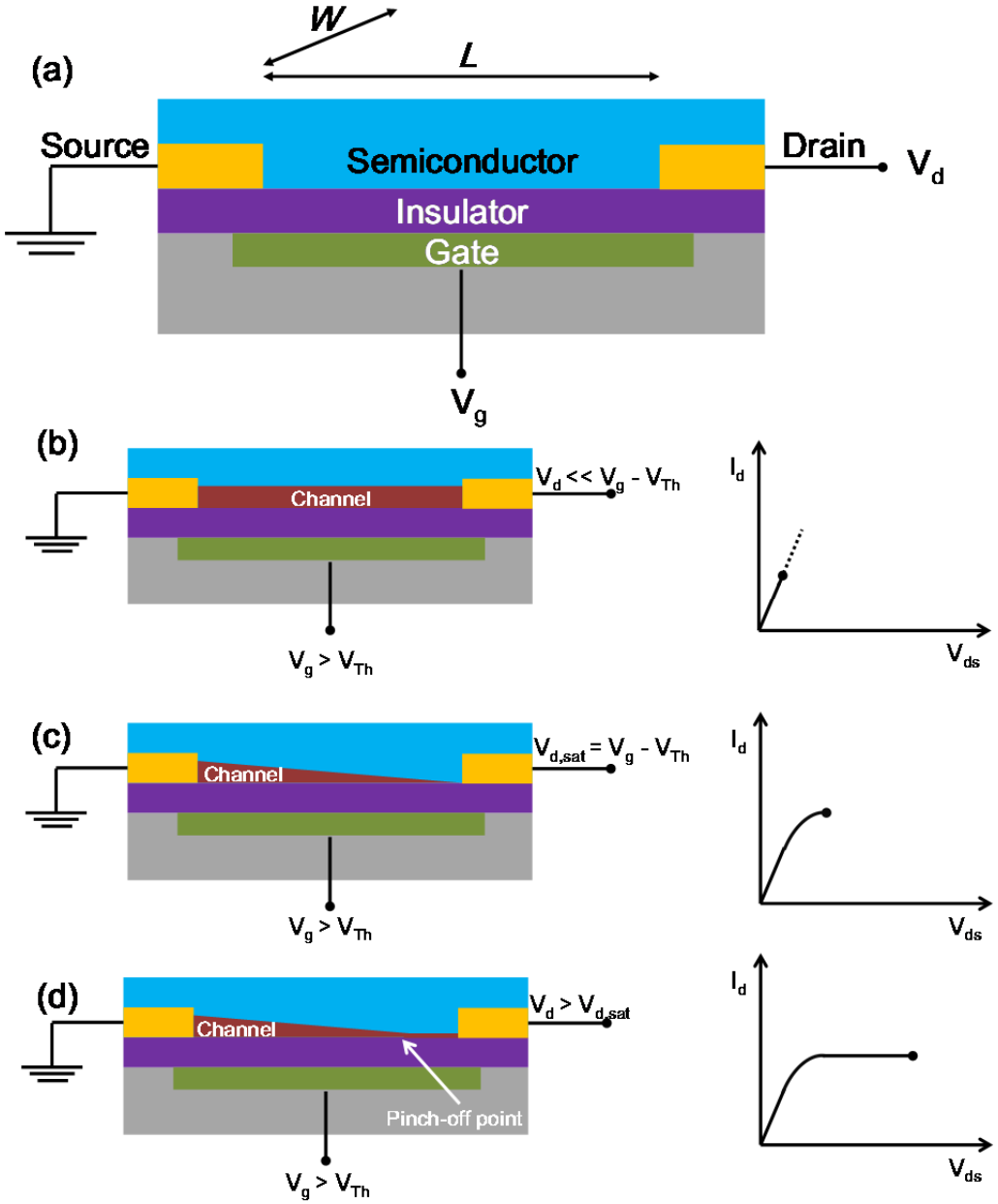

Figure 1.3.5. (a) Schematic structure of a field-effect transistor and applied voltages: (L) channel length, (W) channel width, (V_d) drain voltage, (V_g) gate voltage, (V_{Th}) threshold voltage and (I_d) drain current. (b-d) Illustrations of operating regimes of field-effect transistors: (b) linear regime; (c) start of saturation regime at pinch-off; (d) saturation regime and corresponding current-voltage characteristics.[72]

Principle of OFETs

The operation mechanism of OFETs is illustrated in Figure 1.3.5. Regarding the charge in each terminal, the source electrode should be grounded, and the drain and gate voltages should be positive for *n*-channel devices and negative for *p*-channel devices. In addition, the efficiency in OFETs depends on the charge carrier accumulation in the organic semiconductors with some bias applied on

the gate electrode. In the case of zero gate voltage (V_g = 0 V) with intrinsic semiconductors, there should be no free charge carriers in the conducting channel, and the source−drain current will converge to near zero ("off" state) when a voltage is applied between the source and the drain. If a negative gate voltage (V_g < 0 V) is applied, positive charges (*p*-channel) will be created in the vicinity of the semiconductor/dielectric interface, and the source−drain current (I_{ds}) will dramatically increase ("on" state) as a consequence (vice versa if a positive gate voltage (V_g > 0 V) is applied). The I_{ds} in the conducting channel is controlled by the gate voltage, and the polarity of charge carriers in the conducting channel determines whether the semiconductor is *p*-type, *n*-type, or ambipolar. After the accumulation of charge carriers, intramolecular charge migration within single molecules and intermolecular hopping between adjacent molecules are considered two classifications of commonly accepted transport models in less ordered organic semiconductors; usually,[18] intermolecular hopping is the critical factor limiting OFET mobility, which relies on supramolecular self-assembly in the film state.[73]

The three critical parameters determining OFET performance are charge carrier mobility (μ), current modulation ratio (I_{on}/I_{off}), and threshold voltage (V_t);[74] μ is demonstrated by how fast charge carriers drift in the active layer per unit electric field, which in turn determines the voltage to be applied and device power consumption. I_{on}/I_{off} is defined as the ratio of the source−drain current when the gate bias is maximal ("on" state) and when there is no gate bias ("off" state), which is an indicator of purity in organic materials and its susceptibility to doping by its surroundings. V_t characterizes the critical voltage at which the field effect is operative, and it serves as a measurement of the number of charge carrier traps at the semiconductor/dielectric interface. Highly pure materials have no traps that must be filled before charge carriers can flow between the source and the drain,[75] leading to efficient charge transporting characteristics.

The performance parameters are obtained from the OFET output and transfer characteristics. In the output characteristics, two operation regions can be differentiated into a linear region at a low drain voltage and a saturation region at a high drain voltage. The charge carrier mobility (μ) and threshold voltage (V_t) in the saturation region can be calculated from the transfer characteristic using the following equation:

$$I_{DS} = \frac{\mu C_{diel} W}{2L}(V_{GS} - V_{th})^2$$

where W is the channel width, L is the channel length (Figure 1.3.5), C_i is the dielectric capacitance, μ is the mobility, V_g is the gate voltage, and V_t is the threshold voltage. The current modulation I_{on}/I_{off} can be derived from the quotient of the "on" current divided by the "off" current.[76]

1.4 Isoindigo (IIG) Materials

1.4.1 Background

In 2010, Reynolds and co-workers pioneered a novel planar (IIG) (exactly, 6,6'-dibromoisoindigo),[20,77] a structural isomer of indigo, with a strong electron-affinity character owing to the conjugation of the lactam ring and large optical transition dipoles suitable for organic optoelectronic materials.[78] As far as a strong intramolecular charge transfer (ICT) induced by the donor-acceptor strategy is concerned, IIG has been introduced as the acceptor unit in constructing various donor-acceptor organic semiconductor copolymers, either of which makes hole-transport materials for OPVs and OFETs.

1.4.2 Synthesis of Isoindigo

The synthetic route of IIG is from the acid-catalyzed aldol condensation of 6-bromoisatin and 6-bromooxindole with dehydration in acetic acid almost quantitative yield.[20,77] (Scheme 1.4.1) However, non-functionalized IIG shows limited solubility in common organic solvent due to the extended conjugation length of the core and strongly intermolecular hydrogen bonding. Therefore, almost all IIG monomers make alkylated forms with *N*-alkylation of the amine position of two lactam rings.[20,77,79] (Figure 1.4.2) The *N*-alkylated IIG monomer, directly using the coupling reaction for polymerization with various counterparts, will be applied to optoelectronic devices.

Scheme 1.4.1. Synthetic route of 6,6'-dibromoisoindigo (IIG).

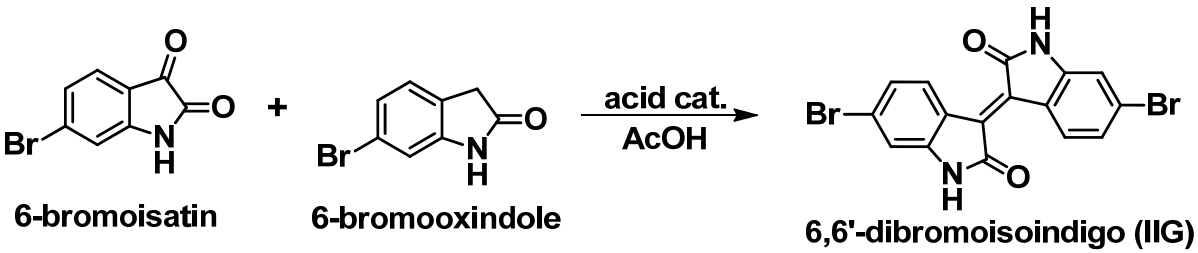

Scheme 1.4.2. Synthetic route of *N*-alkylated 6,6'-dibromoisoindigo.

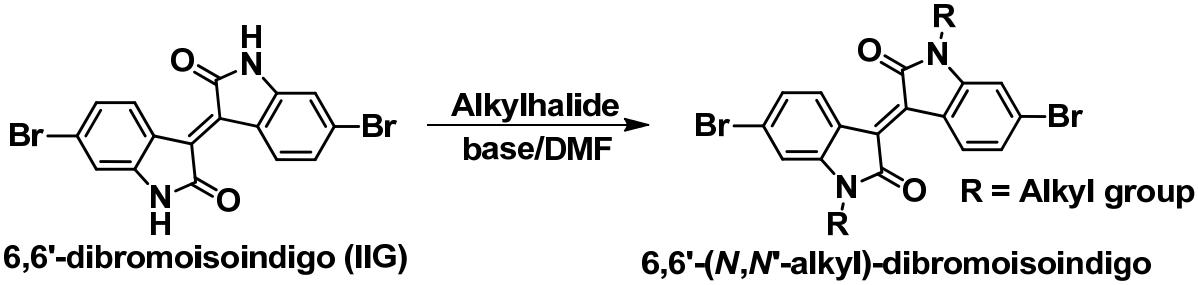

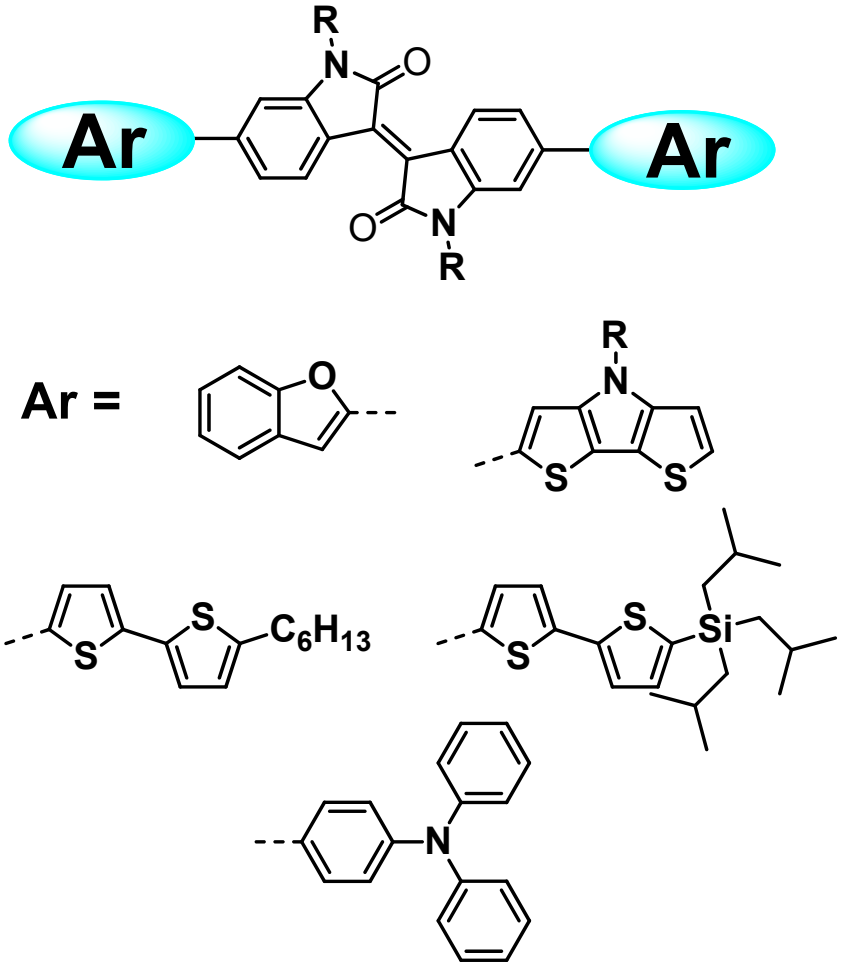

Figure 1.4.1. Chemical structure of IIG-based small molecules for OPV.

1.4.3 Isoindigo-based Semiconductors for OPVs

Small molecules of IIG have shown good performance for photoactive materials of OPV devices. The first IIG small molecule for OPVs reported by Reynolds and co-workers consisted of an IIG core and thiophene derivate end-group. In this moiety, the IIG was affected by the acceptor in these semiconductors and constructed a donor-acceptor-donor architecture.[20,80-83] (Figure 1.4.1)

The IIG polymers for the donor materials of OPVs exhibited high-performance power conversion efficiency with fullerene acceptors. The IIG monomer has been accepting properties, and many chemists have synthesized it with donating counterparts for donor-acceptor (D-A type) and accepting counterparts for acceptor-acceptor (A-A type). In each alternating system, the polymer types used are donor (D-A type) and acceptor (A-A type), respectively.[77,84-93] (Figure 1.4.2)

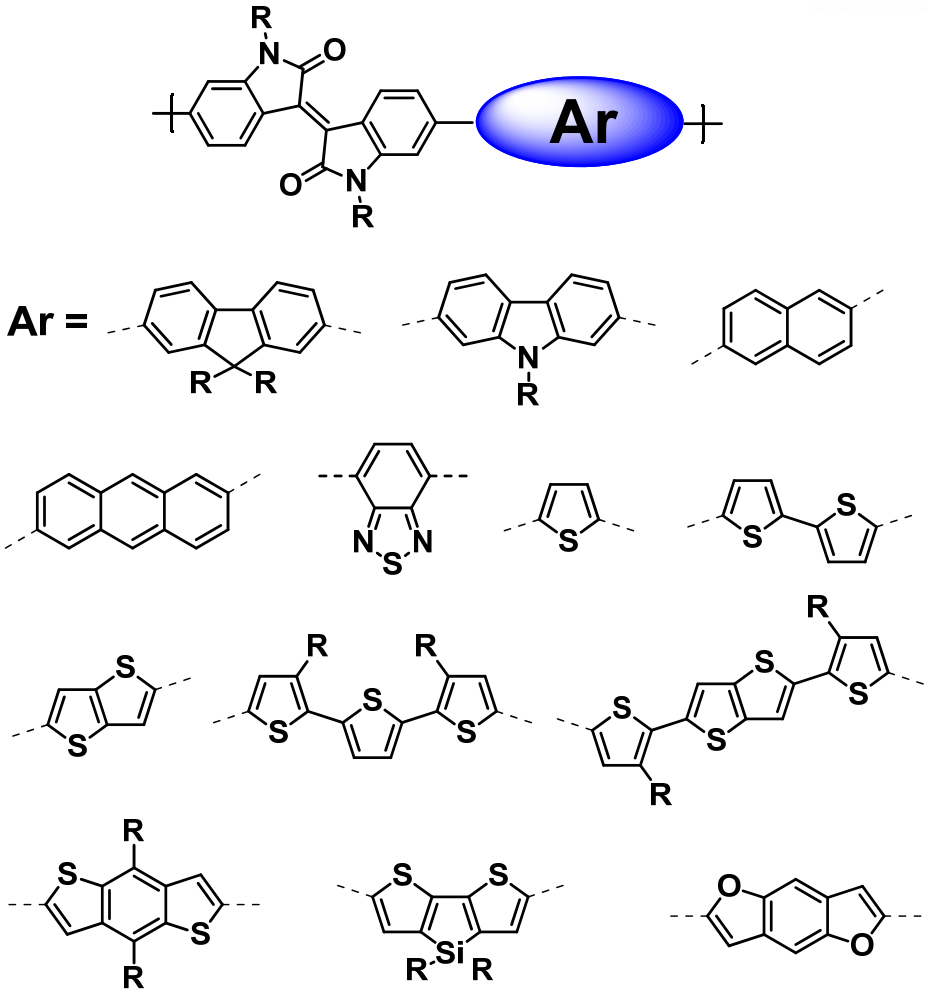

Figure 1.4.2. Chemical structure of IIG-based polymers for OPV.

1.4.4 Isoindigo-based Semiconductors for OFETs

Pei and co-workers developed IIG with thiophene and bithiophene donor-alternating copolymers, respectively, and first investigated their OFET performance. These polymers used a 2-octyldodecyl alkyl chain on the IIG unit to increase solubility. (Figure 1.4.3) The research group investigated the effect of the alkyl chain branching position on the hole mobilities of IIG copolymers. In addition, Bao and co-workers proposed a conversion from a normally branched alkyl to a siloxane-terminated hybrid side-chain, which dramatically increased OFETs' mobility.[21,79,94-96] (Figure 1.4.4)

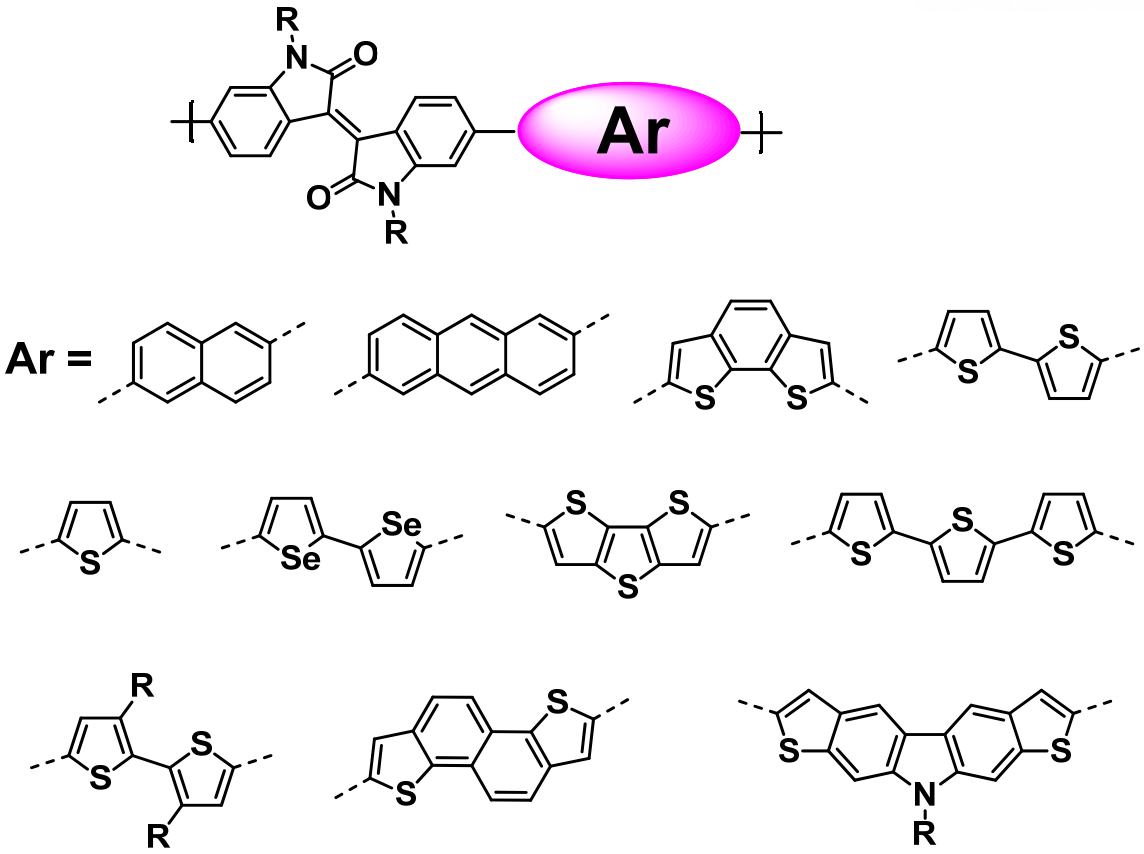

Figure 1.4.3. Chemical structure of IIG-based polymers for OFET.

1.5 Research Overview

1.5.1 Counterpart Modification

The IIG accepts moiety for organic semiconductors with other donating counterparts. D-A type materials exhibit broad light absorption, which means strong intramolecular charge transfer and a low energy band gap. In addition, the balance of D-A fragments are controlled energy level, such as HOMO and LUMO for optoelectronic applications. Therefore, many counterparts for IIG coupling have been suggested, such as five- or six-membered aromatic structures with various electron-donating and -withdrawing properties.

First, in this research, using a material design methodology called “A-A type” for high-performance *n*-channel semiconductors, two IIG-based A-A type copolymers were synthesized by copolymerizing an IIG core with either benzothiadiazole (BT) or thienopyrroledione (TPD), PIIG-BT and PIIG-TPD, respectively, both of which proved to be promising acceptor units.

Secondly, a previously reported A-A type copolymer, such as PIIG-BT, was used with heteroaromatic spacers, and D-A-D-A type copolymers were synthesized to affect the polarity tuning in OFET devices.[65,97]

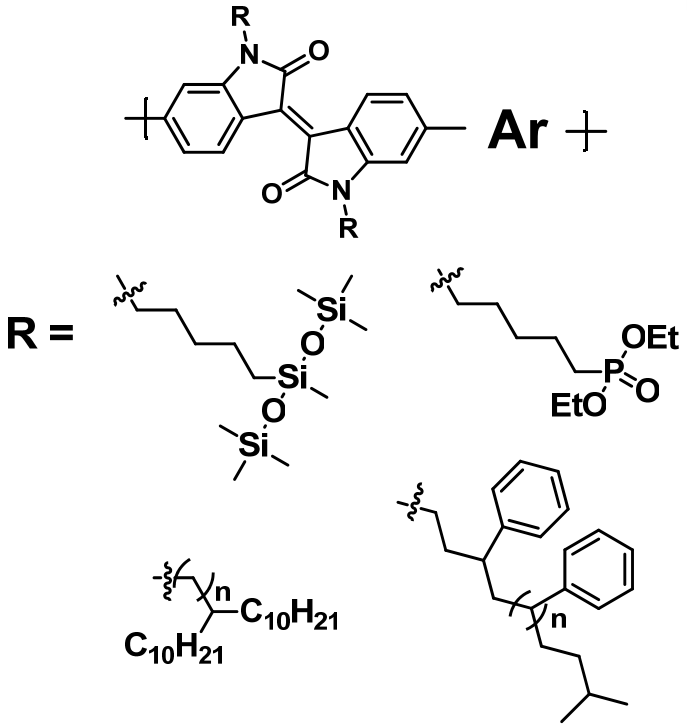

Figure 1.4.4. Various side-chins for IIG-based polymers.

1.5.2 Thienoisoindigo Materials

In 2012, McCulloch and co-workers revealed a thiophene-implanted IIG fragment, thienoisoindigo (TIIG),[98] by modulating from the outermost aryl parts of IIG to the five-membered heterocyclic thiophene rings. (Scheme 1.5.1) Consequently, the unique structural features of TIIG are capable of (i) improving co-planarity to the molecular plane via S···O interactions and (ii) enhancing charge delocalization via the quinoidal structure of the backbone, which can lead to better molecular ordering, π-conjugation, and charge transport efficiency.[98-104] (Figure 1.5.1)

In this part, we depart from the common choice of the heteroacene-based donors and focus on employing an acene-based centrosymmetric donor unit for the TIIG-based platform. Using commercially available naphthalene (Np) as the simplest fused centrosymmetric acene, we present an easily accessible TIIG-containing D-A polymer, poly(thienoisoindigo-*alt*-naphthalene) (abbreviated as PTIIG-Np), and comprehensively describe its thin-film properties and OFET characteristics.[67]

Scheme 1.5.1. Synthetic route of thienoisoindigo (TIIG).

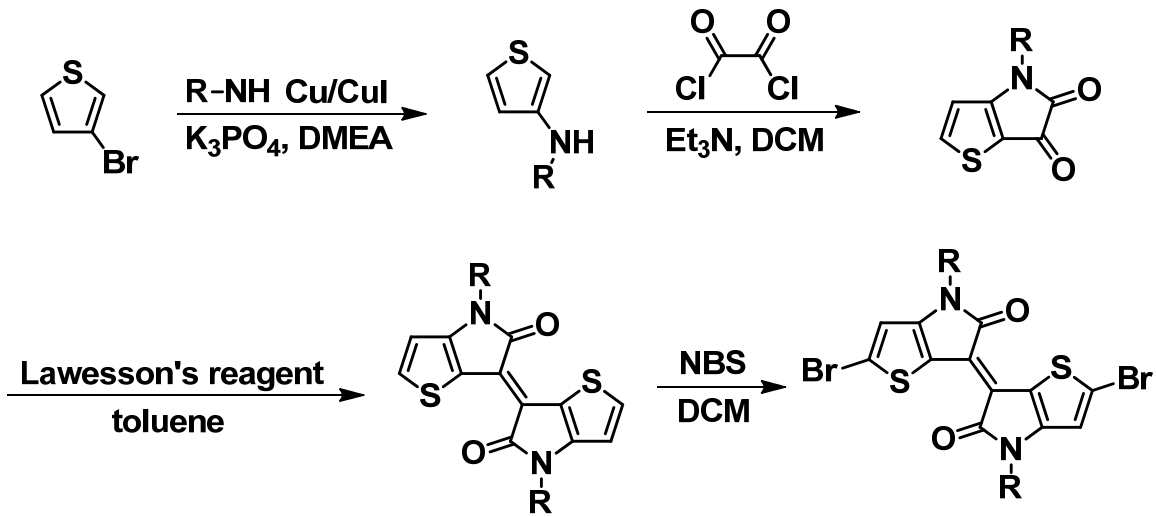

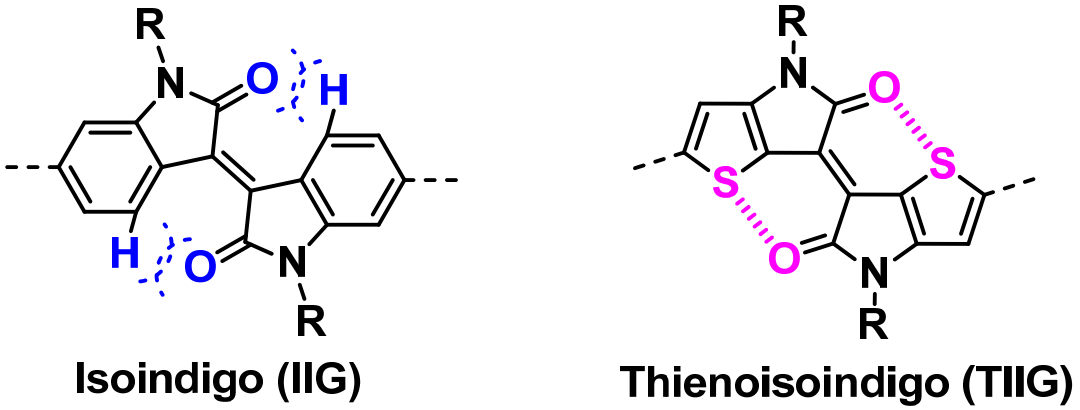

Figure 1.5.1. Chemical structures of isoindigo (IIG), thienoisoindigo (TIIG).

1.4.4 Side-chain Modification

To enhance optoelectronic performance, researchers have used “side-chain engineering” on organic semiconductors. In the past decade, side-chains have been utilized by normal hydrocarbon groups (alkyl groups) to solubilize materials. On the other hand, recently, side-chain engineering has been used to greatly enhance optoelectronics characteristic, such as OPVs and OFETs, with π-conjugated organic semiconductors. Now, side-chains have not been fully explored and understood; however, many side-chain groups have been proposed and studied over the years (e.g., alkyl, component, characteristic hybrid, ionic, reactive, etc.).[105] (Figure 1.5.2)

In this part, we have introduced a variable amount of phosphonate-terminated non-ionic side-chain substitution into an IIG-based model polymer for OPVs. The polymers were designed with the

following considerations: (i) The phosphonate groups have good compatibility with metal-oxide due to their polar and hydrophilic character. (ii) The incorporation of phosphonate side-chains can both increase the dielectric constant of the donor polymer and suppress non-geminate recombination losses in inverted polymer solar cells. (iii) A further aspect of the phosphonates is the possibility of avoiding electrical field-induced redistribution of ion/electrode interfaces.[106]

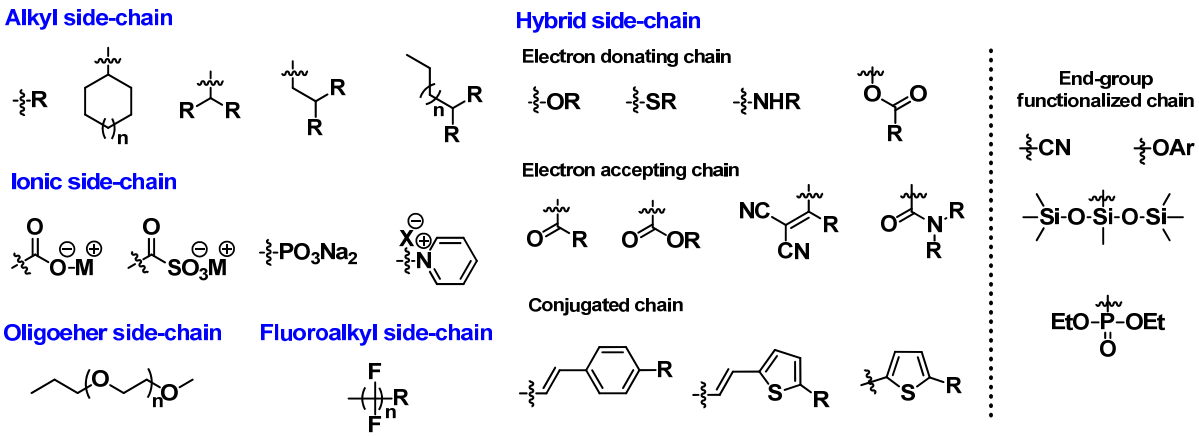

Figure 1.5.2. Chemical structures of various side-chains.

1.6 Reference

1. Cheng, Y.-J.; Yang, S.-H.; Hsu, C.-S. *Chem. Rev.* **2009**, *109*, 5868.
2. Günes, S.; Neugebauer, H.; Sariciftci, N. S. *Chem. Rev.* **2007**, *107*, 1324.
3. Yu, G.; Gao, J.; Hummelen, J. C.; Wudl, F.; Heeger, A. J. *Science* **1995**, *270*, 1789.
4. Forrest, S. R. *Nature* **2004**, *428*, 911.
5. Arias, A. C.; MacKenzie, J. D.; McCulloch, I.; Rivnay, J.; Salleo, A. *Chem. Rev.* **2010**, *110*, 3.
6. Shirakawa, H.; Louis, E. J.; MacDiarmid, A. G.; Chiang, C. K.; Heeger, A. J. *J. Chem. Soc., Chem. Commun.* **1977**, 578.
7. https://en.wikipedia.org/wiki/Conductive_polymer.
8. Burroughes, J.; Bradley, D.; Brown, A.; Marks, R.; Mackay, K.; Friend, R.; Burns, P.; Holmes, A. *Nature* **1990**, *347*, 539.

9. Kobayashi, H.; Kanbe, S.; Seki, S.; Kigchi, H.; Kimura, M.; Yudasaka, I.; Miyashita, S.; Shimoda, T.; Towns, C. R.; Burroughes, J. H. *Synt. Met.* **2000**, *111*, 125.

10. Bernius, M. T.; Inbasekaran, M.; O'Brien, J.; Wu, W. *Adv. Mater.* **2000**, *12*, 1737.

11. Friend, R.; Gymer, R.; Holmes, A.; Burroughes, J.; Marks, R.; Taliani, C.; Bradley, D.; Dos Santos, D.; Bredas, J.; Lögdlund, M. *Nature* **1999**, *397*, 121.

12. Dai, L.; Winkler, B.; Dong, L.; Tong, L.; Mau, A. W. *Adv. Mater.* **2001**, *13*, 915.

13. Fukuda, Y.; Watanabe, T.; Wakimoto, T.; Miyaguchi, S.; Tsuchida, M. *Synt. Met.* **2000**, *111*, 1.

14. Kim, J. Y.; Lee, K.; Coates, N. E.; Moses, D.; Nguyen, T.-Q.; Dante, M.; Heeger, A. J. *Science* **2007**, *317*, 222.

15. Park, S. H.; Roy, A.; Beaupre, S.; Cho, S.; Coates, N.; Moon, J. S.; Moses, D.; Leclerc, M.; Lee, K.; Heeger, A. J. *Nature Photon.* **2009**, *3*, 297.

16. Garnier, F.; Hajlaoui, R.; Yassar, A.; Srivastava, P. *Science* **1994**, *265*, 1684.

17. Facchetti, A.; Deng, Y.; Wang, A.; Koide, Y.; Sirringhaus, H.; Marks, T. J.; Friend, R. H. *Angew. Chem. Int. Ed.* **2000**, *39*, 4547.

18. Murphy, A. R.; Frechet, J. M. *Chem. Rev.* **2007**, *107*, 1066.

19. Hirsch, J. *J. Phys. C* **1979**, *12*, 321.

20. Mei, J.; Graham, K. R.; Stalder, R.; Reynolds, J. R. *Org. lett.* **2010**, *12*, 660.

21. Lei, T.; Cao, Y.; Zhou, X.; Peng, Y.; Bian, J.; Pei, J. *Chem. Mater.* **2012**, *24*, 1762.

22. Nielsen, C. B.; Turbiez, M.; McCulloch, I. *Adv. Mater.* **2013**, *25*, 1859.

23. Cho, S.; Lee, J.; Tong, M.; Seo, J. H.; Yang, C. *Adv. Funct. Mater.* **2011**, *21*, 1910.

24. Steyrleuthner, R.; Schubert, M.; Jaiser, F.; Blakesley, J. C.; Chen, Z.; Facchetti, A.; Neher, D. *Adv. Mater.* **2010**, *22*, 2799.

25. Baeg, K. J.; Khim, D.; Jung, S. W.; Kang, M.; You, I. K.; Kim, D. Y.; Facchetti, A.; Noh, Y. Y. *Adv. Mater.* **2012**, *24*, 5433.

26. Hassan, J.; Sevignon, M.; Gozzi, C.; Schulz, E.; Lemaire, M. *Chem. Rev.* **2002**, *102*, 1359.

27. http://en.wikipedia.org/wiki/Coupling_reaction.

28. http://nobelprize.org/nobel_prizes/chemistry/laureates/2010.

29. Beletskaya, I. P.; Cheprakov, A. V. *Coord. Chem. Rev.* **2004**, *248*, 2337.

30. Rosen, B. M.; Quasdorf, K. W.; Wilson, D. A.; Zhang, N.; Resmerita, A.-M.; Garg, N. K.; Percec, V. *Chem. Rev.* **2010**, *111*, 1346.

31. Allen, D. V., University of Massachusetts Amherst, 2004.

32. Miyaura, N.; Yamada, K.; Suzuki, A. *Tetrahedron Lett.* **1979**, *20*, 3437.

33. Miyaura, N.; Suzuki, A. *J. Chem. Soc., Chem. Commun.* **1979**, 866.

34. Miyaura, N.; Suzuki, A. *Chem. Rev.* **1995**, *95*, 2457.

35. Milstein, D.; Stille, J. *J. Am. Chem. Soc.* **1978**, *100*, 3636.

36. Stille, J. K. *Angew. Chem. Int. Ed.* **1986**, *25*, 508.
37. Kosugi, M.; Sasazawa, K.; Shimizu, Y.; Migita, T. *Chem. Lett.* **1977**, *6*, 301.
38. Yin, L.; Liebscher, J. *Chem. Rev.* **2007**, *107*, 133.
39. King, A. O.; Okukado, N.; Negishi, E.-i. *J. Chem. Soc., Chem. Commun.* **1977**, 683.
40. Heck, R.; Nolley Jr, J. *J. Org. Chem.* **1972**, *37*, 2320.
41. Mizoroki, T.; Mori, K.; Ozaki, A. *Bull. Chem. Soc. Jpn.* **1971**, *44*, 581.
42. Heck, R. F. *Org. React.* **1982**.
43. De Meijere, A.; Meyer, F. E. *Angew. Chem. Int. Ed.* **1995**, *33*, 2379.
44. Tang, C. W. *Appl. Phys. Lett.* **1986**, *48*, 183.
45. Sariciftci, N.; Smilowitz, L.; Heeger, A. J.; Wudl, F. *Science* **1992**, *258*, 1474.
46. Jørgensen, M.; Norrman, K.; Krebs, F. C. *Sol. Energ. Mat. Sol. Cells* **2008**, *92*, 686.
47. Sun, Y.; Seo, J. H.; Takacs, C. J.; Seifter, J.; Heeger, A. J. *Adv. Mater.* **2011**, *23*, 1679.
48. Hau, S. K.; Yip, H.-L.; Leong, K.; Jen, A. K.-Y. *Org. Electron.* **2009**, *10*, 719.
49. Kim, G.; Yeom, H. R.; Cho, S.; Seo, J. H.; Kim, J. Y.; Yang, C. *Macromolecules* **2012**, *45*, 1847.
50. Nunzi, J.-M. *Comptes Rendus Physique* **2002**, *3*, 523.
51. Saunders, B. R.; Turner, M. L. *Adv. Colloid Interface Sci.* **2008**, *138*, 1.
52. Heremans, P.; Cheyns, D.; Rand, B. P. *Acc. Chem. Res.* **2009**, *42*, 1740.
53. Ameri, T.; Dennler, G.; Lungenschmied, C.; Brabec, C. J. *Energy Environ. Sci.* **2009**, *2*, 347.
54. van Duren, J. K.; Yang, X.; Loos, J.; Bulle-Lieuwma, C. W.; Sieval, A. B.; Hummelen, J. C.; Janssen, R. A. *Adv. Funct. Mater.* **2004**, *14*, 425.
55. Hoppe, H.; Glatzel, T.; Niggemann, M.; Schwinger, W.; Schaeffler, F.; Hinsch, A.; Lux-Steiner, M. C.; Sariciftci, N. *Thin Solid Films* **2006**, *511*, 587.
56. Hoppe, H.; Niggemann, M.; Winder, C.; Kraut, J.; Hiesgen, R.; Hinsch, A.; Meissner, D.; Sariciftci, N. S. *Adv. Funct. Mater.* **2004**, *14*, 1005.
57. Gebeyehu, D.; Brabec, C.; Padinger, F.; Fromherz, T.; Hummelen, J.; Badt, D.; Schindler, H.; Sariciftci, N. *Synt. Met.* **2001**, *118*, 1.
58. Martens, T.; D'Haen, J.; Munters, T.; Beelen, Z.; Goris, L.; Manca, J.; D'Olieslaeger, M.; Vanderzande, D.; De Schepper, L.; Andriessen, R. *Synt. Met.* **2003**, *138*, 243.
59. Brabec, C. J.; Cravino, A.; Meissner, D.; Sariciftci, N. S.; Fromherz, T.; Rispens, M. T.; Sanchez, L.; Hummelen, J. C. *Adv. Funct. Mater.* **2001**, *11*, 374.
60. Scharber, M. C.; Muhlbacher, D.; Koppe, M.; Denk, P.; Waldauf, C.; Heeger, A. J.; Brabec, C. J. *Adv. Mater.* **2006**, *18*, 789.
61. Riedel, I.; Dyakonov, V. *Phys. Status Solidi A* **2004**, *201*, 1332.
62. Schilinsky, P.; Waldauf, C.; Hauch, J.; Brabec, C. J. *J. Appl. Phys.* **2004**, *95*, 2816.
63. Tsumura, A.; Koezuka, H.; Ando, T. *Appl. Phys. Lett.* **1986**, *49*, 1210.

64. Edgar, L. J.; US Patents: 1930, p US1745175 A.

65. Kim, G.; Han, A.-R.; Lee, H. R.; Lee, J.; Oh, J. H.; Yang, C. *Chem. Commun.* **2014**, *50*, 2180.

66. Kim, G.; Han, A.-R.; Lee, H. R.; Oh, J. H.; Yang, C. *Phys. Chem. Chem. Phys.* **2015**, *17*.

67. Kim, G.; Kang, S.-J.; Dutta, G. K.; Han, Y.-K.; Shin, T. J.; Noh, Y.-Y.; Yang, C. *J. Am. Chem. Soc.* **2014**, *136*, 9477.

68. Kim, G.; Han, A.-R.; Lee, H. R.; Oh, J. H.; Yang, C. *Phys. Chem. Chem. Phys.* **2015**, *17*, 26512.

69. Lee, J.; Han, A.-R.; Yu, H.; Shin, T. J.; Yang, C.; Oh, J. H. *J. Am. Chem. Soc.* **2013**, *135*, 9540.

70. Lee, J.; Han, A.-R.; Kim, J.; Kim, Y.; Oh, J. H.; Yang, C. *J. Am. Chem. Soc.* **2012**, *134*, 20713.

71. Kim, Y.; Long, D. X.; Lee, J.; Kim, G.; Shin, T. J.; Nam, K.-W.; Noh, Y.-Y.; Yang, C. *Macromolecules* **2015**, *48*, 5179.

72. Zaumseil, J.; Sirringhaus, H. *Chem. Rev.* **2007**, *107*, 1296.

73. Hoeben, F. J.; Jonkheijm, P.; Meijer, E.; Schenning, A. P. *Chem. Rev.* **2005**, *105*, 1491.

74. Newman, C. R.; Frisbie, C. D.; da Silva Filho, D. A.; Brédas, J.-L.; Ewbank, P. C.; Mann, K. R. *Chem. Mater.* **2004**, *16*, 4436.

75. Dimitrakopoulos, C. D.; Malenfant, P. R. *Adv. Mater.* **2002**, *14*, 99.

76. Guo, X.; Facchetti, A.; Marks, T. J. *Chem. Rev.* **2014**, *114*, 8943.

77. Stalder, R.; Mei, J.; Reynolds, J. R. *Macromolecules* **2010**, *43*, 8348.

78. Robb, M. J.; Ku, S. Y.; Brunetti, F. G.; Hawker, C. J. *J. Polym. Sci. A Polym. Chem.* **2013**, *51*, 1263.

79. Lei, T.; Cao, Y.; Fan, Y.; Liu, C.-J.; Yuan, S.-C.; Pei, J. *J. Am. Chem. Soc.* **2011**, *133*, 6099.

80. Graham, K. R.; Mei, J.; Stalder, R.; Shim, J. W.; Cheun, H.; Steffy, F.; So, F.; Kippelen, B.; Reynolds, J. R. *ACS Appl. Mater. Interfaces* **2011**, *3*, 1210.

81. Graham, K. R.; Wieruszewski, P. M.; Stalder, R.; Hartel, M. J.; Mei, J.; So, F.; Reynolds, J. R. *Adv. Funct. Mater.* **2012**, *22*, 4801.

82. Graham, K. R.; Stalder, R.; Wieruszewski, P. M.; Patel, D. G.; Salazar, D. H.; Reynolds, J. R. *ACS Appl. Mater. Interfaces* **2012**, *5*, 63.

83. Yassin, A.; Leriche, P.; Allain, M.; Roncali, J. *New J. Chem.* **2013**, *37*, 502.

84. Kuwabara, J.; Nohara, Y.; Choi, S. J.; Fujinami, Y.; Lu, W.; Yoshimura, K.; Oguma, J.; Suenobu, K.; Kanbara, T. *Polym. Chem.* **2013**, *4*, 947.

85. Liu, B.; Zou, Y.; Peng, B.; Zhao, B.; Huang, K.; He, Y.; Pan, C. *Polym. Chem.* **2011**, *2*, 1156.

86. Wang, E.; Ma, Z.; Zhang, Z.; Henriksson, P.; Inganäs, O.; Zhang, F.; Andersson, M. R. *Chem. Commun.* **2011**, *47*, 4908.

87. Ma, Z.; Wang, E.; Vandewal, K.; Andersson, M. R.; Zhang, F. *Appl. Phys. Lett.* **2011**, *99*, 143302.

88. Zhang, G.; Fu, Y.; Xie, Z.; Zhang, Q. *Macromolecules* **2011**, *44*, 1414.

89. Wang, E.; Ma, Z.; Zhang, Z.; Vandewal, K.; Henriksson, P.; Inganäs, O.; Zhang, F.; Andersson, M. R. *J. Am. Chem. Soc.* **2011**, *133*, 14244.

90. Stalder, R.; Grand, C.; Subbiah, J.; So, F.; Reynolds, J. R. *Polym. Chem.* **2012**, *3*, 89.

91. Xu, X.; Cai, P.; Lu, Y.; Choon, N. S.; Chen, J.; Hu, X.; Ong, B. S. *J. Polym. Sci. A Polym. Chem.* **2013**, *51*, 424.

92. Ma, Z.; Wang, E.; Jarvid, M. E.; Henriksson, P.; Inganäs, O.; Zhang, F.; Andersson, M. R. *J. Mater. Chem.* **2012**, *22*, 2306.

93. Hu, C.; Fu, Y.; Li, S.; Xie, Z.; Zhang, Q. *Polym. Chem.* **2012**, *3*, 2949.

94. Mei, J.; Kim, D. H.; Ayzner, A. L.; Toney, M. F.; Bao, Z. *J. Am. Chem. Soc.* **2011**, *133*, 20130.

95. Lei, T.; Dou, J. H.; Pei, J. *Adv. Mater.* **2012**, *24*, 6457.

96. Deng, Y.; Chen, Y.; Zhang, X.; Tian, H.; Bao, C.; Yan, D.; Geng, Y.; Wang, F. *Macromolecules* **2012**, *45*, 8621.

97. Kim, G.; Han, A.-R.; Lee, H. R.; Oh, J. H.; Yang, C. *Phys. Chem. Chem. Phys.* **2015**, *7*, 26512.

98. Ashraf, R. S.; Kronemeijer, A. J.; James, D. I.; Sirringhaus, H.; McCulloch, I. *Chem. Commun.* **2012**, *48*, 3939.

99. Sirringhaus, H.; Brown, P.; Friend, R.; Nielsen, M. M.; Bechgaard, K.; Langeveld-Voss, B.; Spiering, A.; Janssen, R. A.; Meijer, E.; Herwig, P. *Nature* **1999**, *401*, 685.

100. Koizumi, Y.; Ide, M.; Saeki, A.; Vijayakumar, C.; Balan, B.; Kawamoto, M.; Seki, S. *Polym. Chem.* **2013**, *4*, 484.

101. Van Pruissen, G. W.; Gholamrezaie, F.; Wienk, M. M.; Janssen, R. A. *J. Mater. Chem.* **2012**, *22*, 20387.

102. Chabinyc, M. L.; Toney, M. F.; Kline, R. J.; McCulloch, I.; Heeney, M. *J. Am. Chem. Soc.* **2007**, *129*, 3226.

103. DeLongchamp, D. M.; Kline, R. J.; Lin, E. K.; Fischer, D. A.; Richter, L. J.; Lucas, L. A.; Heeney, M.; McCulloch, I.; Northrup, J. E. *Adv. Mater.* **2007**, *19*, 833.

104. Dutta, G. K.; Han, A.; Lee, J.; Kim, Y.; Oh, J. H.; Yang, C. *Adv. Funct. Mater.* **2013**, *23*, 5317.

105. Mei, J.; Bao, Z. *Chem. Mater.* **2013**, *26*, 604.

106. Kim, G.; Song, S.; Lee, J.; Kim, T.; Lee, T. H.; Walker, B.; Kim, J. Y.; Yang, C. *Adv. Energy Mater.* **2015**, *5*, 10.1002/aenm.201500844.

Chapter 2 Conjugated Backbone Modification for Tuning the Polarity in Organic Field-Effect Transistors

2.1. Acceptor-Acceptor Type Isoindigo Polymers for *n*-type Characteristics

Chapter 2.1 is reproduced in part with permission of "Acceptor-acceptor type isoindigo-based copolymers for high-performance n-channel field-effect transistors" from Kim G. *et al*. *Chem. Commun.*, **2014**, *50*, 2180.

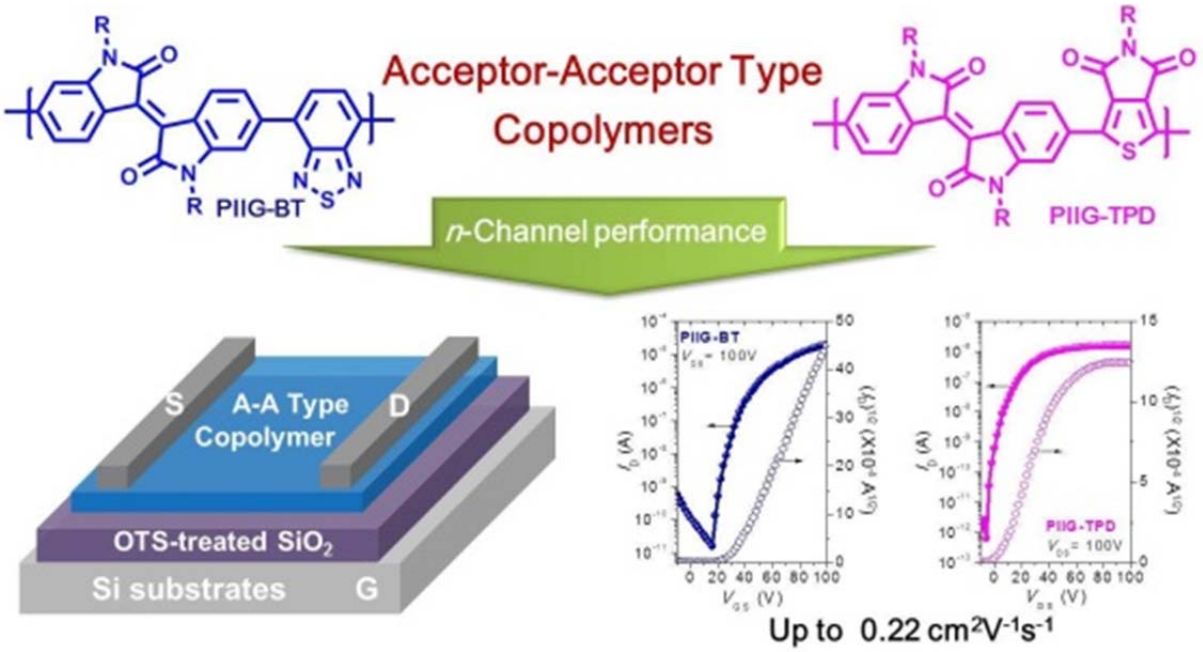

2.1.1 Introduction

In 2010, Reynolds and co-workers reported a novel planar isoindigo (IIG) unit with strong electron-affinity character and large optical transition dipoles suitable for organic electronic materials.[1, 2] As far as a strong intramolecular charge transfer (ICT) induced by the donor (D)-acceptor (A) strategy is concerned, IIG has been introduced as the A unit in constructing various D-A copolymers, either of which makes hole-transport materials for photovoltaics (PVs)[3, 4] and field-effect transistors (FETs).[5-8] The availability of both *n*- and *p*-type semiconductors is essential for these applications above, however access to conjugated high electron-affinity polymers remains a critical challenge. Considering the high electron-affinity of IIG unit, a fundamental question arises as to whether IIG-based copolymers exclusively composed of all electron deficient monomers can be expected to yield interesting electron-transporting materials. In this communication, as a materials-design

methodology,[9] called 'A-A type', for high-performance *n*-channel semiconductors, we have synthesized two A-A copolymers, PIIG-BT and PIIG-TPD, by copolymerizing IIG core with either benzothiadiazole (BT) or thienopyrroledione (TPD), both of which have proven to be one of the most promising acceptor units.[10-24] We present the high-performance, unipolar electron-transport characteristics of the FETs based on the resulting copolymers, and demonstrate the high potential of A-A type copolymers as *n*-channel semiconductors. To our delight, PIIG-BT copolymer FETs show electron mobility of up to 0.22 $cm^2 V^{-1} s^{-1}$, which, to the best of our knowledge, is the highest value among *n*-type copolymers based on lactam-like structures reported to date.

2.1.2 Result and discussion

Synthetic approach and characterization: The synthetic routes to the monomers and copolymers (PIIG-BT and PIIG-TPD) are outlined in Scheme 2.1.1. The detailed procedures are provided in experimental section. Briefly, the key intermediate 6,6'-dibromoisoindigo (1) was obtained from the condensation of 6-bromoisatin and 6-bromooxindole. The *N*-alkylation of 1 was performed using long branched 2-octyldodecyl iodide and highly soluble 6,6′-dibromoisoindigo monomer 2 was formed in 80% yield. The commercially available diboronicester BT co-monomer was further purified by recrystallization from methanol. However, it was difficult to prepare the distannyl or diboronic ester TPD as the counterpart co-monomer, by either lithiation and subsequent reaction with trimethyltin chloride or a Pd-catalyzed coupling reaction with bis(pinacolato)diboron. Thereby, we opted to synthesize the synthon diborylated IIG (3), which was obtained from the transformation of 2 under the Pd-mediated borylation method in 78% yield.[25, 26] With all monomers ready, the copolymerizations were then carried out under Suzuki type-coupling reaction, with 1:1 monomer ratio, using $Pd_2(dba)_3$ as a catalyst, P(*o*-tolyl)$_3$ as the corresponding ligand, and K_3PO_4 as a base, to afford the target copolymers, respectively. After sequential Soxhlet purification with methanol, acetone, hexane, and chloroform, gel-permeation chromatography (GPC) analysis exhibited a number-averaged molecular weight (M_n) of 25.0 and 57.1 kDa for PIIG-BT and PIIG-TPD, respectively, with a polydispersity of 1.32 and 3.30. The both copolymers were readily soluble in all organic solvents tested at room temperature.

Scheme 2.1.1. Synthetic routes of IIG-based A-A copolymers.[a]

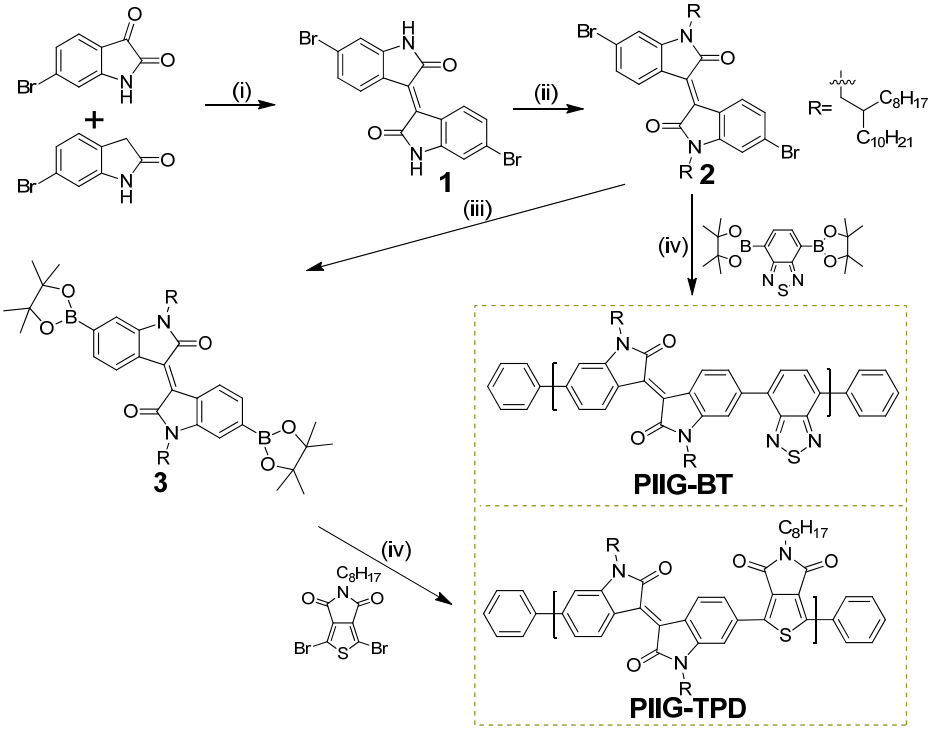

[a]Reagents and conditions: (i) AcOH, HCl, reflux, overnight; (ii) 2-octyldodecyl iodide, K_2CO_3, DMF, reflux, overnight; (iii) Bis(pinacolato)diboron, 1,4-dioxane, KOAc, $PdCl_2$(dppf), reflux; (iv) Suzuki polymerization, toluene, H_2O, K_3PO_4, P(*o*-tolyl)$_3$, $Pd_2(dba)_3$, 90°C.

Notably, together with the satisfactory yield (61%) of PIIG-TPD, its high M_n is in sharp contrast to some examples of copolymers made from the dibrominated derivatives of TPD using Suzuki polymerization, in which only low mass copolymers were obtained even with various synthetic attempts.[26] This result may be attributed to a higher ligand to Pd ratio (Pd/P(*o*-tolyl)$_3$ of 1:4) in our experiment, which can serve to suppress decomposition of the Pd catalyst.[27, 28] In addition, we cannot negate the fact that the longer branched alkyl side chains relative to the previous synthesis can provide the excellent solubility of the resulting copolymer PIIG-TPD to ensure its higher molecular weight available. Further systematic experiments are currently underway to provide a solid support for the above claimed explanation.

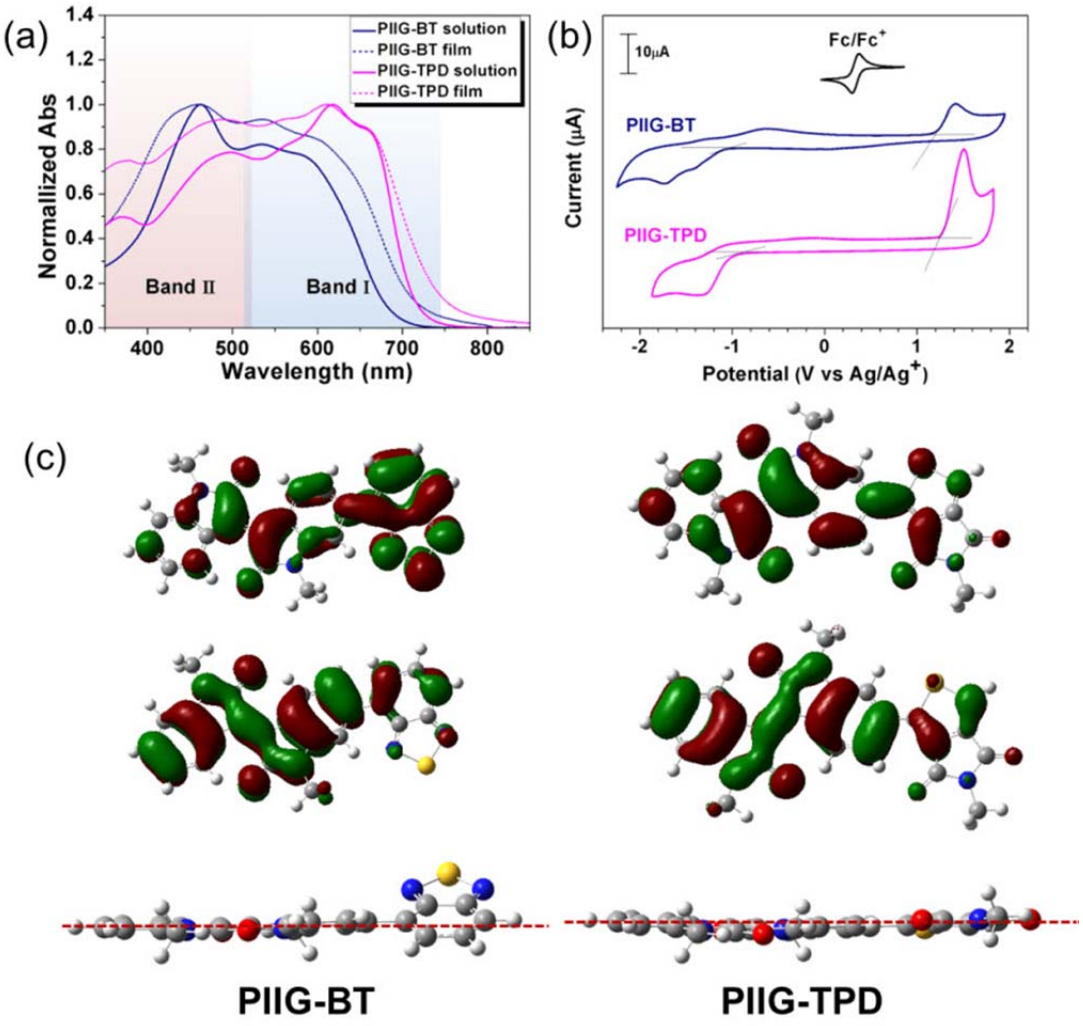

Figure 2.1.1. (a) Normalized absorption spectra in solution ($CHCl_3$) and thin films and (b) cyclic voltammograms of PIIG-BT and PIIG-TPD. (c) Calculated molecular orbitals for the model monomers of IIG-based copolymers.

Table 2.1.1. Optical and electrochemical properties of IIG-based copolymers

	λ_{max} (nm)	λ_{edge} (nm)	E_g^{opt} (eV)[a]	E_{HOMO} (eV)[b]	E_{LUMO} (eV)[b]	E_g^{elec} (eV)[c]
PIIG-BT	461	712	1.74	−5.68	−3.54	2.14
PIIG-TPD	611	746	1.66	−5.70	−3.66	2.04

[a]Calculated from the absorption band edge of the copolymer film, $E_g^{opt}=1240/\lambda_{edge}$. [b]Thin films in $CH_3CN/n\text{-}Bu_4NPF_6$, versus Fc/Fc^+ at 50 mVs^{-1}. HOMO and LUMO estimated from the onset oxidation and reduction potentials, respectively, assuming the absolute energy level of ferrocene/ferrocenium to be 4.8 eV below vacuum. [c]E_g^{elec} (eV) = −(LUMO − HOMO)

Optical and electrochemical properties The UV-Vis absorption spectra of two copolymers are shown in Figure 2.1.1a and the complete list of the optical and electrochemical data is summarized in Table 2.1.1. These copolymers exhibit a similar broad absorption band both in solution and films from 350 to 750 nm. However, the two main absorption bands (band I: 530-750 nm and band II: 350-530 nm) for PIIG-TPD are somewhat red-shifted relative to those of PIIG-BT. Consequently, the optical band gap (E_g^{opt}) of PIIG-TPD is estimated to be 0.08 eV, smaller than that of PIIG-BT. Very interestingly, PIIG-TPD shows the increased absorption intensity of the band I relative to that of the band II, when compared to this strength of the two peaks for PIIG-BT. The difference in the electron accepting strength based on the moieties (BT vs. TPD) neighbouring IIG along the backbone as a key parameter can account for the change in absorption features. The cyclic voltammetries (CV) of all copolymers in thin films were measured to evaluate their electronic energy levels **(**Figure 2.1.1b). The HOMO levels are somewhat consistent for the two copolymers with values between –5.68 and –5.70 eV, whereas the LUMO level of PIIG-TPD (–3.66 eV) is obviously lower than that of PIIG-BT (–3.54 eV). With the above all results based on optical and electrochemical data in hand, one can conclude that TPD unit has a stronger electron-accepting ability than that of the BT. Density functional theory (DFT) calculations performed with the B3LYP functional and a 6-31G basis set show that for PIIG-BT and PIIG-TPD, both the HOMO and LUMO are almost uniformly delocalized on the entire molecular backbone (Figure 2.1.1c). This observation quite differs from many D-A IIG-based copolymers in which the HOMOs are well delocalized along the polymer chain but the LUMOs are mostly localized on the IIG core.[5, 8, 29-32]

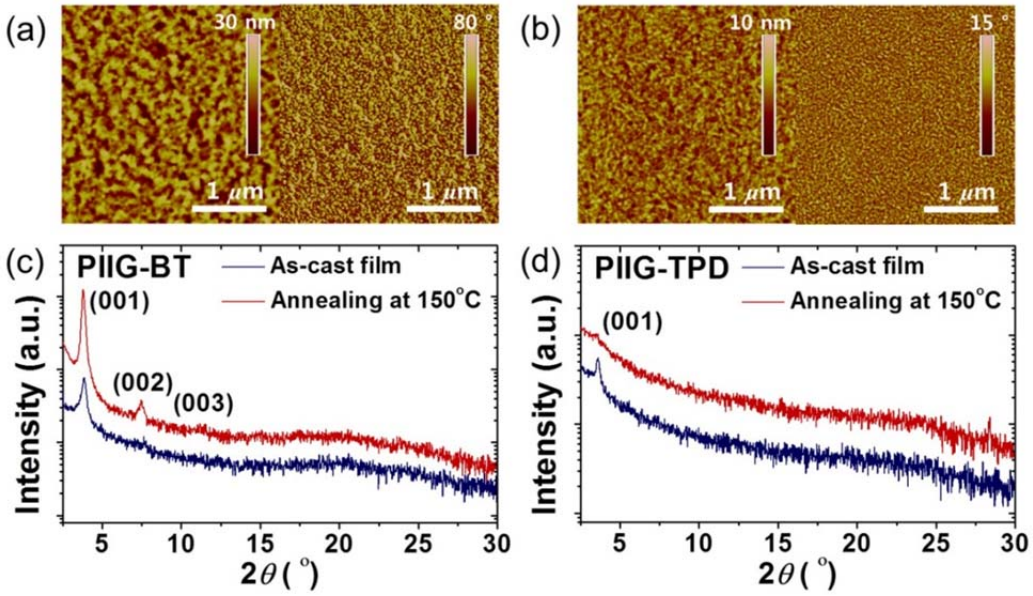

Figure 2.1.2. AFM height (left) and phase (right) images of drop-cast films of (a) PIIG-BT and (b) PIIG-TPD after annealing, and out-of-plane X-ray diffraction (XRD) patterns of (c) PIIG-BT and (d) PIIG-TPD drop-cast thin films before and after annealing. The thermal annealing was performed at 150 °C for 30 min.

Thin-film microstructure analyses The thin-films morphologies of A-A type IIG-based copolymers were investigated using tapping-mode atomic force microscopy (AFM) measurement (Figure 2.1.2a and Figure 2.1.2b). Both the optimized copolymer films formed densely interconnected nanofibrillar domains. It is interesting to note that PIIG-BT exhibited conspicuously larger grains (~170 nm in diameter) than those of PIIG-TPD (~80 nm in diameter). Therefore, we believe that PIIG-BT as compared to PIIG-TPD can substantially strengthen the intermolecular interactions to form more interconnected crystalline grains, which would allow excellent charge transport performance. The crystalline nature and molecular orientation were further studied with X-ray diffraction (XRD) analysis. The as-cast PIIG-BT and PIIG-TPD thin-films exhibited primary diffraction peaks at 2θ of 3.86° and 3.60°, corresponding to d(001)-spacing values of 22.87 and 24.52 Å respectively, while there were no discernible (010) diffractions in both cases (Figure 2.1.2c and Figure 2.1.2d). This suggests that preferentially dominant 'edge-on' orientations relative to the substrate can be deduced for each of the two copolymers. Upon the thermal annealing at 150 °C, the (001) diffraction peak of PIIG-BT film was noticeably intensified and the second- and third-order peaks became visible. In contrast, the slightly wrecked (001) peak was observed in the annealed PIIG-TPD film, indicating the decreased quality of the edge-on alignment, most likely due to the tilted main backbone driven by the additional octyl groups in TPD unit. Judging from these XRD results, it is apparent that there are more crystalline domains with edge-on orientation for the annealed PIIG-BT, compared with the annealed PIIG-TPD in which the lamellar packing became worse.

Organic field-effect transistors The electrical performance of A-A type IIG-based copolymers was evaluated by fabricating the bottom-gate/top-contact OFET devices. The polymer thin films were prepared on OTS-treated SiO_2/Si substrates by drop-casting the chloroform solution (3 mg mL^{-1}) and then annealed on a hot plate at 150 °C for 30 min in a nitrogen atmosphere. Both PIIG-BT and PIIG-TPD exhibited unipolar *n*-type field-effect behaviors, mainly due to the very low-lying HOMO level (about–5.70 eV) of electron deficient A-A type IIG-based copolymers. Figure 2.1.3 shows the representative transfer and output characteristics of optimized FETs annealed at 150 °C. The annealed thin films of IIG-based copolymers showed significantly enhanced mobilities, compared with the as-cast polymer thin films (see Table 2.1.2 for details).

The annealed PIIG-BT films exhibited efficient *n*-channel operation with high electron mobility of up to 0.22 $cm^2 V^{-1} s^{-1}$ and high I_{on}/I_{off} of 10^7. On the other hand, about one order of magnitude lower electron mobility (~0.01 $cm^2 V^{-1} s^{-1}$) was obtained from the annealed PIIG-TPD films. Note that for a fair comparison correlating PIIG-BT and PIIG-TPD profiles, PIIG-TPD with the molecular weight and PDI values (M_n = 32.0 kDa, PDI = 1.5) was isolated using a preparative GPC in chloroform and its mobility remained in a much lower level of ~0.001 $cm^2 V^{-1} s^{-1}$ (see Table 2.1.2 and Figure. 2.1.4).

This poor performance is presumably due to the smaller grains and the lower degree of the molecular orientation in the PIIG-TPD films, even though TPD unit resulted in the lower LUMO level of IIG copolymer with a stronger electron-accepting property. However, the turn-on of PIIG-TPD FETs became easier owing to the lower charge injection barrier.

Table 2.1.2. Detailed electrical parameters of OFET devices for PIIG-BT and PIIG-TPD films

Condition		μ_{max} [$cm^2 V^{-1} s^{-1}$]	μ_{avg} [$cm^2 V^{-1} s^{-1}$]	$I_{on}/I_{off, avg}$	$V_{T, avg}$[c] [V]
PIIG-BT	As-cast	0.005	0.003 (±0.0009)[a]	1.0×10^7 ($\pm7.2\times10^6$)	48.3 (±3.1)
	150 °C	0.22	0.09 (±0.06)	1.3×10^7 ($\pm2.3\times10^7$)	41.5 (±7.1)
PIIG-TPD	As-cast	0.004	0.003 (±0.01)	2.4×10^6 ($\pm7.5\times10^5$)	10.1 (±3.5)
	150 °C	0.01	0.008 (±0.003)	4.1×10^6 ($\pm4.4\times10^6$)	8.3 (±6.4)
PIIG-TPD[b]	150 °C	0.001	6.0×10^{-4} ($\pm2.0\times10^{-4}$)	6.5×10^6 ($\pm7.5\times10^5$)	27.1 (±5.8)

[a]The standard deviation. [b]The fractionated PIIG-TPD (M_n = 32.0 kDa, PDI = 1.5).[c]The relatively higher V_T of PIIG-BT might originate from the larger injection barrier (due to the higher LUMO level) for electrons with respect to gold electrodes.

2.1.3 Conclusion

In conclusion, we have synthesized two A-A type IIG-based copolymers, PIIG-BT and PIIG-TPD consisting of all electron deficient units in the backbone. Unipolar *n*-channel charge transport behaviors were observed from the resulting copolymers. PIIG-BT exhibited electron mobility of up to 0.22 $cm^2 V^{-1} s^{-1}$ with high I_{on}/I_{off} of 10^7, which demonstrates the highest performance for *n*-type copolymers based on lactam core and is also comparable to the hitherto highest electron mobilities obtained from *n*-type copolymers. Feasibly, an A-A type strategy stimulated by this work can be extended to a wide range of design of new *n*-type materials.

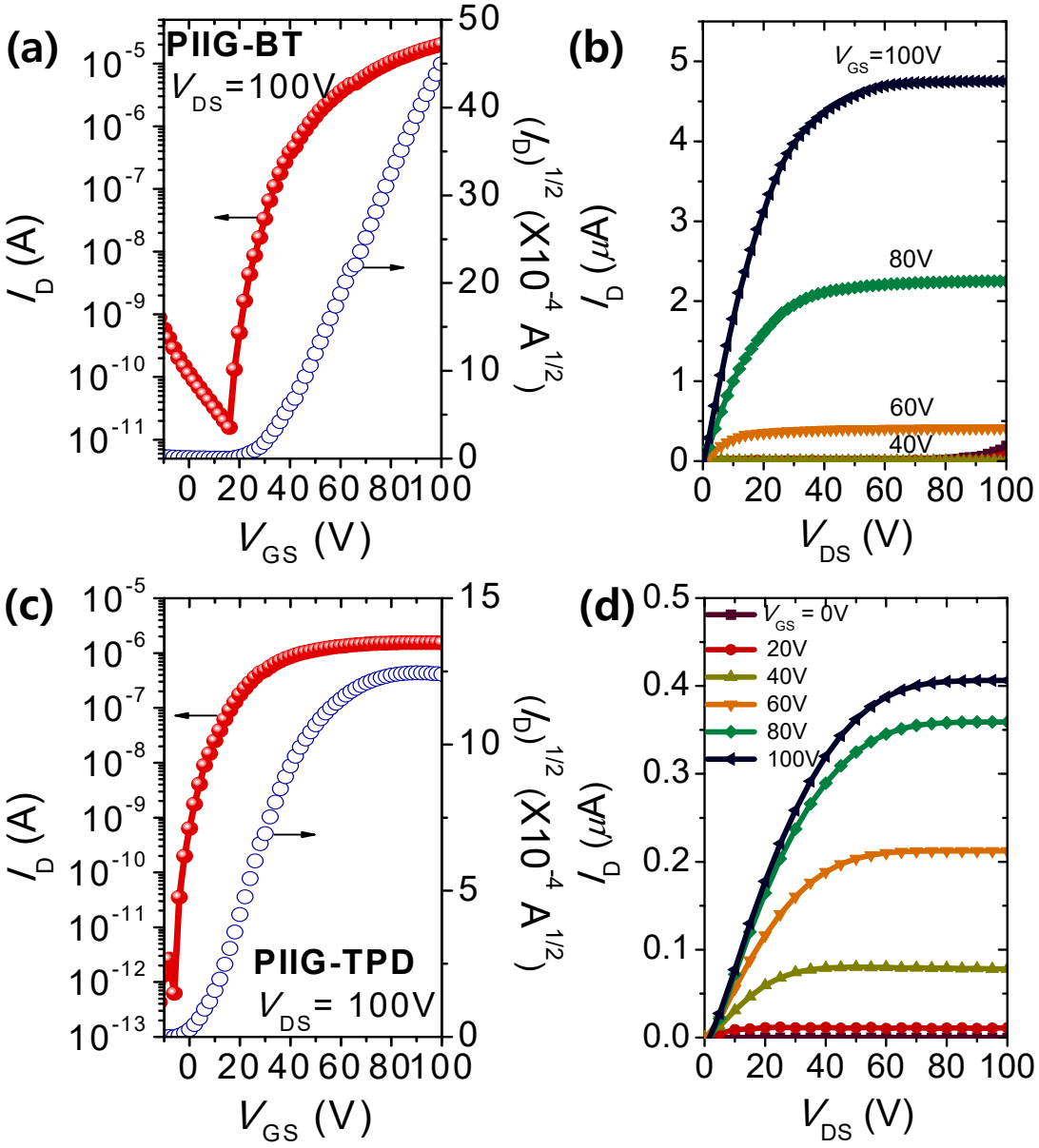

Figure 2.1.3. *I-V* Characteristics of FETs based on IIG-based copolymer thin films after annealing at 150 °C. (a,c) Transfer curves of (a) PIIG-BT and (c) PIIG-TPD at V_{DS} = +100V and (b,d) output characteristics of (b) PIIG-BT and (d) PIIG-TPD.

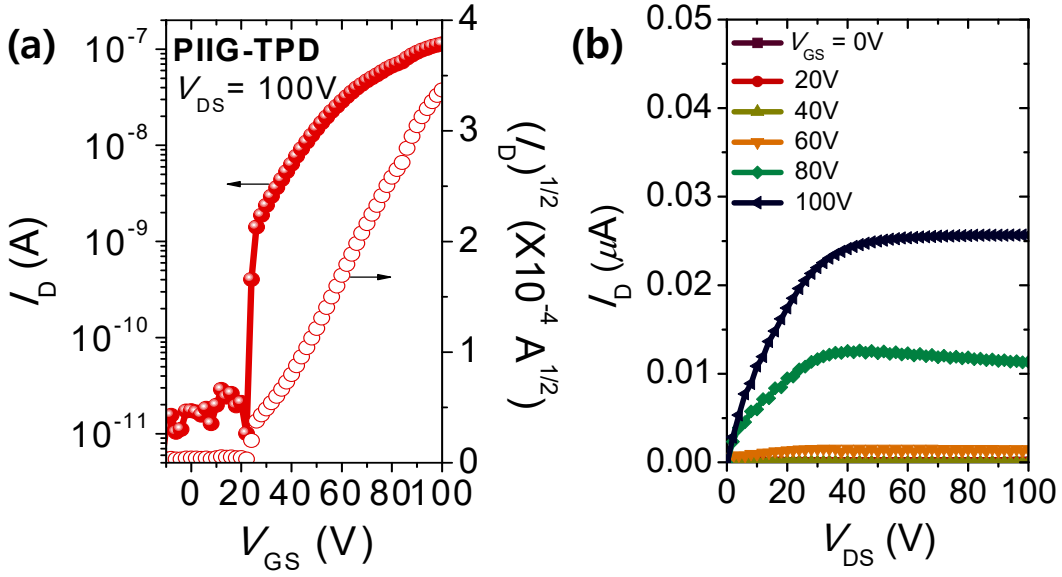

Figure 2.1.4. OFET performance of the fractionated PIIG-TPD (M_n = 32.0 kDa, PDI = 1.5) thin films after annealing at 150 °C. (a) Transfer curve at V_{DS} = +100V and (b) output characteristics.

2.1.4 Experimental Section

Materials and Instruments 6-Bromooxindole was purchased from CAPOT chemical company, 6-bromoisatin was purchased from TCI and other chemicals and solvent were purchased either from Aldrich or Acros and used without further purification. 6,6'-Dibromoisoindigo, 6,6'-(*N,N'*-2-octyldodecyl)-dibromoisoindigo (2), were synthesized according to the literature.[2, 29] ^{1}H NMR and ^{13}C NMR spectra were recorded on a Varian VNRS 600 MHz (Varian USA) spectrophotometer using $CDCl_3$ as solvent and tetramethylsilane (TMS) as the internal standard and MALDI MS spectra were obtained from Ultraflex III (Bruker, Germany). UV-VIS-NIR spectra were taken on UV-1800 (SHIMADZU) spectrometer. Number-average (M_n) and weight average (M_w) molecular weights, and polydispersity index (PDI) of the polymer products were determined by gel permeation chromatography (GPC) with Perkin-Elmer Series 200 using a series of mono disperse polystyrene as standards in THF (HPLC grade) at 313 K. Preparative GPC (pre-GPC) was performed on FUTECS HPLC System NS-4000 with Shodex GPC K-2004 column using a chloroform (HPLC grade) at 298 K. Cyclic voltammetry (CV) measurements were performed on AMETEK VersaSTAT 3 with a three-electrode cell in a nitrogen bubbled 0.1 M tetra-*n*-butylammonium hexafluorophosphate (*n*-Bu_4NPF_6) solution in acetonitrile at a scan rate of 50 mV/s at room temperature. A used as the Ag/Ag^+ (0.1 M of $AgNO_3$ in acetonitrile) reference electrode, platinum counter electrode and polymer coated platinum working electrode respectively. The Ag/Ag^+ reference electrode was calibrated using a ferrocene/ferrocenium redox couple as an external standard, whose oxidation potential is set at –4.8 eV with respect to zero vacuum level. The HOMO energy levels were obtained from the equation:

HOMO = – ($E_{ox}^{onset} - E_{(ferrocene)}^{onset}$ + 4.8) eV. The LUMO levels of polymers were obtained from the equation: LUMO = – (E_{red}^{onset} – $E_{(ferrocene)}^{onset}$ + 4.8) eV. Tapping-mode atomic force microscopy (AFM) measurements were performed using an Agilent 5500 scanning probe microscope (SPM) running with a Nanoscope V controller. The Rigaku high power X-ray diffractometer was used (D/MAZX 2500V/PC) to observe out-of-plane molecular packing in polymer films. X-ray diffraction (XRD) patterns were recorded under an X-ray power of 40 kV and a scan rate of 1 °/min.

Synthesis of 6,6'-(N,N'-2-octyldodecyl)-Pinacoldiboronisoindigo (3): 6,6'-(*N,N'*-2-octyldodecyl)-dibromoisoindigo (2 g, 2.04 mmol), bis(pinacolato)diboron (2.07 g, 8.16 mmol), potassium acetate (1.2 g, 12.24 mmol), and $PdCl_2$(dppf) (90 mg, 0.12 mmol) in anhydrous 1,4-dioxane (20 mL) were stirred at 80 °C for 2 d. The reaction was quenched by water and extracted with methylene chloride. The separated organic layer was washed with water and brine, then dried over $MgSO_4$ and removed under reduced pressure. The crude product was purified by column chromatography (silica gel, hexane to 50% methylene chloride in hexane) to afford 1.7 g (78%) of 3 as red-brown solid. ^{1}H NMR (600 MHz, $CDCl_3$) δ (ppm) 9.14 (d, 2H, *J*= 7.8 Hz), 7.48 (d, 2H, *J*= 7.8 Hz), 7.15 (s, 2H), 3.69 (d, 4H, *J*= 6.2 Hz), 1.95 (m, 2H), 1.40-1.26 (m, 88H), 0.87-0.84 (t, 12H, *J*= 6.6 Hz). ^{13}C NMR (150 MHz, $CDCl_3$) δ (ppm) 168.24, 144.61, 134.46, 129.01, 128.86, 124.38, 113.64, 84.18, 44.60, 36.26, 32.07, 32.05, 31.73, 30.16, 29.79, 29.78, 29.74, 29.50, 29.46, 26.57, 25.02, 22.83, 22.82, 14.27. Elemental Analysis: C, 75.96; H, 10.50; N, 2.61; O, 8.93 Found: C, 75.97; H, 10.52; N, 2.61; O, 8.85. MALDI-TOF-MS *m/z*: $[M]^{+\bullet}$ = 1076.24; calcd, 1075.25.

PIIG-BT: In a Schlenk flask, 6,6'-(*N,N'*-2-octyldodecyl)-dibromoisoindigo (2) (200 mg, 0.204 mmol) and 2,1,3-benzothiadiazole-4,7-bis(boronic acid pinacol ester) (79 mg, 0.204 mmol) was dissolved in toluene (7 mL), to this a solution of K_3PO_4 (217 mg, 1.02 mmol), tri-*o*-tolylphosphine (3.7 mg, 12.2 μmol) and deionized water (1.5 ml) was added. The mixture was vigorously stirred at room temperature under argon. After 30 min, $Pd_2(dba)_3$ (2.8 mg, 3.06 μmol) was added to the reaction mixture and stirred at 90 °C for 3 days (end capped with phenylboronic acid and bromobenzene). After then, the solution was precipitated in a mixture of methanol and ammonia (4:1 v/v, 250 mL). This was filtered off through paper filter under the vacuum, washed on Soxhlet apparatus with methanol (1d), acetone (1d) and hexane (1d) to remove low molecular weight. Finally, Soxhlet extracted chloroform fraction re-precipitated into methanol and filtered off through 0.45 μm Teflon filter. 170 mg (87%) of the polymer was recovered as a dark-green powder (M_n = 2.50 × 10^4 g/mol, PDI=1.32). ^{1}H NMR (600 MHz, $CDCl_3$) δ (ppm) 9.42-9.23 (br, 2H), 7.95-6.28 (br, 8H), 3.96-3.67 (br, 4H), 2.04-1.26 (br, 64H) 0.95-0.85 (br, 12H). Elemental Analysis: C, 77.77; H, 9.68; N, 5.85; O, 3.34; S, 3.35 Found: C, 77.03; H, 9.62; N, 5.74; O, 3.32; S, 3.26.

PIIG-TPD: In a Schlenk flask, 6,6'-(*N,N'*-2-octyldodecyl)-pinacoldiboronisoindigo (3) (219 mg, 0.204 mmol) and 1,3-dibromo-5-hexyl-thieno[3,4-c]pyrrole-4,6-dione (81 mg, 0.204 mmol) was dissolved in toluene (7 mL), to this a solution of K_3PO_4 (217 mg, 1.02 mmol), tri-*o*-tolylphosphine (3.7 mg, 12.2 μmol) and deionized water (1.5 ml) was added. The mixture was vigorously stirred at room temperature under argon. After 30 min, $Pd_2(dba)_3$ (2.8 mg, 3.06 μmol) was added to the reaction mixture and stirred at 90 ^oC for 3 days (end capped with phenylboronic acid and bromobenzene). After then, the solution was precipitated in a mixture of methanol and ammonia (4:1 v/v, 250 mL). This was filtered off through paper filter under the vacuum, washed on Soxhlet apparatus with methanol (1d), acetone (1d) and hexane (1d) to remove low molecular weight. Finally, Soxhlet extracted chloroform fraction re-precipitated into methanol and filtered off through 0.45 μm Teflon filter. 134 mg (61%) of the polymer was recovered as a black powder (M_n = 5.71 × 10^4 g/mol, PDI=3.30). ^{1}H NMR (600 MHz, $CDCl_3$) δ (ppm) 9.27-9.02 (br, 2H), 8.57-8.10 (br, 2H), 7.36-6.65 (br, 2H), 4.14-3.32 (br, 6H) 2.44-0.99 (br, 79H), 0.86-0.70 (br, 15H). Elemental Analysis: C, 77.37; H, 9.92; N, 3.87; O, 5.89; S, 2.95 Found: C, 77.12; H, 9.83; N, 3.74; O, 5.94; S, 2.81.

OFET Fabrication and Measurement Bottom-gate top-contact OFET devices based on the isoindigo (IIG) copolymers were fabricated on a highly *n*-doped Si substrate with thermally grown 300-nm-thick SiO_2 layer (C_i = 10 nFcm^{-2}), where the highly *n*-doped Si and SiO_2 layer were used as the gate electrode and dielectric, respectively. The surface of SiO_2/Si wafer was modified with *n*-octadecyltrimethoxysilane (OTS), as reported previously.[33-35] After cleaning the SiO_2/Si wafers with piranha solution (a 7:3 mixture of H_2SO_4 and H_2O_2), OTS solution (3 mM in trichloroethylene) was spin-coated on the SiO_2/Si substrate at 3000 rpm for 30 s. The OTS-coated wafers were exposed to ammonia vapor in a desiccator for 12 h. Then, the wafers were rinsed with toluene, acetone, and isopropyl alcohol. The contact angle (DI water) on the hydrophobic OTS-modified wafer was typically ~110°.

The IIG-based copolymers (PIIG-BT and PIIG-TPD) were dissolved in anhydrous chloroform (~3 mg mL^{-1}) and the polymer films were prepared on the OTS-modified SiO2/Si substrates by drop-casting method. Then, the polymer films were annealed on a hot plate at 150 °C for 30 min under N2 atmosphere. Gold electrodes (40 nm) were thermally evaporated through a shadow mask with a channel length (L) of 50 μm and width (W) of 1000 μm. The current−voltage characteristics were measured in a N_2-filled glovebox by using a Keithley 4200 semiconductor parametric analyzer. The field-effect mobility was calculated in the saturation regime using the following equation:

$$I_{DS} = ½(W/L)\mu C_i(V_G - V_T)^2$$

where I_{DS} is the drain current, W and L are the semiconductor channel width and length, respectively,

μ is the mobility, C_i is the capacitance per unit area of the gate dielectric, and V_G and V_T are the gate voltage and threshold voltage, respectively.

2.1.5. Reference

1. Mei, J.; Graham, K. R.; Stalder, R.; Reynolds, J. R. *Org. Lett.* **2010**, *12*, 660.
2. Stalder, R.; Mei, J.; Reynolds, J. R. *Macromolecules* **2010**, *43*, 8348.
3. Wang, E.; Ma, Z.; Zhang, Z.; Henriksson, P.; Inganäs, O.; Zhang, F.; Andersson, M. R. *Chem. Commun.* **2011**, *47*, 4908.
4. Wang, E.; Ma, Z.; Zhang, Z.; Vandewal, K.; Henriksson, P.; Inganäs, O.; Zhang, F.; Andersson, M. R. *J. Am. Chem. Soc.* **2011**, *133*, 14244.
5. Lei, T.; Cao, Y.; Zhou, X.; Peng, Y.; Bian, J.; Pei, J. *Chem. Mater.* **2012**, *24*, 1762.
6. Mei, J.; Kim, D. H.; Ayzner, A. L.; Toney, M. F.; Bao, Z. *J. Am. Chem. Soc.* **2011**, *133*, 20130.
7. Lei, T.; Dou, J. H.; Pei, J. *Adv. Mater* **2012**, *24*, 6457.
8. Lei, T.; Dou, J.-H.; Ma, Z.-J.; Yao, C.-H.; Liu, C.-J.; Wang, J.-Y.; Pei, J. *J. Am. Chem. Soc.* **2012**, *134*, 20025.
9. Zhao, X.; Wen, Y.; Ren, L.; Ma, L.; Liu, Y.; Zhan, X. *J. Polym. Sci., Part A: Polym. Chem.* **2012**, *50*, 4266.
10. Zhou, H.; Yang, L.; Stuart, A. C.; Price, S. C.; Liu, S.; You, W. *Angew. Chem.* **2011**, *123*, 3051.
11. Kim, J.; Han, A.-R.; Seo, J. H.; Oh, J. H.; Yang, C. *Chem. Mater.* **2012**, *24*, 3464.
12. Kim, G.; Yeom, H. R.; Cho, S.; Seo, J. H.; Kim, J. Y.; Yang, C. *Macromolecules* **2012**, *45*, 1847.
13. Cho, S.; Lee, J.; Tong, M.; Seo, J. H.; Yang, C. *Adv. Funct. Mater* **2011**, *21*, 1910.
14. Price, S. C.; Stuart, A. C.; Yang, L.; Zhou, H.; You, W. *J. Am. Chem. Soc.* **2011**, *133*, 4625.
15. Boudreault, P.-L. T.; Najari, A.; Leclerc, M. *Chem. Mater.* **2010**, *23*, 456.
16. Zou, Y.; Najari, A.; Berrouard, P.; Beaupré, S.; Réda Aïch, B.; Tao, Y.; Leclerc, M. *J. Am. Chem. Soc.* **2010**, *132*, 5330.
17. Piliego, C.; Holcombe, T. W.; Douglas, J. D.; Woo, C. H.; Beaujuge, P. M.; Fréchet, J. M. *J. Am. Chem. Soc.* **2010**, *132*, 7595.
18. Zhang, Y.; Hau, S. K.; Yip, H.-L.; Sun, Y.; Acton, O.; Jen, A. K.-Y. *Chem. Mater.* **2010**, *22*, 2696.
19. Guo, X.; Ortiz, R. P.; Zheng, Y.; Kim, M.-G.; Zhang, S.; Hu, Y.; Lu, G.; Facchetti, A.; Marks, T. J. *J. Am. Chem. Soc.* **2011**, *133*, 13685.

20. Beaupré, S.; Pron, A.; Drouin, S. H.; Najari, A.; Mercier, L. G.; Robitaille, A. l.; Leclerc, M. *Macromolecules* **2012**, *45*, 6906.

21. Chu, T. Y.; Lu, J.; Beaupré, S.; Zhang, Y.; Pouliot, J. R.; Zhou, J.; Najari, A.; Leclerc, M.; Tao, Y. *Adv. Funct. Mater* **2012**, *22*, 2345.

22. Cabanetos, C. m.; El Labban, A.; Bartelt, J. A.; Douglas, J. D.; Mateker, W. R.; Fréchet, J. M.; McGehee, M. D.; Beaujuge, P. M. *J. Am. Chem. Soc.* **2013**, *135*, 4656.

23. Hong, Y.-R.; Wong, H.-K.; Moh, L. C.; Tan, H.-S.; Chen, Z.-K. *Chem. Commun.* **2011**, *47*, 4920.

24. Ottone, C.; Berrouard, P.; Louarn, G.; Beaupré, S.; Gendron, D.; Zagorska, M.; Rannou, P.; Najari, A.; Sadki, S.; Leclerc, M. *Polym. Chem. (UK)* **2012**, *3*, 2355.

25. Stalder, R.; Mei, J.; Subbiah, J.; Grand, C.; Estrada, L. A.; So, F.; Reynolds, J. R. *Macromolecules* **2011**, *44*, 6303.

26. Grenier, F.; Berrouard, P.; Pouliot, J.-R.; Tseng, H.-R.; Heeger, A. J.; Leclerc, M. *Polym. Chem. (UK)* **2013**, *4*, 1836.

27. Hendriks, K. H.; Heintges, G. H.; Gevaerts, V. S.; Wienk, M. M.; Janssen, R. A. *Angew. Chem., Int. Ed.* **2013**, *52*, 8341.

28. Bao, Z.; Chan, W. K.; Yu, L. *J. Am. Chem. Soc.* **1995**, *117*, 12426.

29. Lei, T.; Cao, Y.; Fan, Y.; Liu, C.-J.; Yuan, S.-C.; Pei, J. *J. Am. Chem. Soc.* **2011**, *133*, 6099.

30. Zhou, H.; Yang, L.; You, W. *Macromolecules* **2012**, *45*, 607.

31. Ashraf, R. S.; Kronemeijer, A. J.; James, D. I.; Sirringhaus, H.; McCulloch, I. *Chem. Commun.* **2012**, *48*, 3939.

32. Dutta, G. K.; Han, A.; Lee, J.; Kim, Y.; Oh, J. H.; Yang, C. *Adv. Funct. Mater* **2013**, *23*, 5317.

33. Ito, Y.; Virkar, A. A.; Mannsfeld, S.; Oh, J. H.; Toney, M.; Locklin, J.; Bao, Z. *J. Am. Chem. Soc.* **2009**, *131*, 9396.

34. Schmidt, R. d.; Oh, J. H.; Sun, Y.-S.; Deppisch, M.; Krause, A.-M.; Radacki, K.; Braunschweig, H.; Könemann, M.; Erk, P.; Bao, Z. *J. Am. Chem. Soc.* **2009**, *131*, 6215.

35. Virkar, A.; Mannsfeld, S.; Oh, J. H.; Toney, M. F.; Tan, Y. H.; Liu, G.-y.; Scott, J. C.; Miller, R.; Bao, Z. *Adv. Funct. Mater* **2009**, *19*, 1962.

2.2. Herteroaromatic Spacer in A-A type Isoindigo Polymers for Ambipolar Charge Transport

Chapter 2.2 is reproduced in part with permission of "Use of Heteroaromatic Spacers in Isoindigo-Benzothiadiazole Polymers for Ambipolar Charge Transport" from Kim G. *et al*. *Phys. Chem. Chem. Phys.*, **2015**, *17*, 26512.

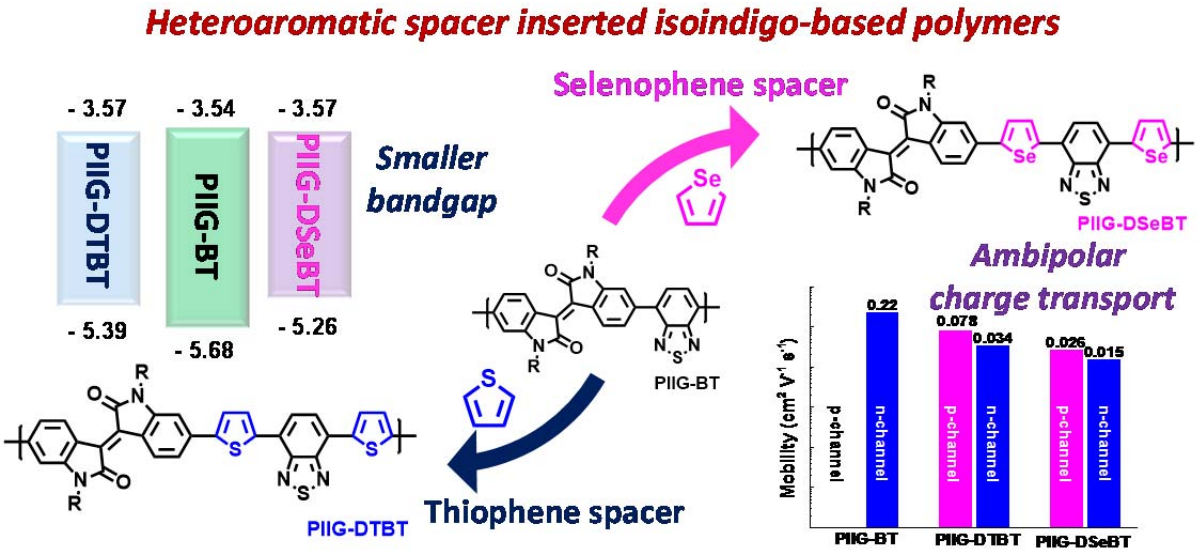

2.2.1 Introduction

π-Conjugated polymers for organic field-effect transistors (OFETs) have attracted considerable attention because of their easy modification of structure, solution processability, and low-cost device fabrication.[1-13] Owing to the capability to facilitate π-π stacking with a large overlapping area and intermolecular interactions induced by a macromolecular conjugated system involving alternating electron-rich and -deficient substituents, donor-acceptor (D-A) approach has found its foremost application in the molecular design and synthesis for the goal of improving the charge-carrier mobilities in OFETs.[11-19]

Within the class of D-A materials, isoindigo (IIG) unit has proven to be one of the most promising acceptor units for high-performance OFET materials. For example, by copolymerizing with numerous electron-rich blocks, great achievements in the resulting IIG-based D-A polymers for OFETs have been acquired in recent years.[20-26] Some IIG-oligothiophene polymers exhibited hole mobilities exceeding 1.0 $cm^2\ V^{-1}\ s^{-1}$.[24-28] Furthermore, the halogenated IIG-containing polymers pioneered by Pei and co-workers showed excellent ambipolar charge-carrier transport in IIG-based polymers, for

the first time.[29] On the other hand, *n*-type behavior is not universal in IIG-based polymers, limiting their application in *n*-type OFETs so far. In order to satisfy the demand for comparable performance characteristics for *n*-type OFETs, very recently our group reported an IIG-based polymer with electron-deficient benzothiadiazole (BT) as another acceptor unit in the polymer backbone, so-called A-A type, showing unipolar *n*-type OFET behavior with electron mobility of up to 0.22 $cm^2 V^{-1} s^{-1}$.[22]

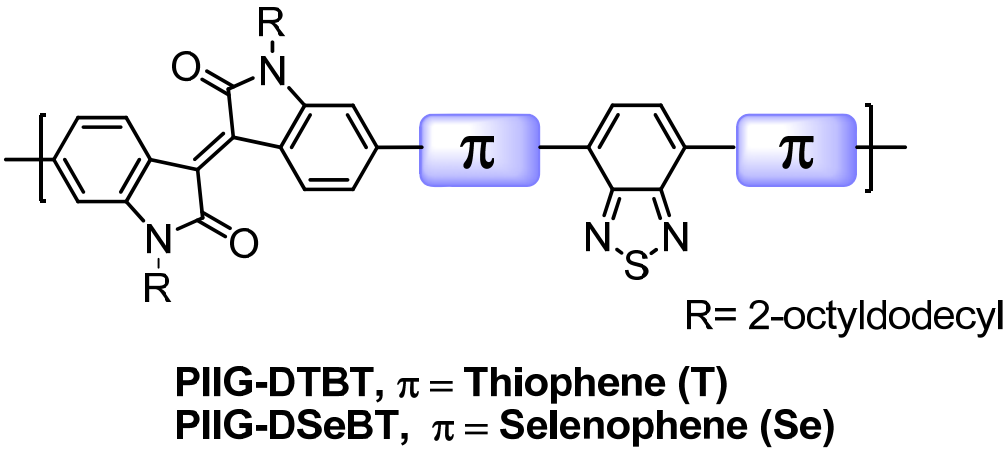

Figure 2.2.1. Molecular structure of PIIG-DTBT and PIIG-DSeBT.

Motivated by this intriguing result, in the present study, we devote our attention to the insertion of heteroaromatic spacer groups in between adjacent IIG and BT units along the backbone, with a view to exploring the impact of implanting heteroaromatic spacers into the IIG-BT polymer on the optoelectronic, electrochemical, and carrier-transport properties. Our choice for the heteroaromatic spacers is five-membered heterocyclic units such as thiophene (T) and selenophene (Se) because they can relieve the steric hindrance between the IIG and BT units, hence enhancing co-planarity of the polymer backbone, which would be preferable for charge transport by hopping.[30-32] The chemical structures of the studied polymers (PIIG-DTBT and PIIG-DSeBT) are shown in **Figure 1**. In this study, we present their syntheses, photophysical and electrochemical properties, and OFET performance. More than just tuning the optical properties and energy levels of the IIG-BT parent polymer, the incorporation of the heteroaromatic spacers affects the polarity in OFET devices, eventually leading to relatively well-balanced ambipolar transport behavior that is very rare for IIG-based polymers.

2.2.2 Results and Discussion

Scheme 2.2.1. Synthesis of PIIG-DTBT and PIIG-DSeBT

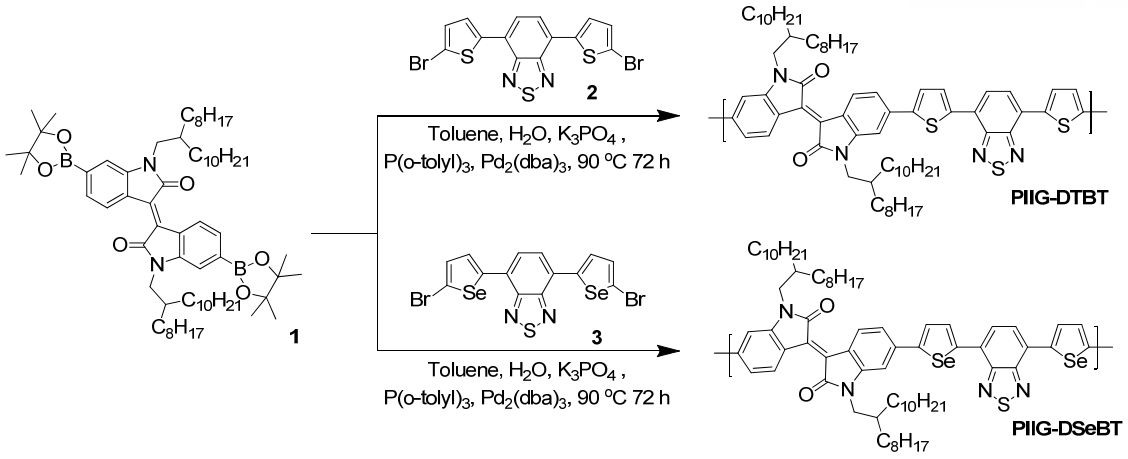

Synthetic approach and characterization The synthetic routes of the target polymers (PIIG-DTBT and PIIG-DSeBT) are outlined in Scheme 2.2.1. The key monomers, 6,6'-(*N,N'*-2-octyldodecyl)-pinacoldiboronisoindigo (1) (three steps; condensation, alkylation, and Miyaura borylation), 4,7-di(5'-bromo-2'-thienyl)-2,1,3-benzothiadiazole (2), and 4,7-di(5'-bromo-2'-selenienyl)-2,1,3-benzothiadiazole (3) (two steps for each compound; Stille coupling and bromination) were easily synthesized according to the previously reported methods. By copolymerizing the diborylated isoindigo and dibrominated monomers under Suzuki condition in degassed toluene/water, using K_3PO_4 as a base, $Pd_2(dba)_3$ as a catalyst, P(*o*-tolyl)$_3$ as the corresponding ligand, the target polymers, *i.e.*, PIIG-DTBT and PIIG-DSeBT, were obtained, respectively. The purification processes involved precipitation into methanol, followed by Soxhlet extraction with methanol, acetone, hexane, and chloroform to remove low molecular weight product. For chlorobenzene fraction of each polymer, gel-permeation chromatography (GPC) analysis against polystyrene standard exhibited a number-averaged molecular mass (M_n) of 6.5×10^3 and 1.6×10^4 g/mol and a polydispersity (PDI) of 2.13 and 3.45 for PIIG-DTBT and PIIG-DSeBT, respectively. Note that the reported M_n and the PDI by using room-temperature GPC (THF as eluent) only represented the soluble portion of each sample because each polymer was poorly soluble in THF.

Optical and electrochemical properties as well as theoretical calculations The UV-Vis spectra of PIIG-DTBT and PIIG-DSeBT in chloroform solution and in solid state on the quartz are shown in Figure 2.2.2a. The spectroscopic data of the polymers are summarized in Table 2.2.1. In both solution and films, the UV-Vis absorption spectra of two polymers are similar in shape, exhibiting a broad band covering the whole visible region. Compared to their absorption spectra in solution, the broader

absorption spectra in the solid state indicate that there are aggregations and/or orderly π-π stacking formed, which is beneficial for improving the charge mobility of the resulting films.

It is apparent that the absorption features for PIIG-DSeBT are obviously red-shifted relative to those of PIIG-DTBT. Thereby, the optical bandgap (E_g^{opt}) estimated from the absorption onset edge of the PIIG-DSeBT film is 1.46 eV, 150 meV smaller than that of PIIG-DTBT (1.61 eV), demonstrating that, in agreement with earlier studies,[34] the replacement of thiophene with selenophene in the polymer backbone results in both a red-shift of maximum absorbance and a reduction of optical bandgap. It is worth noting that, in comparison with PIIG-BT reported previously, the absorption maxima (λ_{max}) and onsets for both the polymers exhibit red-shifts, which is likely a result of the increase of the conjugation length and effective intramolecular charge transfer (ICT) after the insertion of electron-rich spacers (T or Se rings) along the backbones.

Cyclic voltammetry (CV) was performed to determine the energy levels of the polymers (Figure 2.2.2b). The CV curves were recorded as referenced to an Ag/Ag^+ (0.1M *n*-Bu_4NPF_6) electrode, which was calibrated by a ferrocene-ferrocenium (Fc/Fc^+) redox couple (4.8 eV below the vacuum level). Two polymers obviously display both *p*- and *n*-doping processes, in which their oxidative peaks are stronger than those of the reductive ones. The highest occupied molecular orbital (HOMO) and the lowest unoccupied molecular orbital (LUMO) energy levels are calculated to be -5.39/-3.57 eV for PIIG-DTBT and -5.26/-3.57 eV for PIIG-DSeBT, respectively. Compared with the energy levels of PIIG-BT (HOMO/LUMO = -5.68/-3.54 eV), both PIIG-DTBT and PIIG-DSeBT have significantly higher-lying HOMO levels, due to the presence of the electron-rich heteroaromatic units, whereas their LUMO levels remain almost unchanged. Besides, PIIG-DSeBT exhibits 0.13 eV higher-lying HOMO level relative to PIIG-DTBT, indicating that the electron-donating strength of the Se spacer is stronger than that of the T unit. Thus, the calculated electrochemical bandgap (E_g^{elec}) of PIIG-DSeBT is smaller than the value from PIIG-DTBT, which is consistent with the trend of E_g^{opt} deduced from the absorption onsets.

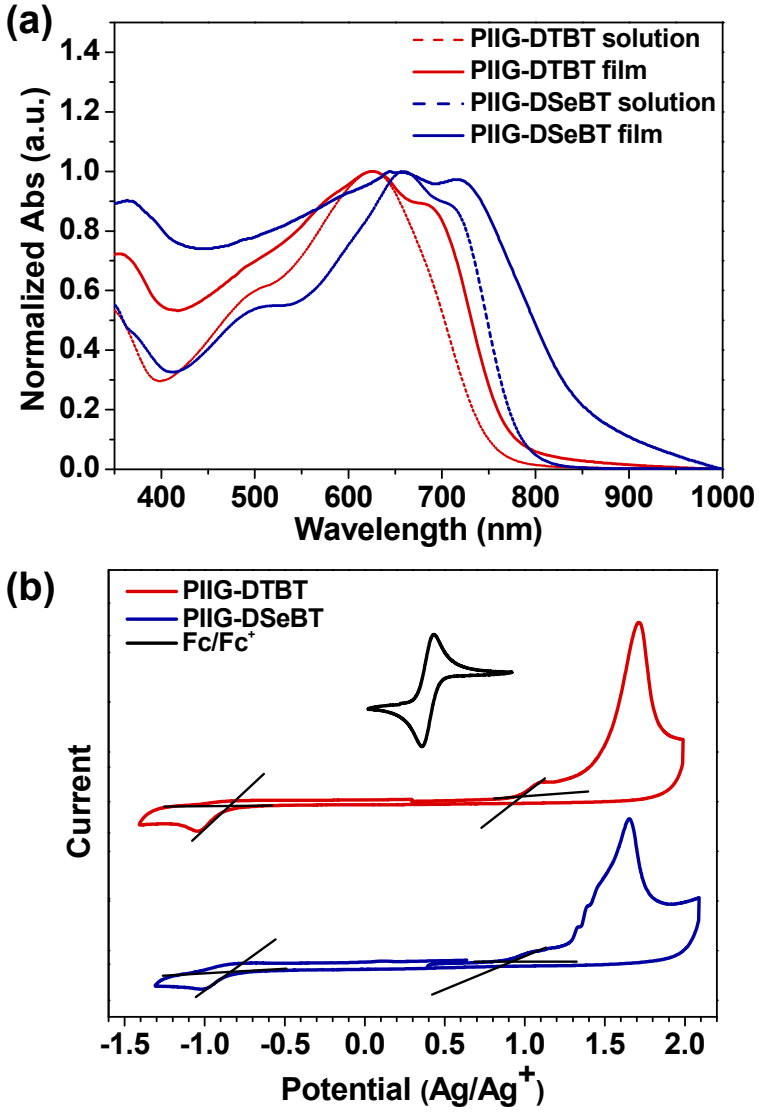

Figure 2.2.2. (a) Normalized solution and film absorption spectra and (b) Cyclic voltammograms of PIIG-DTBT and PIIG-DSeBT.

Table 2.2.1 UV-Vis absorption and electrochemical properties of the polymers

	λ_{max} (nm)	λ_{edge} (nm)	E_g^{opt} (eV)[a]	E_{HOMO} (eV)[b]	E_{LUMO} (eV)[b]	E_g^{elec} (eV)[c]
PIIG-DTBT	626	768	1.61	-5.39	-3.57	1.82
PIIG-DSeBT	667	851	1.46	-5.26	-3.57	1.69

[a]Calculated from the absorption band edge of the copolymer film, $E_g^{opt}=1240/\lambda_{edge}$. [b]Thin films in 0.1 M CH_3CN/*n*-Bu_4NPF_6, versus ferrocenium/ferrocene at 50 mVs^{-1}. HOMO and LUMO estimated from the onset oxidation and reduction potentials, respectively, assuming the absolute energy level of ferrocene/ferrocenium to be 4.8 eV below vacuum. [c]E_g^{elec} (eV) = −(LUMO − HOMO).

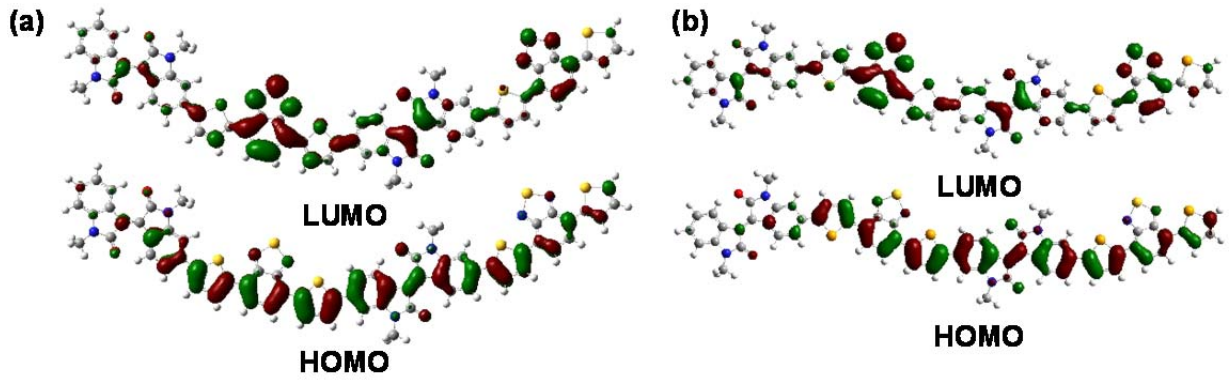

Figure 2.2.3. DFT-optimized geometries and charge-density isosurfaces for the HOMO and LUMO levels of (a) $(IIG\text{-}DTBT)_2$ and (b) $(IIG\text{-}DSeBT)_2$ model systems.

Distributions of HOMO and LUMO on the dimer systems of each polymer were calculated using the density functional theory (DFT) method at the B3LYP/6-31G level and are shown in Figure 2.2.3. The computational results reveal that the HOMOs are well delocalized along the polymer chain, but their LUMOs are slightly localized on the BT core. This somewhat contrasts with many D-A IIG-based polymers, in which the LUMOs are almost spanned over the IIG unit. Therefore, we believe that BT unit would have a slightly stronger electron affinity relative to IIG.

Thin-film microstructure analyses The film morphologies of the IIG-BT polymers containing heteroaromatic spacers were investigated using tapping-mode atomic-force microscopy (AFM). The thin films were prepared on *n*-octadecyltrimethoxysilane (OTS)-treated SiO_2/Si substrates by drop-casting method. As shown in Figure 2.2.4, both polymers formed densely packed nanofibrillar networks with the relatively smooth surface roughness less than 3.2 nm. PIIG-DTBT films exhibited more distinct nanofibrillar structures compared to PIIG-DSeBT films. In addition, fibrillar aggregates with larger grains were observed from the polymer films thermally annealed at 220 °C for 30 min, which may indicate the formation of efficient pathways for charge-carrier transport after the thermal annealing. To further investigate the crystallinity and molecular orientations, X-ray diffraction (XRD) analysis was carried out on the IIG-BT polymer thin films (see Figure 2.2.5). The spacer containing IIG-BT polymer thin films exhibited well-defined high order peaks up to (004), implying the formation of long-range lamellar packing in the thin films. PIIG-DTBT and PIIG-DSeBT films showed primary diffraction peaks at 2θ of 4.63° and 4.58°, respectively, which correspond to d(001)-spacing values of 19.07 Å and 19.28 Å, respectively (see Table 2.2.2). These are relatively reduced values compared to that of PIIG-BT (22.87 Å). This result demonstrates the positive effect of the heteroaromatic spacers on the dense molecular packing through the efficient donor-acceptor interaction between the polymer backbones. After annealing the polymer films, the diffraction peaks

became remarkably stronger and more intensified, and the (001) layer distances were reduced to 18.83 Å and 19.03 Å for PIIG-DTBT and PIIG-DSeBT, respectively. These results are also indicative of the positive effects of the thermal annealing for the charge transport. The PIIG-DTBT thin film exhibited relatively denser crystalline natures than the PIIG-DSeBT thin film, which may lead to better electrical performance in PIIG-DTBT films (*vide infra*).

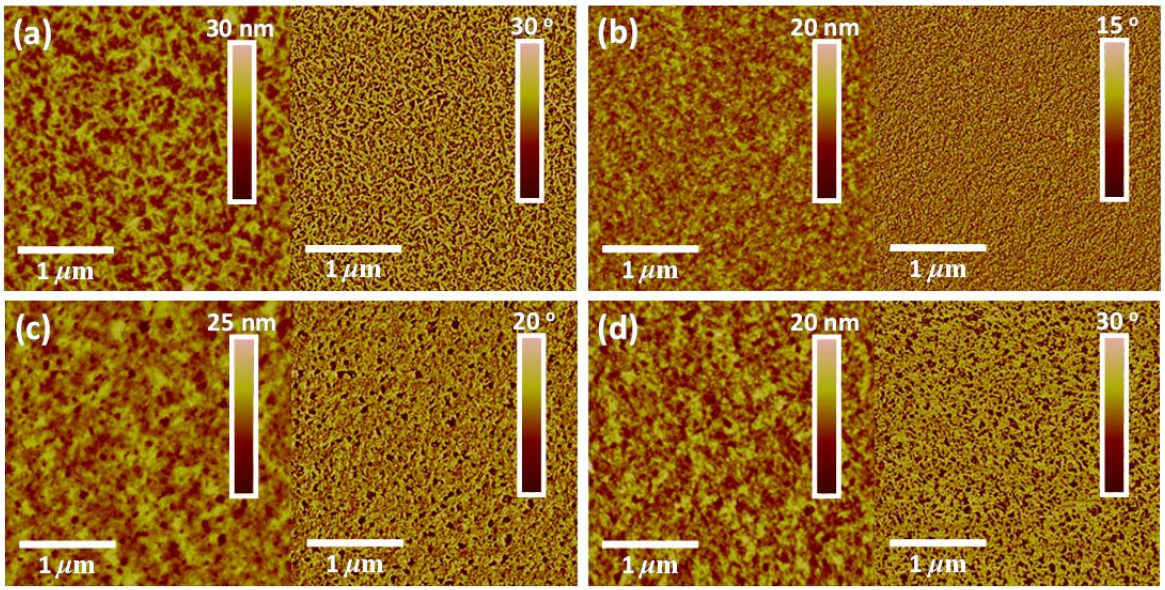

Figure 2.2.4. AFM height (left) and phase (right) images of drop-cast polymer films of {(a),(c)} PIIG-DTBT and {(b),(d)} PIIG-DSeBT. {(a),(b)} As cast films and {(c),(d)} annealed films at 220 °C on OTS-treated SiO_2/Si substrates.

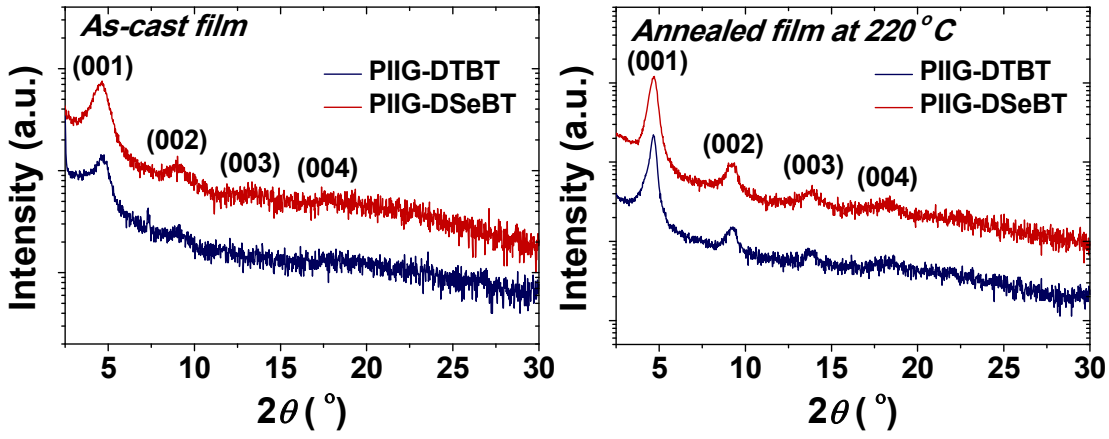

Figure 2.2.5. Out-of-plane X-ray diffraction (XRD) patterns of PIIG-DTBT and PIIG-DSeBT thin films: as-cast film (left) and annealed film at 220 °C (right).

Table 2.2.2 Peak assignments for the out-of-Plane XRD patterns obtained from PIIG-DTBT and PIIG-DSeBT thin films

Condition	(00*n*)	PIIG-DTBT		PIIG-DSeBT	
		2θ [^{o}]	*d*(001)-spacing [Å]	2θ [^{o}]	*d*(001)-spacing [Å]
As-cast film	(001)	4.63	19.07	4.63	19.07
	(002)	9.09	-	9.09	-
	(003)	-	-	-	-
	(004)	18.08	-	18.08	-
Annealed film at 220 ^{o}C	(001)	4.69	18.83	4.69	18.83
	(002)	9.29	-	9.29	-
	(003)	13.89	-	13.89	-
	(004)	18.34	-	18.34	-

Organic field-effect transistors In order to evaluate the electrical performance of heteroaromatic spacer containing IIG-BT polymers, we fabricated bottom-gate/top-contact OFET devices. The polymer films were drop-cast onto OTS-treated SiO_2/Si substrates from an IIG-based polymer solution in *o*-dichlorobenzene (3 mg mL^{-1}). Note that the solubility of PIIG-DSeBT was relatively poorer than that of PIIG-DTBT, thus heating the PIIG-DSeBT solution at high temperature (more than 100 ^{o}C) was required to suppress the precipitation of the polymer during the solution processing. For the heteroaromatic spacer inserted IIG-based polymer films, the annealed thin films exhibited significantly enhanced FET performance compared with the as-cast polymer thin films and the optimum thermal annealing temperature was found to be 220 ^{o}C (see Figure 2.2.6). Figure 2.2.7 shows the representative *I-V* characteristics of transfer and output curves from the optimized FETs annealed at 220 ^{o}C and their electrical performances are summarized in Table 2.2.3. In contrast with *n*-type electrical performance of PIIG-BT, both PIIG-DTBT and PIIG-DSeBT exhibited ambipolar characteristics, displaying typical V-shaped transfer curves. The ambipolar behaviors of PIIG-DTBT and PIIG-DSeBT can be mainly attributed to the smaller bandgaps induced by the extension of the conjugation length and the enhanced ICT of the spacer containing IIG-BT polymers. In particular, the energetically low-lying HOMO level of PIIG-BT prohibits the efficient injection of hole carriers with regard to the gold contact, whereas the higher-lying HOMO levels of PIIG-DTBT and PIIG-DSeBT allow more efficient injection of hole carriers relative to the gold contact, thereby leading to more pronounced ambipolar behaviors. The higher ambipolar FET performance was observed in the annealed PIIG-DTBT films ($\mu_{h,max}$ and $\mu_{e,max}$ of 7.8×10^{-2} and 3.4×10^{-2} cm^2 V^{-1} s^{-1}, respectively), which is most likely due to their optimized thin film microstructures compared to PIIG-DSeBT films ($\mu_{h,max}$ = 2.6×10^{-2} cm^2 V^{-1} s^{-1} and $\mu_{e,max}$ = 1.5×10^{-2} cm^2 V^{-1} s^{-1}). The slightly hole-dominant charge transport in their ambipolar characteristics is presumably due to the relatively smaller injection barriers for holes with respect to the gold contacts as well as to the delocalization of HOMO orbitals.

In addition, the threshold voltages (V_T) of PIIG-DSeBT were slightly smaller than PIIG-DTBT, owing to its easy turn-on characteristic induced by the lower bandgap. The complementary metal−oxide−semiconductor (CMOS)-like inverter characteristics of PIIG-DTBT and PIIG-DSeBT were also investigated using two identical ambipolar transistors. Output voltage (V_{OUT}) was monitored as a function of input voltage (V_{IN}) at a constant supply bias (V_{DD}). The voltage transfer characteristic (VTC) curves were shown in Figure 2.2.8, and high gains of 36.2 and 21.6 were obtained from PIIG-DTBT and PIIG-DSeBT, respectively. Although the asymmetry in mobility and threshold voltage in *p*- and *n*-channel modes should be complemented by further optimization of device architecture for both polymers, PIIG-DTBT exhibited a relatively higher gain because of the better ambipolar charge-carrier mobilities.

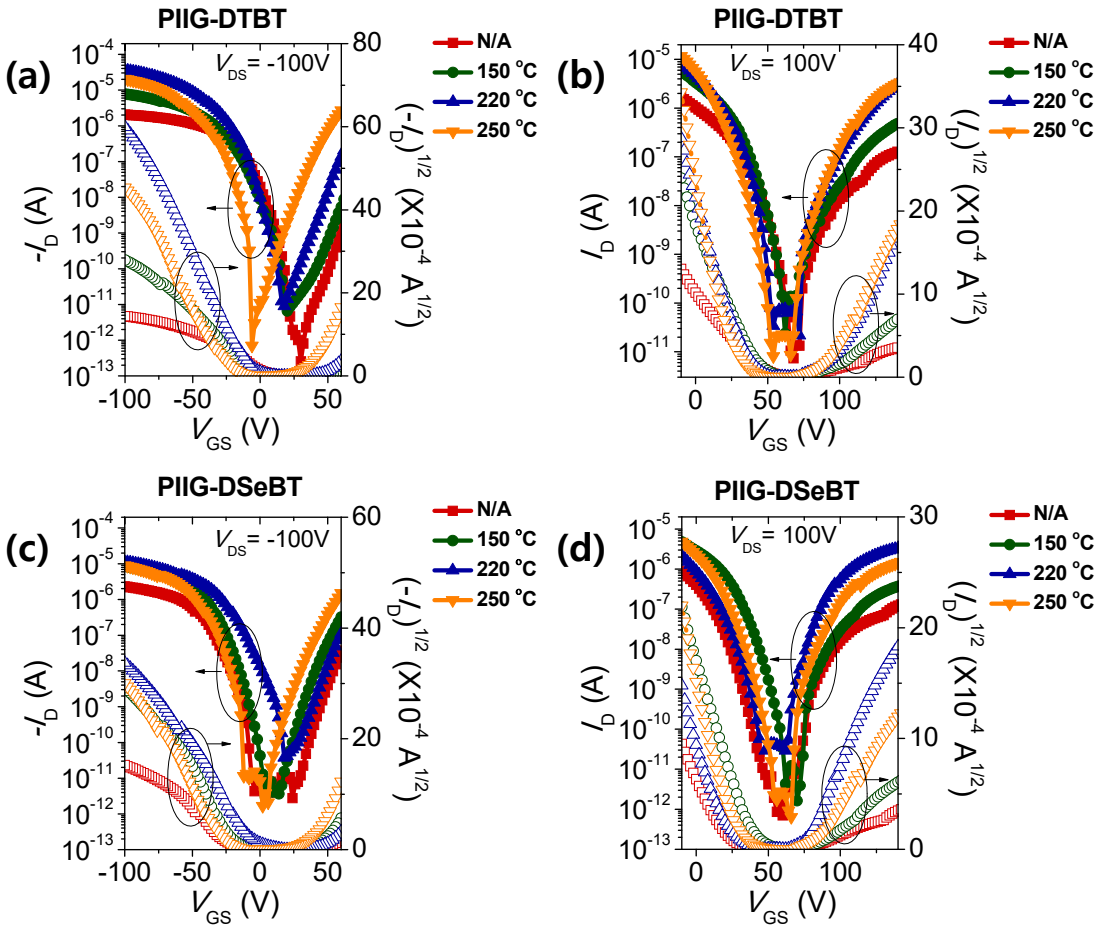

Figure 2.2.6. Ambipolar charge-transport characteristics of spacer containing IIG-BT polymers depending on annealing temperature: {(a),(b)} PIIG-DTBT and {(c),(d)} PIIG-DSeBT. The ambipolar transistor operating in {(a),(c)} hole- and {(b),(d)} electron-enhancement mode at $|V_{DS}|$=100V, respectively.

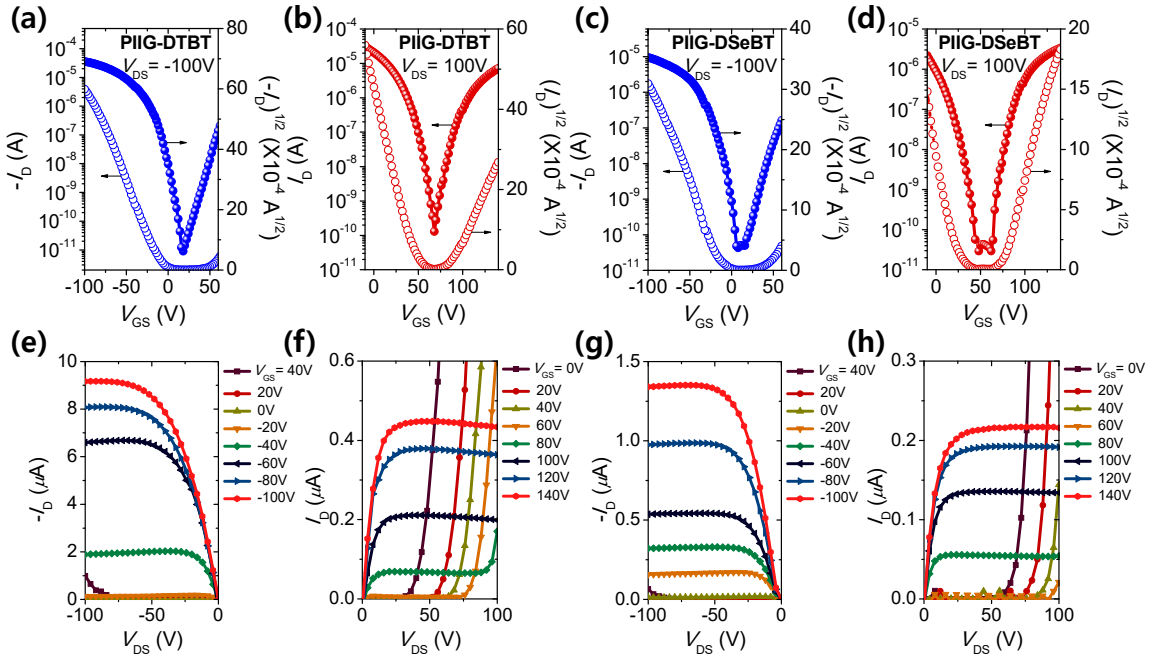

Figure 2.2.7. FET characteristics obtained from spacer-tuned BT polymer films annealed at 220 °C. Transfer curves of {(a),(b)} PIIG-DTBT and {(c),(d)} PIIG-DSeBT films at {(a),(c)} hole-, {(b),(d)} electron-enhancement operation with V_{DS} = −100 and +100 V, respectively. Output curves of {(e),(f)} PIIG-DTBT and {(g),(h)} PIIG-DSeBT films at {(e),(g)} *p*-, {(f),(h)} *n*-channel operation, respectively.

Table 2.2.3 OFET performance of spacer-tuned IIG-BT polymer thin films

Polymer[a]	*p*-channel				*n*-channel			
	$\mu_{h,max}$[b] [cm^2 V^{-1} s^{-1}]	$\mu_{h,avg}$[c] [cm^2 V^{-1} s^{-1}]	I_{on}/I_{off}	V_T [V]	$\mu_{e,max}$ [cm^2 V^{-1} s^{-1}]	$\mu_{e,avg}$ [cm^2 V^{-1} s^{-1}]	I_{on}/I_{off}	V_T [V]
PIIG-DTBT	7.8×10^{-2}	4.3×10^{-2} ($\pm1.9\times10^{-2}$)[d]	$>10^7$	-22.8	3.4×10^{-2}	1.4×10^{-2} ($\pm1.3\times10^{-2}$)	$>10^5$	95.6
PIIG-DSeBT	2.6×10^{-2}	2.0×10^{-2} ($\pm4.8\times10^{-3}$)	$>10^6$	-20.9	1.5×10^{-2}	5.3×10^{-3} ($\pm4.2\times10^{-3}$)	$>10^4$	87.2

[a]The polymer films were annealed at 220 °C and their FET performance of more than 10 devices was tested in a nitrogen atmosphere. [b]The maximum and [c]average mobility of the FET devices (L = 50 μm and W = 1000 μm). [d]The standard deviation.

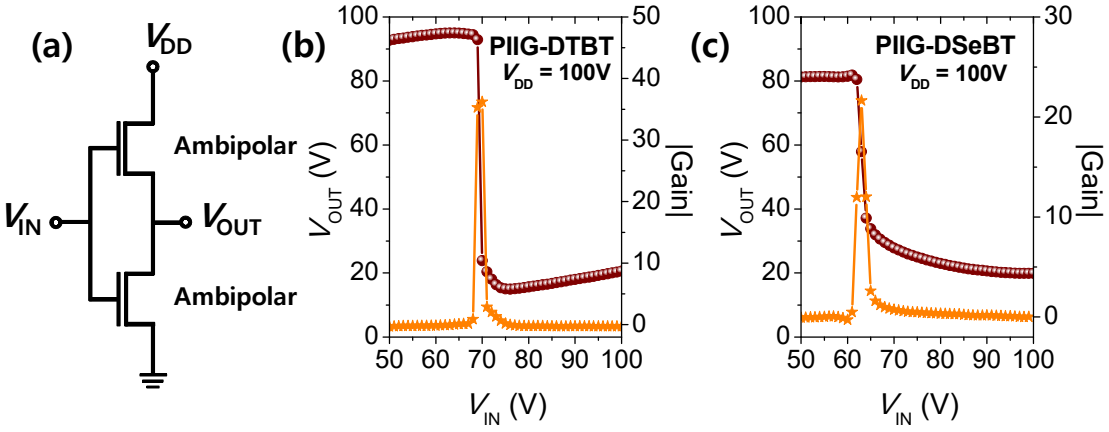

Figure 2.2.8. (a) Schematic of the complementary inverter structure. CMOS-like inverter characteristics of (b) PIIG-DTBT and (c) PIIG-DSeBT inverter (V_{DD} = 100 V).

2.2.3 Conclusions

Two new polymeric hybrids (PIIG-DTBT and PIIG-DSeBT) containing IIG, BT, and five-membered heteroaromatic spacers (T and Se) were synthesized and characterized, and their OFET performance was evaluated with the goal of attaining an understanding of the effect of the insertion of the spacers. Compared to PIIG-BT polymer directly incorporating IIG or BT units in the main backbone, the presence of the spacers regularly inserted to the polymeric backbones caused a red-shift, resulting in relatively narrow energy bandgaps. This is mainly attributed to the extended conjugation length and enhanced ICT. Both the polymers formed a well-ordered lamellar structure with fibrillar grains in the thin film. Beside the fine-tuning of optical properties and energy levels afforded by the simple structural modifications described in this study, the heteroaromatic spacers endowed both polymers with the changed polarity in OFET devices, resulting in relatively well-balanced ambipolar transport, and for PIIG-DTBT, the hole and electron mobilities as high as 7.8×10^{-2} and 3.4×10^{-2} $cm^2\ V^{-1}\ s^{-1}$ were achieved. To the best of our knowledge, this is the second example of IIG-based polymers presenting ambipolar characteristics in OFETs, reported to date.

2.2.4 Experimental

Materials and Instrument 6,6'-(*N,N'*-2-Octyldodecyl)-pinacoldiboronisoindigo (1), 4,7-di(5'-bromo-2'-thienyl)-2,1,3-benzothiadiazole (2), and 4,7-di(5'-bromo-2'-selenienyl)-2,1,3-benzothiadiazole (3) were synthesized according to the literature.[22, 33, 34] ^{1}H NMR spectra were recorded on a Varian VNRS 600 MHz (Varian USA) spectrophotometer using $CDCl_3$ as solvent and tetramethylsilane (TMS). UV-Vis spectra were taken on UV-1800 (SHIMADZU) spectrometer. Number-average (M_n) and weight

average (M_w) molecular weights, and polydispersity index (PDI) of the polymer products were determined by gel permeation chromatography (GPC) with Perkin-Elmer Series 200 using a series of mono disperse polystyrene as standards in THF (HPLC grade) at 313 K. Cyclic voltammetry (CV) measurements were performed on AMETEK VersaSTAT 3 with a three-electrode cell in a nitrogen bubbled 0.1 M tetra-*n*-butylammonium hexafluorophosphate (*n*-Bu_4NPF_6) solution in acetonitrile at a scan rate of 50 mV/s at room temperature. Ag/Ag^+ (0.1 M of $AgNO_3$ in acetonitrile) electrode, platinum wire and polymer coated glassy carbon electrode were used as the reference electrode, counter electrode and working electrode, respectively. The Ag/Ag^+ reference electrode was calibrated using a ferrocene/ferrocenium redox couple as an external standard, whose oxidation potential is set at -4.8 eV with respect to zero vacuum level. The HOMO energy levels were obtained from the equation HOMO= $-(E_{ox}^{onset} - E_{(ferrocene)}^{onset} + 4.8)$ eV. The LUMO levels of polymers were obtained from the equation LUMO= $-(E_{red}^{onset} - E_{(ferrocene)}^{onset} + 4.8)$ eV. Tapping-mode atomic force microscopy (AFM) measurements were performed using an Agilent 5500 scanning probe microscope (SPM) running with a Nanoscope V controller. The Rigaku high power X-ray diffractometer was used (D/MAZX 2500V/PC) to observe out-of-plane molecular packing in polymer films. X-ray diffraction (XRD) patterns were recorded under an X-ray power of 40 kV and a scan rate of 1 ^{o} min^{-1}.

OFET Fabrication and Measurement Bottom-gate top-contact OFET devices based on the spacer containing IIG-BT polymers were fabricated on a highly *n*-doped Si substrate with thermally grown 300-nm-thick SiO_2 layer (C_i = 10 nF cm^{-2}), where the highly *n*-doped Si and SiO_2 layer were used as the gate electrode and dielectric, respectively. The surface of SiO_2/Si wafer was treated with *n*-octadecyltrimethoxysilane (OTS), as reported previously.[15, 35] After cleaning the SiO_2/Si wafers with piranha solution (a 7:3 mixture of H_2SO_4 and H_2O_2), OTS solution (3 mM in trichloroethylene) was spin-coated on the SiO_2/Si substrate at 3000 rpm for 30 s. The OTS-deposited wafers were exposed to ammonia vapor in a desiccator for 12 h. Then, the wafers were rinsed with toluene, acetone, and isopropyl alcohol. The contact angle (DI water) on the hydrophobic OTS-treated wafer was typically ~110°. The spacer containing IIG-BT polymers (PIIG-DTBT and PIIG-DSeBT) were dissolved in anhydrous *o*-dichlorobenzene (~3 mg mL^{-1}) and the polymer films were prepared on the OTS-treated SiO_2/Si substrates by drop-casting method. Then, the polymer films were annealed on a hot plate at 220 °C for 30 min under N_2 atmosphere. Gold electrodes (40 nm) were thermally evaporated through a shadow mask with a channel length (L) of 50 μm and width (W) of 1000 μm. The current−voltage characteristics were measured in a N_2-filled glovebox by using a Keithley 4200 semiconductor parametric analyzer. The field-effect mobility was calculated in the saturation regime using the following equation:

$$I_{DS} = ½(W/L)\mu C_i(V_G - V_T)^2$$

where I_{DS} is the drain current, W and L are the semiconductor channel width and length, respectively, μ is the mobility, C_i is the capacitance per unit area of the gate dielectric, and V_G and V_T are the gate voltage and threshold voltage, respectively.

Suzuki-type polymerization

PIIG-DTBT: In a Schlenk flask, 6,6'-(*N,N'*-2-octyldodecyl)-pinacoldiboronisoindigo (1) (219 mg, 0.204 mmol) and 4,7-di(5'-bromo-2'-thienyl)-2,1,3-benzothiadiazole (2) (93 mg, 0.204 mmol) was dissolved in toluene (7 mL), to this a solution of K_3PO_4 (217 mg, 1.02 mmol), tri-*o*-tolylphosphine (3.7 mg, 12.2 μmol) and deionized water (1.5 ml) was added. The mixture was vigorously stirred at room temperature under argon. After 30 min, $Pd_2(dba)_3$ (3.7 mg, 4.08 μmol) was added to the reaction mixture and stirred at 90 °C for 3 d. After then, the solution was precipitated in a mixture of methanol and ammonia (4:1 v/v, 250 mL). This was filtered off through paper filter under the vacuum, washed on Soxhlet apparatus with methanol (1d), acetone (1d), hexane (1d) and chloroform (1d) to remove low molecular weight. Finally, chlorobenzene fraction was re-precipitated into methanol and filtered off through 0.45 μm Teflon filter. The polymer was obtained as chlorobenzene soluble black powder, 73 mg (32%) (M_n = 6.5×10^3 g/mol, PDI = 2.13). ^{1}H NMR (600 MHz, $CDCl_3$) δ (ppm) 9.22-9.20 (br, 2H), 8.16-7.84 (br, 6H), 7.52-6.67 (br, 6H), 3.76-3.50 (br, 4H) 2.11-1.26 (br, 64H), 0.87-0.84 (br, 12H). Elemental Analysis: C, 74.96; H, 8.63; N, 4.99; O, 2.85; S, 8.58 Found: C, 74.7; H, 8.52; N, 4.74; O, 3.24; S, 8.38.

PIIG-DSeBT: In a Schlenk flask, 6,6'-(*N,N'*-2-octyldodecyl)-pinacoldiboronisoindigo (1) (219 mg, 0.204 mmol) and 4,7-di(5'-bromo-2'-selenienyl)-2,1,3-benzothiadiazole (3) (113 mg, 0.204 mmol) was dissolved in toluene (7 mL), to this a solution of K_3PO_4 (217 mg, 1.02 mmol), tri-*o*-tolylphosphine (3.7 mg, 12.2 μmol) and deionized water (1.5 ml) was added. The mixture was vigorously stirred at room temperature under argon. After 30 min, $Pd_2(dba)_3$ (3.7 mg, 4.08 μmol) was added to the reaction mixture and stirred at 90 °C for 3 d. After then, the solution was precipitated in a mixture of methanol and ammonia (4:1 v/v, 250 mL). This was filtered off through paper filter under the vacuum, washed on Soxhlet apparatus with methanol (1d), acetone (1d), hexane (1d), and chloroform (1d) to remove low molecular weight. Finally, chlorobenzene fraction re-precipitated into methanol and filtered off through 0.45 μm Teflon filter. The polymer was obtained as chlorobenzene soluble black powder, 73 mg (32%) (M_n = 1.6×10^4 g/mol, PDI = 3.45). ^{1}H NMR (600 MHz, $CDCl_3$) δ (ppm) 9.17-8.89 (br, 2H), 8.18-6.38 (br, 10H), 3.74-3.49 (br, 4H), 2.10-1.02 (br, 64H), 0.88-0.72 (br, 12H). Elemental Analysis: C, 69.17; H, 7.96; N, 4.61; O, 2.63; S, 2.64 Found: C, 68.77; H, 7.66; N, 4.58; O, 2.62; S, 2.59.

2.2.5 Reference

1. Wang, C.; Dong, H.; Hu, W.; Liu, Y.; Zhu, D. *Chem. Rev.* **2011**, *112*, 2208.
2. Rivnay, J.; Jimison, L. H.; Northrup, J. E.; Toney, M. F.; Noriega, R.; Lu, S.; Marks, T. J.; Facchetti, A.; Salleo, A. *Nat. Mater.* **2009**, *8*, 952.
3. Beaujuge, P. M.; Fréchet, J. M. *J. Am. Chem. Soc.* **2011**, *133*, 20009.
4. Giri, G.; Verploegen, E.; Mannsfeld, S. C.; Atahan-Evrenk, S.; Kim, D. H.; Lee, S. Y.; Becerril, H. A.; Aspuru-Guzik, A.; Toney, M. F.; Bao, Z. *Nature* **2011**, *480*, 504.
5. Sirringhaus, H. *Adv. Mater.* **2005**, *17*, 2411.
6. McCulloch, I.; Heeney, M.; Bailey, C.; Genevicius, K.; MacDonald, I.; Shkunov, M.; Sparrowe, D.; Tierney, S.; Wagner, R.; Zhang, W.; Chabinyc, M. L.; Kline, R. J.; McGehee, M. D.; Toney, M. F. *Nat. Mater.* **2006**, *5*, 328.
7. Katz, H. E. *Chem. Mater.* **2004**, *16*, 4748.
8. Meijer, E.; De Leeuw, D.; Setayesh, S.; Van Veenendaal, E.; Huisman, B.-H.; Blom, P.; Hummelen, J.; Scherf, U.; Klapwijk, T. *Nat. Mater.* **2003**, *2*, 678.
9. Garnier, F.; Hajlaoui, R.; Yassar, A.; Srivastava, P. *Science* **1994**, *265*, 1684.
10. Guo, X.; Baumgarten, M.; Müllen, K. *Prog. Polym. Sci.* **2013**, *38*, 1832.
11. Lee, J.; Han, A.-R.; Kim, J.; Kim, Y.; Oh, J. H.; Yang, C. *J. Am. Chem. Soc.* **2012**, *134*, 20713.
12. Lee, J.; Han, A.-R.; Yu, H.; Shin, T. J.; Yang, C.; Oh, J. H. *J. Am. Chem. Soc.* **2013**, *135*, 9540.
13. Zaumseil, J.; Sirringhaus, H. *Chem. Rev.* **2007**, *107*, 1296.
14. Cortizo-Lacalle, D.; Arumugam, S.; Elmasly, S. E.; Kanibolotsky, A. L.; Findlay, N. J.; Inigo, A. R.; Skabara, P. J. *J. Mater. Chem.* **2012**, *22*, 11310.
15. Schmidt, R.; Oh, J. H.; Sun, Y.-S.; Deppisch, M.; Krause, A.-M.; Radacki, K.; Braunschweig, H.; Könemann, M.; Erk, P.; Bao, Z. *J. Am. Chem. Soc.* **2009**, *131*, 6215.
16. Kim, Y.; Hong, J.; Oh, J. H.; Yang, C. *Chem. Mater.* **2013**, *25*, 3251.
17. Kim, J.; Han, A.-R.; Seo, J. H.; Oh, J. H.; Yang, C. *Chem. Mater.* **2012**, *24*, 3464.
18. Lee, J.; Cho, S.; Seo, J. H.; Anant, P.; Jacob, J.; Yang, C. *J. Mater. Chem.* **2012**, *22*, 1504.
19. Suraru, S.-L.; Zschieschang, U.; Klauk, H.; Würthner, F. *Chem. Commun.* **2011**, *47*, 1767.
20. Stalder, R.; Mei, J.; Subbiah, J.; Grand, C.; Estrada, L. A.; So, F.; Reynolds, J. R. *Macromolecules* **2011**, *44*, 6303.
21. Mei, J.; Graham, K. R.; Stalder, R.; Reynolds, J. R. *Org. lett.* **2010**, *12*, 660.

22. Kim, G.; Han, A.-R.; Lee, H. R.; Lee, J.; Oh, J. H.; Yang, C. *Chem. Commun.* **2014**, *50*, 2180.

23. Grenier, F.; Berrouard, P.; Pouliot, J.-R.; Tseng, H.-R.; Heeger, A. J.; Leclerc, M. *Polym. Chem.* **2013**, *4*, 1836.

24. Wang, E.; Mammo, W.; Andersson, M. R. *Adv. Mater.* **2014**, DOI: 10.1002/adma.201304945.

25. Lei, T.; Cao, Y.; Fan, Y.; Liu, C.-J.; Yuan, S.-C.; Pei, J. *J. Am. Chem. Soc.* **2011**, *133*, 6099.

26. Lei, T.; Cao, Y.; Zhou, X.; Peng, Y.; Bian, J.; Pei, J. *Chem. Mater.* **2012**, *24*, 1762.

27. Mei, J.; Kim, D. H.; Ayzner, A. L.; Toney, M. F.; Bao, Z. *J. Am. Chem. Soc.* **2011**, *133*, 20130.

28. Lei, T.; Dou, J. H.; Pei, J. *Adv. Mater.* **2012**, *24*, 6457.

29. Lei, T.; Dou, J.-H.; Ma, Z.-J.; Yao, C.-H.; Liu, C.-J.; Wang, J.-Y.; Pei, J. *J. Am. Chem. Soc.* **2012**, *134*, 20025.

30. Kronemeijer, A. J.; Gili, E.; Shahid, M.; Rivnay, J.; Salleo, A.; Heeney, M.; Sirringhaus, H. *Adv. Mater.* **2012**, *24*, 1558.

31. Shahid, M.; Ashraf, R. S.; Huang, Z.; Kronemeijer, A. J.; McCarthy-Ward, T.; McCulloch, I.; Durrant, J. R.; Sirringhaus, H.; Heeney, M. *J. Mater. Chem.* **2012**, *22*, 12817.

32. Sirringhaus, H.; Brown, P.; Friend, R.; Nielsen, M. M.; Bechgaard, K.; Langeveld-Voss, B.; Spiering, A.; Janssen, R. A.; Meijer, E.; Herwig, P. *Nature* **1999**, *401*, 685.

33. Kim, G.; Yeom, H. R.; Cho, S.; Seo, J. H.; Kim, J. Y.; Yang, C. *Macromolecules* **2012**, *45*, 1847.

34. Kim, B.; Yeom, H. R.; Yun, M. H.; Kim, J. Y.; Yang, C. *Macromolecules* **2012**, *45*, 8658.

35. Ito, Y.; Virkar, A. A.; Mannsfeld, S.; Oh, J. H.; Toney, M.; Locklin, J.; Bao, Z. *J. Am. Chem. Soc.* **2009**, *131*, 9396.

Chapter 3 Isoindigo Modification to Thienoisoindigo for Organic Thin-Film Transistors

Chapter 3 is reproduced in part with permission of "A Thienoisoindigo-Naphthalene Polymer with Ultra-High Mobility of 14.4 $cm^2/V{\cdot}s$ That Substantially Exceeds Benchmark Values for Amorphous Silicon Semiconductors" from Kim G. *et al. J. Am. Chem. Soc.*, **2014**, *136*, 9477.

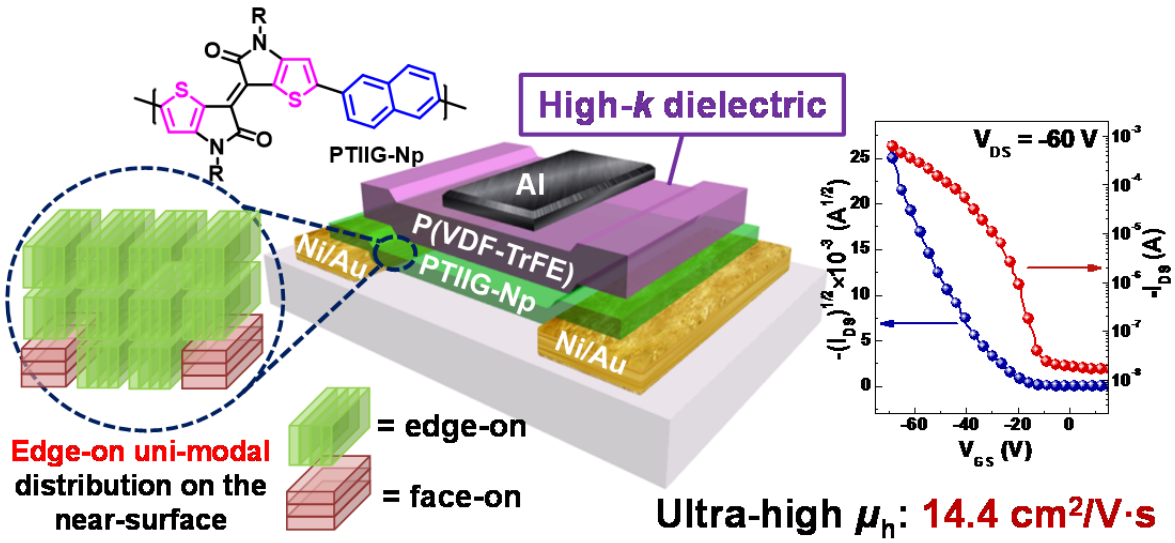

3.1 Introduction

High hopes exist for next-generation mobile displays, circuitry, and even radio frequency identification as well as e-paper,[1-4] each of which will doubtless have flexible, light-weight, large-area, and ultra low-cost requirements.[3-13] By taking full advantage of their versatile chemical synthesis, superior processability from solutions at low temperatures, as well as mechanical flexibility/ruggedness that semiconducting polymers inherently possess, solution-printable polymer-based thin-film transistors (TFTs), both as discrete transistors and in integrated circuits,[14,15] are now regarded as an ideal candidate for meeting all the aforementioned prerequisites. Unquestionably, benefiting from the maturation of the donor–acceptor (D–A) polymer approaches, most recently, great progress in the field of polymer TFTs has yielded state-of-the-art materials with high charge-carrier mobilities, reliably exceeding 3 $cm^2/V{\cdot}s$[16-19] and beyond for amorphous silicon semiconductors (a-Si:H, 0.5–1.0 $cm^2/V{\cdot}s$).[20] Such a vigorous boost in TFTs performance is most frequently associated with the D–A frameworks in which either diketopyrrolopyrrole (DPP) or isoindigo (IIG), as a polar

bicyclic lactam electron-deficient unit, was incorporated with electron-rich heteroacenes, such as thiophene and selenophene derivatives.[16-19,21-23]

Although exploring DPP- or IIG-based D-A polymers as well as shedding light on their high charge-carrier mobilities are still of great interest in the polymer academic community, the research in the area of these materials is almost reaching a plateau, threatened by development of strong alternative high-performance pigments. In a timely manner given the need for newer competitive materials, in 2012, McCulloch and co-workers disclosed a thiophene-implanted IIG unit, thienoisoindigo (TIIG), by modulating from the outer arylene groups of IIG to five-membered heterocyclic aromatic rings.[24] Consequently, the unique structural features of TIIG are capable of (i) improving co-planarity to the molecular plane *via* S···O interactions and (ii) enhancing the charge delocalization *via* a quinoidal structure of the backbone,[24-26] which can lead to better molecular ordering, π-conjugation, and charge transport efficiency.[5,27,28]

Shortly thereafter, it was widely expected that superior TFTs performance would be possible with a suitable molecular set-up of TIIG-containing D–A systems, thus creating various TIIG-based polymer semiconductors with heteroacene building blocks as a novel polymer design. Disappointingly, it turned out that the observed mobilities were no greater than ~0.3 $cm^2/V \cdot s$[24-26,29] that was one to three orders of magnitude lower than those obtained for current DPP- or IIG-containing semiconductors. This is probably due to the suppression of the full potential merits of TIIG unit within such structures, rather than its intrinsic property limitations; nevertheless, it is undeniably a setback for in this field. Very recently, we found that the geometric skeletons of the donors in D–A polymers with an identical acceptor could reflect the interchain π-π stacking as well as carrier mobility dynamics, rather than inserting electron-rich heteroacene donors into the backbone to further strengthen intramolecular charger transfer.[30]

Herein, we depart from the common choice of the heteroacene-based donors and focus on employing acene-based centrosymmetric donor unit for TIIG-based platform. Using commercially available naphthalene (Np) as the simplest fused centrosymmetric acene, we present an easily accessible TIIG-containing D-A polymer, poly(thienoisoindigo-*alt*-naphthalene) (abbreviated as PTIIG-Np, see Figure 3.1a for its molecular structure), and comprehensively describe its thin-film properties and transistor characteristics. PTIIG-Np shows excellent *p*-type dominant TFTs performance, with hole mobility of 5.8 $cm^2/V \cdot s$ employing common poly(methyl methacrylate) (PMMA) dielectric in a top gate structure. Furthermore, an unprecedented mobility of up to 14.4 $cm^2/V \cdot s$ is achieved from the PTIIG-Np TFTs adopting a high-*k* gate polymer dielectric poly(vinylidenefluoride-trifluoroethylene) (P(VDF-TrFE)), which is the highest mobility value among lactam-based polymers reported in the literature so far.

3.2 Results and Discussion

Synthetic Strategies, Synthesis, and Characterization: Our target polymer, PTIIG-Np (Figure 3.1a), was synthesized *via* Pd-catalyzed Suzuki polymerization between (*E*)-2,2'-dibromo-4,4'-bis(2-octyldodecyl)-[6,6'-bithieno[3,2-*b*]pyrrolylidene]-5,5'(4*H*,4'*H*)-dione and 2,6-bis(4,4,5,5-tetramethyl-1,3,2-dioxaborolan-2-yl)naphthalene, followed by Soxhlet extraction to remove impurities and undesired molecular weight fractions (see Scheme 3.1. for polymerization and syntheses of all the intermediates and their characterizations in Supporting Information). PTIIG-Np (M_n = 21.0 kDa using PS/THF standard) has excellent solubility in common organic solvents (THF, chloroform, toluene, etc.) and forms uniform thin films by spin-coating. As depicted in Figure 3.1b, PTIIG-Np shows dual-band absorptions in the region of 330–1100 nm, covering the whole visible to near-infrared range. Compared to those in solution, the absorption peaks of the thin films are not only red-shifted, but the intensity of 0–0 vibrational transition relative to 0–1 is also increased, thus becoming a broader band at the low-energy region. This indicates that the molecules in solid state undergo molecular organization to form more ordered structures, most likely as a result of the strong D–A interactions.

Cyclic voltammetry was used to estimate the frontier molecular orbital energy levels (Table 3.1). The highest occupied molecular orbital (HOMO) and lowest unoccupied molecular orbital (LUMO) levels are estimated to be -5.12 eV and -3.49 eV, respectively (Figure 3.1c). The ionization potential (IP, |HOMO|) of PTIIG-Np, measured by ultraviolet photoelectron spectroscopy (UPS) in air, is also found to be *ca.* -5.10 eV (Table 3.1), which is notably greater than that of P3HT (~-4.7 eV), often referred to as the 'fruit fly' of organic semiconductors.[7,31] The low-lying HOMO energy level is expected to be beneficial for increasing ambient stability of the polymer against oxidation as well as reducing the hole injection barrier between a gold source electrode and *p*-type semiconductor, which consequently would improve the device performance.

Upon B3LYP/6-31g** calculation on the trimer length oligomer with isobutyl groups, it is apparent that the HOMO is delocalized along the polymer chain, whereas the LUMO is somewhat concentrated on the TIIG core (Figure 3.1d). Thus, the nature of PTIIG-Np is considering *p*-channel dominant ambipolar TFT characteristics achievable (*vide infra*). The HOMO/LUMO energies obtained from the calculations of IP and optical bandgap are 5.10/3.74 eV and in very close agreement with the experimental data. In addition, this reveals that the intra twist (θ_1) within centro-symmetric ketopyrrole cores is ≤0.4°, while the inter torsion (θ_2) of 18.6–25.7° exists between TIIG and neighboring Np subunits (Figure 3.1e).

Scheme 3.1. Synthetic routes of PTIIG-Np.[a]

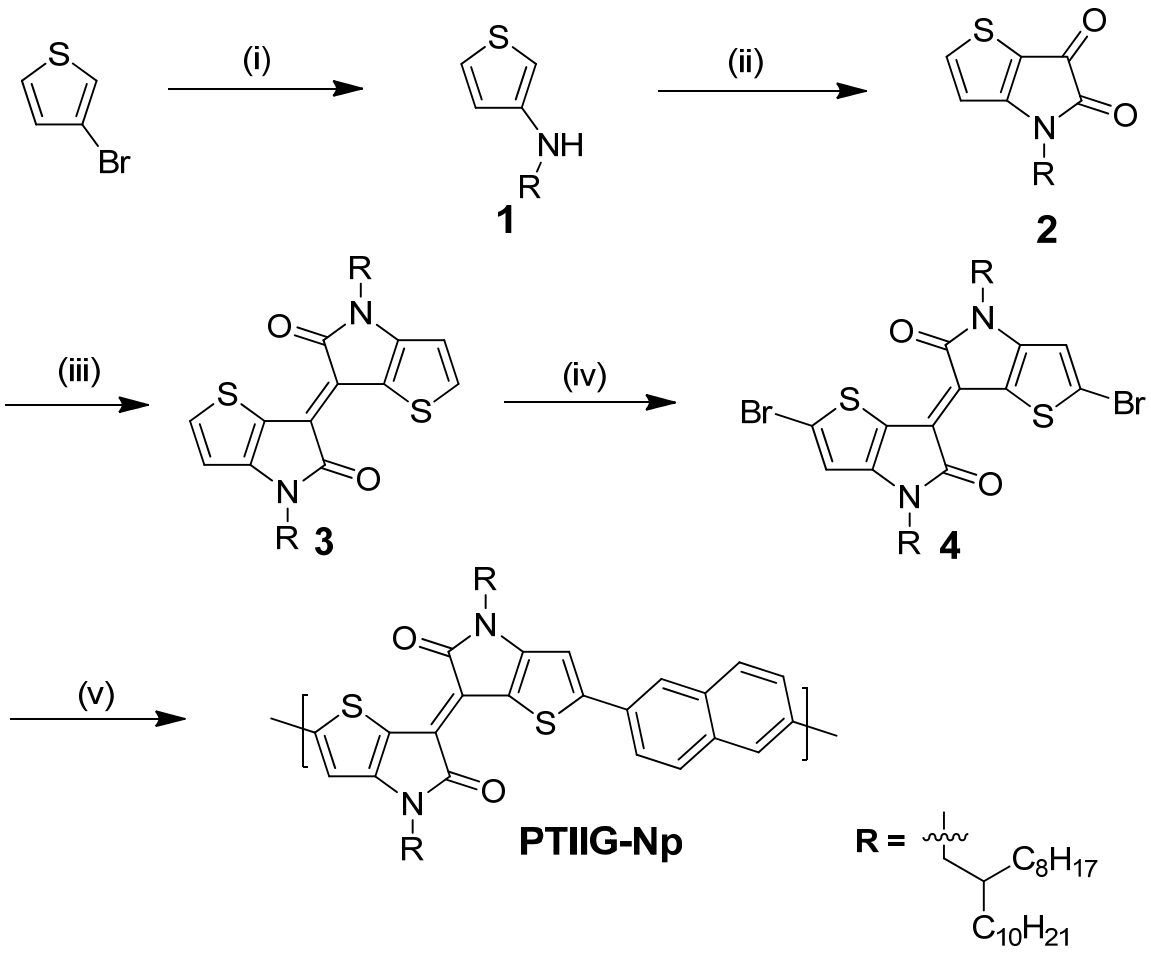

[a]Reagents and conditions: (i) 2-Octyldodecane-1-amine, Cu, CuI, K_3PO_4, dimethyl aminoethanol, reflux, 48 h, 41%; (ii) Oxalyl chloride, triethylamine, DCM, r.t., overnight, 40%; (iii) Lawesson's Reagent, toluene, 60°C, 2h, 35%; (iv) NBS, THF, r.t., overnight, 70%; (v) Suzuki polymerization, 2,6-*bis*(4,4,5,5-tetramethyl-1,3,2-dioxaborolan-2-yl)naphthalene, toluene, H_2O, K_3PO_4, P(*o*-tolyl)$_3$, $Pd_2(dba)_3$, 90°C, 72h, 59%.

Fabrication of Solution-processed TFTs and I–V Characterizations: We built high-performance TFT devices using PTIIG-Np polymer film (from 1,2,4-trichlorobenzene solution, ~5 mg mL^{-1}). The devices were fabricated in a top-gate and bottom-contact (TG-BC) configuration, with pre-patterned Ni (t~3 nm) /Au (t~12 nm) source-drain electrodes and PMMA acting as the gate dielectric, which was then spin-cast onto the polymer semiconductor layer. To explore the thermally induced PTIIG-Np ordering effect, the semiconductor layers were annealed at various temperatures (80, 150, 200, 250, and 310 ^{o}C) before spin-coating the dielectric layer. Al gate electrode was then deposited by thermal evaporation to complete the TFT structure.

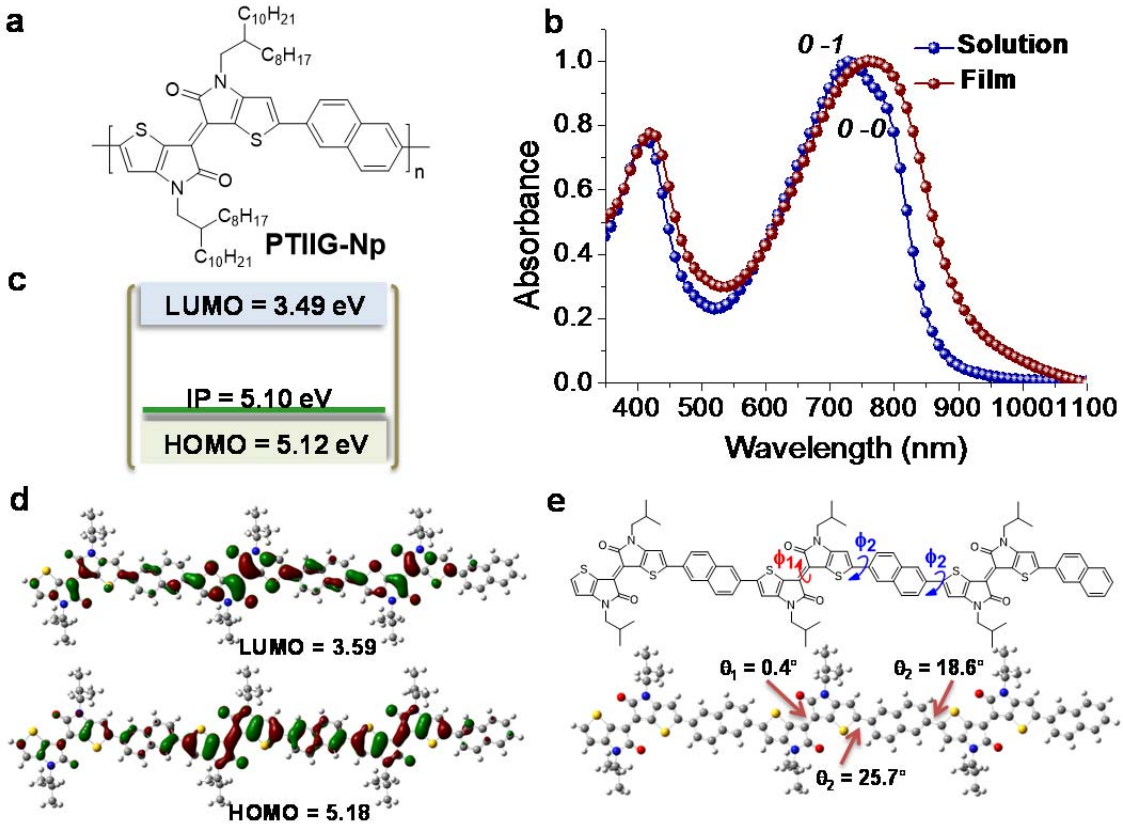

Figure 3.1. Chemical structure, Ultraviolet absorption spectra, Energy-level diagrams, and Energy-minimized structure at the B3LYP/6-31G** level. a, Structure of PTIIG-Np. (b) Normalized ultraviolet-visible absorption spectra of PTIIG-Np in $CHCl_3$ solution and as a thin film on quartz substrate. c, HOMO and LUMO levels determined by the thin films using cyclic voltammetry (CV) calibrated by the Fc/Fc^+ redox couple as an external standard. IP was also measured by ultraviolet photoelectron spectroscopy (UPS) technique. d, DFT-optimized geometries and charge-density isosurfaces for the trimeric system with a visualization of the HOMO and LUMO molecular orbitals (green and red represent the isosurfaces (iso value = 0.02) of the opposite phase of the wave functions). e, Calculated dihedral angles of the trimer structure.

Table 3.1. Optophysical properties of PTIIG-Np

	M_n (kDa)	PDI	IP[a]	λ_{max}^{sol} (nm)[b]	λ_{max}^{film} (nm)	E_g^{opt} (eV)[c]	E_{HOMO} (eV)[d]	E_{LUMO} (eV)[d]	E_g^{CV} (eV)[e]
PTIIG-Np	21.0	4.87	5.10	730	759	1.36	-5.12	-3.49	1.63

[a]Measured by an ambient ultraviolet photoelectron spectroscopy (UPS) technique; [b]Chloroform solution; [c]Determined from the onset of the electronic absorption spectra; [d]Cyclic voltammetry determined with Fc/Fc^+ (E_{HOMO} = -4.80 eV) as the external reference; [e]$E_g^{CV} = E_{LUMO} - E_{HOMO}$.

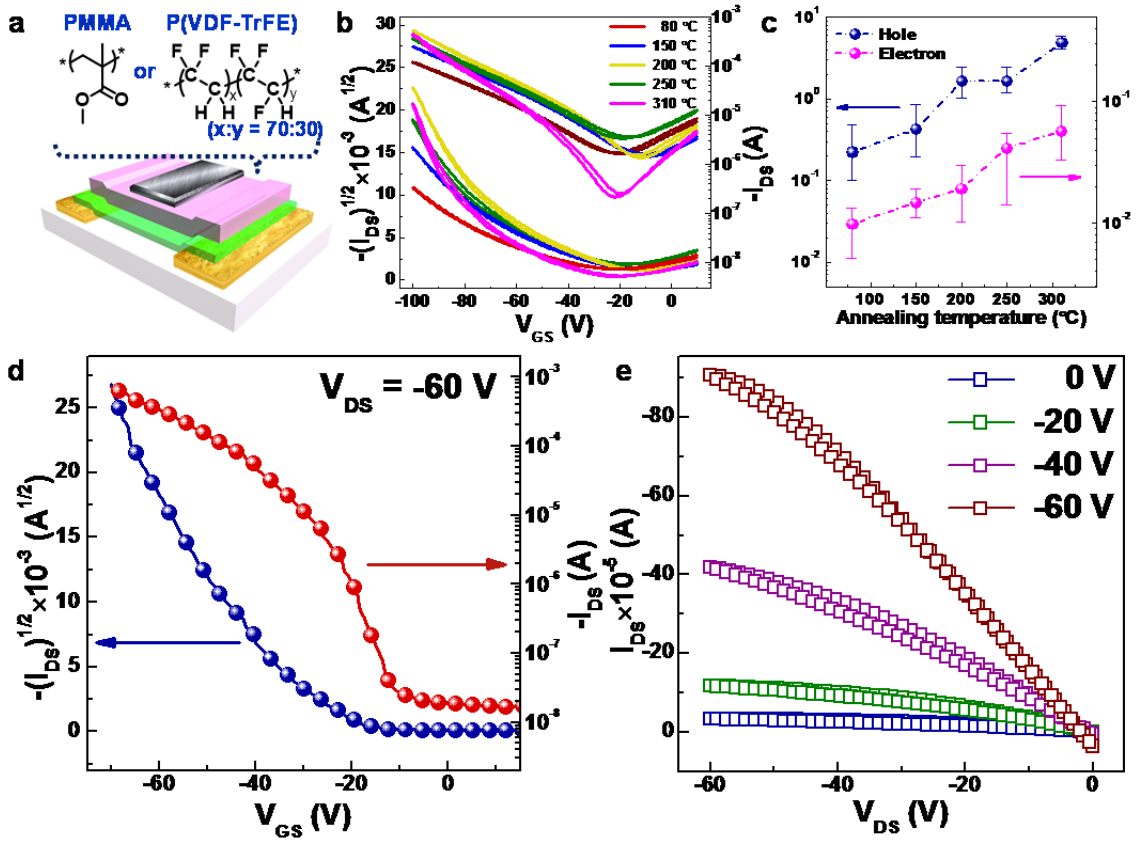

Figure 3.2. Device geometry of solution-processed PTIIG-Np TFTs and their electrical characteristics. a, Schematic cross-section of the top-gate and bottom-contact (TG-BC) geometry and the chemical structures of PMMA and P(VDF-TrFE) (as the gate dielectric layer. b,c, Transfer curves of PTIIG-Np devices with PMMA dielectric at -100 V of V_{DS} (channel width (W): 1 mm, length (L): 20 μm), of which semiconductor films were annealed at different temperatures (b) and hole and electron charge carrier mobility distributions based on various annealing temperatures (c). d,e, Transfer (d) and output (e) characteristics for PTIIG-Np TFTs after thermal annealing at 310 ^{o}C with P(VDF-TrFE) gate insulator (channel width (W): 1 mm, length (L): 50 μm), where the devices were additionally cured at 160 ^{o}C after spin-coating of the gate dielectric layer on the top of semiconductor surface, in order to suppress the crystalline β-phase induced by the large ferroelectric properties.

In pre-patterned electrodes, the channel width (W) and length (L) are 1 mm and 20 μm for the devices with PMMA (Figure 3.2a). Device fabrication and characterization were performed in a nitrogen gas filled glovebox (oxygen and moisture <20 ppm). The experimental details regarding TFT fabrication and surface modification are described in the Experimental section. Figure 3.2b exhibits the transfer curves tested from the PTIIG-Np TFTs with PMMA dielectric layer, showing *p*-type dominant ambipolar characteristics, and their electrical properties are summarized in Table 3.2.

Table 3.2. Summary of TFT performance characteristics for PTIIG-Np semiconductor with different gate dielectrics

Condition[a]		*p*-channel				*n*-channel		
Insulator (thickness)	T [°C]	$\mu_{h,max}$ [$cm^2/V{\cdot}s$]	$\mu_{h,avg}$ [$cm^2/V{\cdot}s$]	V_{th} [V]	$R_c{\cdot}W$ [$\Omega{\cdot}cm$]	$\mu_{e,max}$ [$cm^2/V{\cdot}s$]	$\mu_{e,avg}$ [$cm^2/V{\cdot}s$]	V_{th} [V]
PMMA (~500 nm)[b]	80	0.48	0.22	-48– -59	1.18– 4.67 $\times10^6$	0.013	0.0098	56– 65
	150	0.86	0.43	-51– -58	2.15– 2.20 $\times10^5$	0.019	0.015	59– 63
	200	2.5	1.6	-59– -67	1.34– 1.84 $\times10^5$	0.030	0.019	55– 71
	250	2.4	1.6	-64– -69	1.24– 2.57 $\times10^5$	0.055	0.042	54– 69
	310	5.8	4.9	-74– -79	0.81– 5.83 $\times10^5$	0.092	0.057	62– 75
P(VDF-TrFE) (~600 nm)[b]	310	14.4	12.0	-45– -48	3.2–4.1 $\times10^3$	N. A.		

[a]The TFT performance of more than 20 devices was tested in nitrogen atmosphere; [b]The capacitance values per unit area of PMMA and P(VDF-TrFE) were calculated as 6.2 and 15.5 nF/cm^2, respectively.

As the annealing temperature (ranging from 80 to 310 °C) was increased, gradually enhanced charge-carrier mobilities were observed at both hole and electron, resulting in the hole and electron mobilities (μ_h and μ_e) of up to 5.8 and 0.092 $cm^2/V{\cdot}s$, respectively, from the 310 °C annealed film. Over 20 devices from four different substrates were measured, and the average μ_h and μ_e extracted from the saturation regime were 4.9 and 0.057 $cm^2/V{\cdot}s$, respectively, for these devices. To our knowledge, this is the highest value among TIIG-based polymers reported to date. Additionally, we observed a relatively reduced contact resistances (R_cW) for the hole injection upon the PTIIG-Np films annealed at 150–310 °C (<6×10^{-5} $\Omega{\cdot}cm$) compared to the case of 80 °C (1–5×10^{-6} $\Omega{\cdot}cm$) (Table 3.2), which implies better intimate physical contact and molecular chain orientation between the semiconductors and the S-D electrodes by the thermal annealing process.

An intriguing question that arises here is whether the TIIG building block within the polymer framework is critical for the excellent TFT performance. To address this open question, we fabricated

the TG-BC TFTs using the corresponding IIG-based polymer (PIIG-Np) as a semiconductor (see synthesis and structure in Scheme 3.2). The devices based on this polymer exhibited about 100 times lower hole mobilities (μ_h = ~10^{-2} $cm^2/V \cdot s$) (Figure 3.3 and Table 3.3) than those of PTIIG-Np, which is associated with the large differences between two semiconductors in the respect of energy levels and conjugated backbone planarity (Figure 3.4 and Table 3.4). Therefore, the origin of the overall improved PTIIG-Np transistor performance could be ascribed to the structural and electronic features originating from the suitable molecular set-up.

Scheme 3.2. Synthetic routes of PIIG-Np.[a]

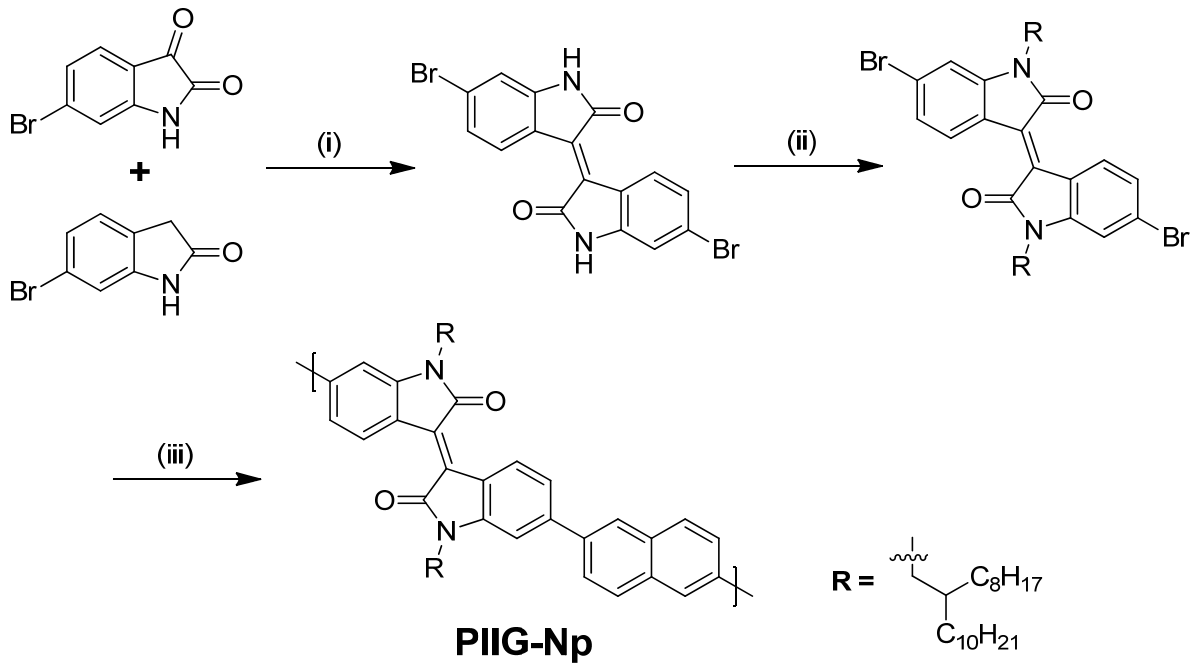

[a]Reagents and conditions: (i) HCl, AcOH, reflux, overnight, 95%; (ii) 2-octyldodecyliodide, K_2CO_3, DMF, reflux, overnight, 80%; (iii) Suzuki polymerization, 2,6-*bis*(4,4,5,5-tetramethyl-1,3,2-dioxaborolan-2-yl)naphthalene, toluene, H_2O, K_3PO_4, P(*o*-tolyl)$_3$, $Pd_2(dba)_3$, 90°C, 72h, 65%, M_n = 190.0 kDa, M_w = 448.4 kDa, PDI = 2.36. (PS/THF standard)

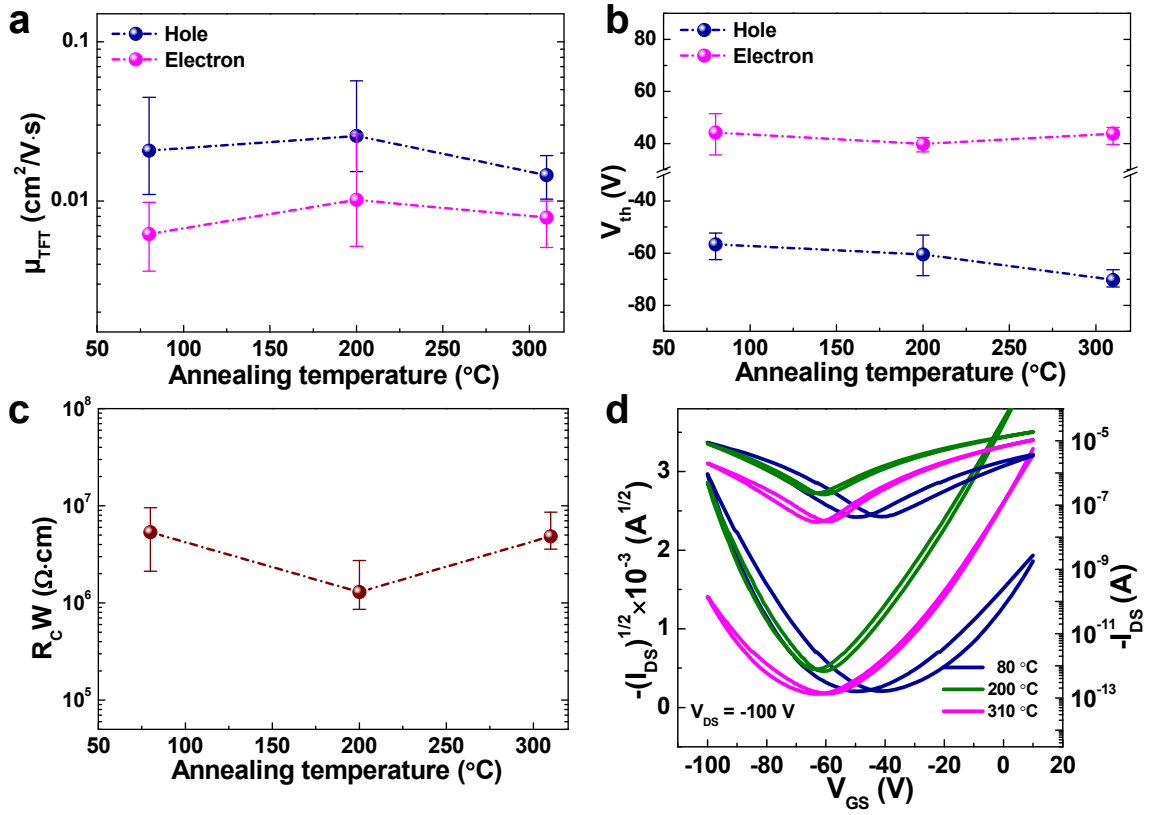

Figure 3.3. Electrical characteristics of solution-processed PIIG-Np TFTs with PMMA dielectric. a, hole and electron mobility distributions based on various annealing temperatures. b, Threshold voltage (V_{th}) distributions. c, Channel width normalized *p*-channel contact resistance (R_cW) values, which was derived from a Y-function method, depending on the thermal-annealing temperatures of PIIG-Np. d, The transfer characteristics for PIIG-Np devices at -100 V of V_{DS} (channel length (L): 20 μm, width (W): 1 mm).

Table 3.3. Summary of TFT performance characteristics of PIIG-Np

Condition[a]		*p*-channel[b]				*n*-channel[b]		
Insulator	T [°C]	$\mu_{h,max}$ [cm^2/V·s]	$\mu_{h,avg}$ [cm^2/V·s]	V_{th} [V]	R_c·W [Ω·cm]	$\mu_{e,max}$ [cm^2/V·s]	$\mu_{e,avg}$ [cm^2/V·s]	V_{th} [V]
PMMA (~500 nm)	80	4.47×10^{-2}	2.07×10^{-2}	-52– -63	2.1– 9.6×10^{6}	9.80×10^{-3}	6.19×10^{-3}	36– 52
	200	5.70×10^{-2}	2.56×10^{-2}	-53– -69	0.86– 2.7×10^{6}	2.64×10^{-2}	1.02×10^{-2}	37– 42
	310	1.93×10^{-2}	1.45×10^{-2}	-66– -73	3.6– 8.6×10^{6}	1.00×10^{-2}	7.87×10^{-3}	40– 46

[a]The TFT performance of more than 20 devices was tested in nitrogen atmosphere; [b]The all electrical parameters were measured at the saturation region (±100 V of V_{DS}) and extracted in the ranges from ±80 to ±100 V of V_{GS}.

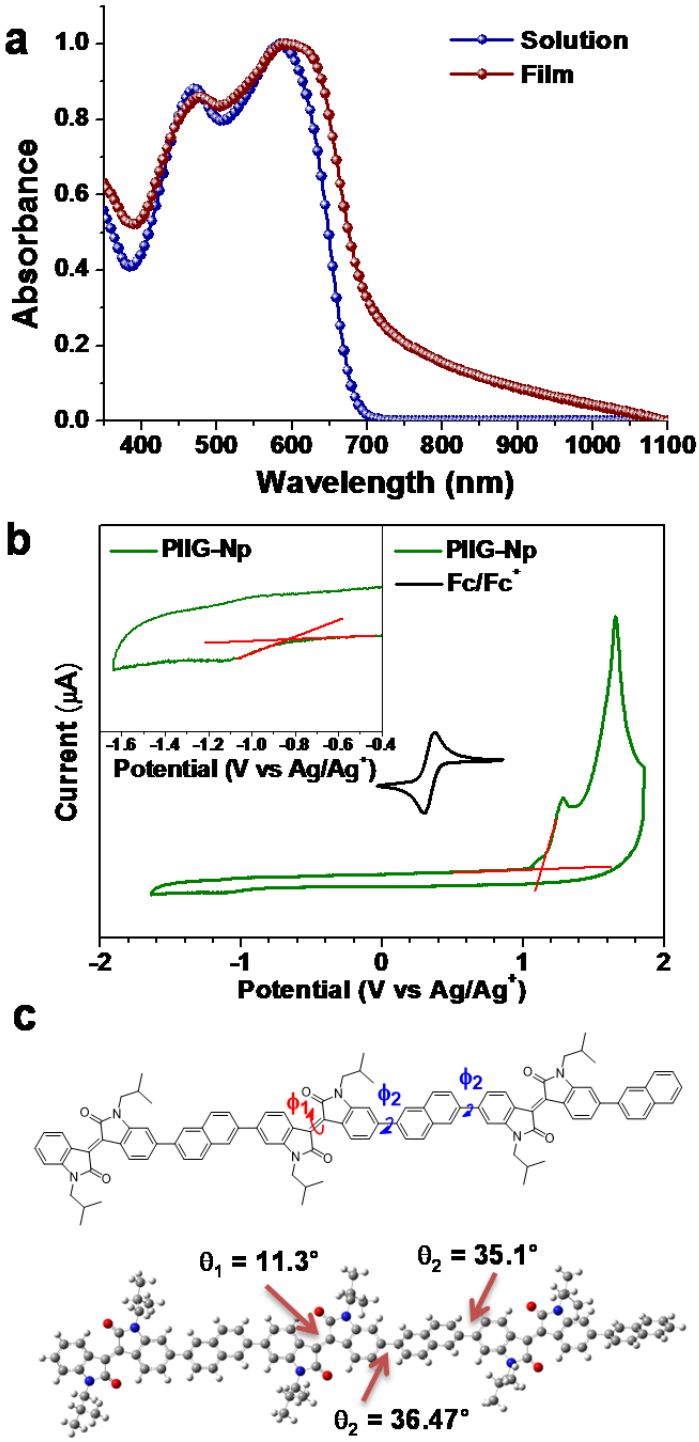

Figure 3.4. Optical and electrochemical properties and DFT calculated structure at the B3LYP/6-31G** level. a, Normalized ultraviolet–visible absorption spectra of PIIG-Np in $CHCl_3$ solution and as a thin film on quartz substrate. b, HOMO and LUMO levels determined by the thin film using cyclic voltammetry (CV) that calibrated by the Fc/Fc^+ redox couple as an external standard. c, Calculated dihedral angles of the trimer structure.

Table 3.4. Optophysical properties of PIIG-Np

	M_n (kDa)	PDI	λ_{max}^{sol} (nm)[a]	λ_{max}^{film} (nm)	E_g^{opt} (eV)[b]	E_{HOMO} (eV)[c]	E_{LUMO} (eV)[c]	E_g^{CV} (eV)[d]
PIIG-Np	190.0	2.36	585	699	1.77	-5.56	-3.59	1.97

[a]Chloroform solution; [b]Determined from the onset of the electronic absorption spectra; [c]Cyclic voltammetry determined with Fc/Fc^+ (E_{HOMO} = -4.80 eV) as the external reference; [d]$E_g^{CV} = E_{LUMO} - E_{HOMO}$.

It is true that the nature of the microscopic motion of charge carriers has been correlated to the chemical purity and structural quality of the organic semiconductors. The fact that the dielectric properties of the gate insulator also have a strong influence on the charge mobility has been discovered recently.[13,32,33] Although the extraordinary mobilities were achieved as described above, here we still decided to construct the TFT devices (W = 1 mm, L = 50 μm) of PTIIG-Np based on the optimized annealing temperature (310 °C) by replacing PMMA layer with P(VDF-TrFE). P(VDF-TrFE), a well-known a high-dielectric-constant ('high-*k*', k = 10–12) ferroelectric polymer, resulting in lower operating voltages of TFTs,[34,35] which is especially desirable for portable and wearable electronics.[3,36,37] Moreover, our group recently demonstrated a significant enhancement of hole transport and injection for *n*-channel dominant naphthalene-bis(dicarboximide)-dithiophene polymer (P(NDI2OD-T2)) using P(VDF-TrFE) in which well-balanced ambipolarity being mobile for both holes and electrons (~0.1 $cm^2/V \cdot s$) was realized[38]. The TG-BC PTIIG-Np devices were fabricated similarly to the former case, except that high-*k* P(VDF-TrFE) was used as the gate dielectric layer after spin-coating the semiconductor solution and then applied the optimized annealing temperature of 310 °C for semiconductor ordering (see Figure 3.2d and Figure 3.2e). Consequently, after spin-coating of P(VDF-TrFE) solution, the films were baked at 80 °C to remove the residual solvent and the completed devices were re-heated at 160 °C above the melting temperature (T_m: ~148 °C) in order to get rid of its crystalline β-phase formation,[39] of which state would induce the large ferroelectric properties in P(VDF-TrFE); The β-phase peak of a P(VDF-TrFE) film at ca. 20° in the diffraction angle was fully diminished by the melt-annealing process (at 160 °C) (see Figure 3.5). As contrasted to the PMMA dielectric case with PTIIG-Np TFTs, the devices based on P(VDF-TrFE) rendered unipolar *p*-type operations, with unprecedented high mobility of up to 14.4 $cm^2/V \cdot s$ (12 $cm^2/V \cdot s$ on average), which could be promising for real-life TFTs. In our previous report, the origin of the remarkable boost in the hole carrier mobility was explained by the molecular orbital energy modulation through dipoles of P(VDF-TrFE) and organic semiconductor, which pull-up HOMO and LUMO levels.[38] Thus, the large dipole polarization at the interface of the fluorinated polymer can promote the accumulation of positive charge carriers at the semiconductor-dielectric interlayer by the band bending.

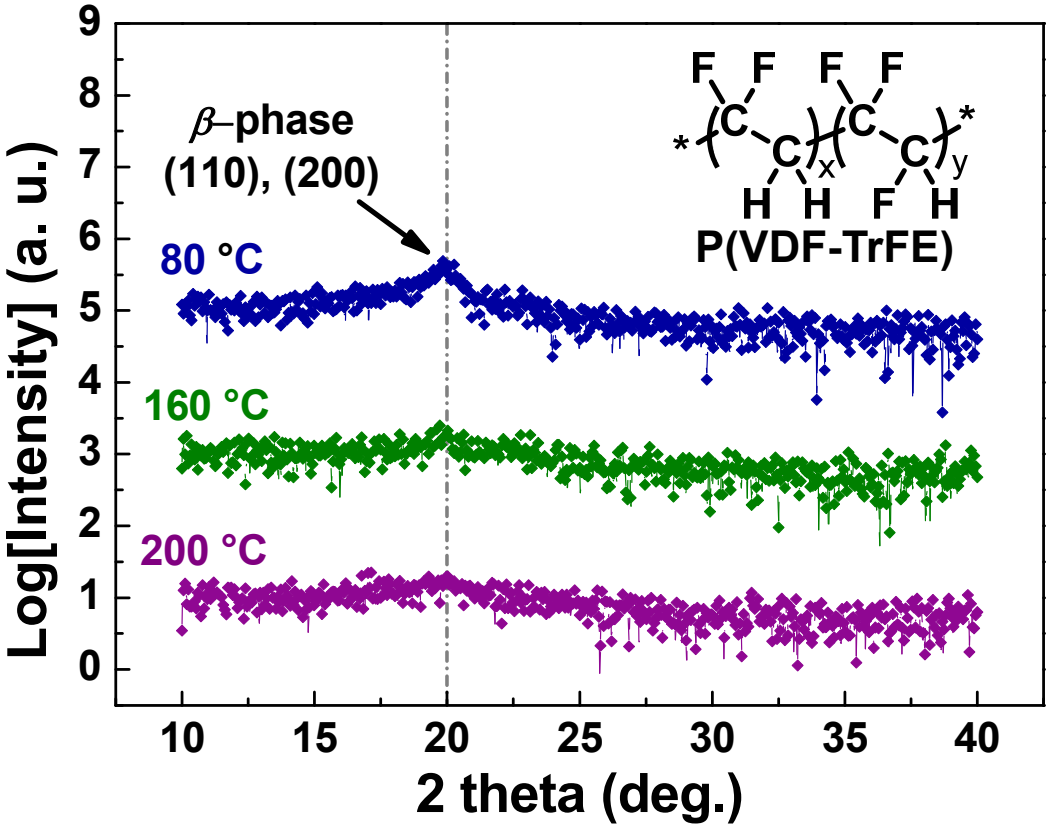

Figure 3.5. XRD patterns of P(VDF-TrFE) layer depending on annealing temperatures (80, 160, and 200 °C). The upper inset indicates the chemical structure of P(VDF-TrFE).

Thin Film Microstructure Analyses: To gain a picture of the correlation between molecular packing/crystallinity and the unprecedented TFTs performance, we investigated the microstructure (crystalline nature and molecular orientation) of PTIIG-Np, based on grazing incidence X-ray diffraction (GIXD) and atomic force microscopy (AFM) measurements. Figure 3.6a shows the GIXD diffractograms (both in- and out-of-plane diffraction profiles) of the PTIIG-Np films annealed at 310 ^{o}C prepared by spin-casting onto SiO_2/Si substrate. The detailed crystallographic parameters extracted from those GIXD patterns are also listed in Table 3.5.

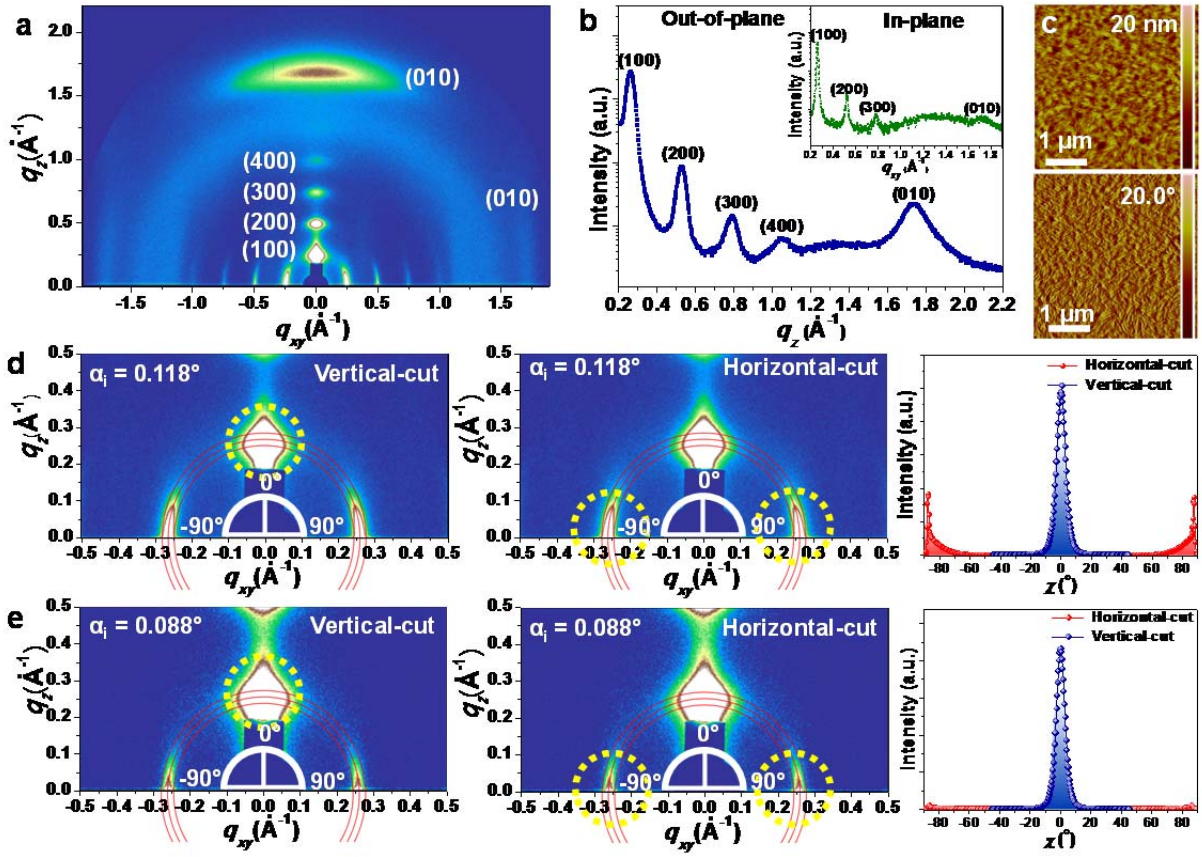

Figure 3.6. Microstructure analysis of PTIIG-Np. GIXD profiles and AFM images of solution-processed PTIIG-Np films annealed at 310 °C. a,b, GIXD image (a) and pattern (out-of plane) (b) of thin films (Inset is the corresponding in-plane GIXD pattern). c, AFM height (top) and phase (bottom) images. d,e, The local GIXD diffraction data ranged from -0.5 to 0.5 Å^{-1} in q_{xy} and from 0 to 0.5 Å^{-1} in q_z and the corresponding intensity-corrected pole figures of the (100) reflection. Data in d are the diffractions in which the incidence angle of X-ray was set to be 0.118°, just above the critical angle of the film but below the critical angel of the substrate, to penetrate whole film thickness. Data in e are the diffractions in which the incidence angle of X-ray was set to be 0.088°, below the critical angle of the film, to explore the majority populations on the near-surface region of the film. The columns on the left and the middle qualitatively represent the circular averaged areas along $q_{xy} \approx 0$ Å^{-1} (fraction of edge-on crystallites) and $q_z \approx 0$ Å^{-1} (fraction of face-on crystallites), respectively. The columns on the right show the complete pole figures, compiled by the integral intensities from each area (where χ is defined as the angle between the crystallite orientation and the surface normal).

The GIXD reveals that every PTIIG-Np film has well-ordered layer-by-layer lamellar packing microstructure, adopting bi-modal distribution of edge-on and face-on crystallites, where the molecular packing out-of-plane appears nominally along the q_z axis and the in-plane ordering along q_{xy}. Along the out-of-plane direction, almost all polymer films exhibit the diffraction peaks up to the fourth order of the lamellar stacking repeat (i.e., (100), (200), (300), and (400); d_{100} = 23.8–25.8 Å) with additional multiple-diffracted intensities also observed in in-plane direction. In addition, the

short π-π stacking spacings of ~3.6 Å (q = ~1.7 Å^{-1}) in both q_z and q_{xy} profiles are obtained from all case films (assigned as (010) peak here), being convincing evidence of 3-D conduction channel-induced structures. As the thermal annealing was increased up to 250 °C, no significant changes in the diffraction patterns were observed, while in both the q_z and q_{xy}, there is not only a slight shift in the (100) peak position to higher values (~sub-Å range), but also its estimated coherence length (L_c) based on Scherrer's equation[40] is gradually increased. Especially, after annealing the films to 310 °C, the diffraction peaks become more-intense and sharper, leading to remarkably large (100) L_c values of 140 Å (q_z axis) and 383 Å (q_{xy} axis) (compared to those annealed at different temperatures), which indicates further improved microstructural ordering and enhanced crystalline structure.[41,42] Therefore, these GIXD data support the observed highest performance for PTIIG-Np film annealed at 310 °C.

Table 3.5. Crystallographic parameters calculated from GIXD profiles of PTIIG-Np

Crystallographic parameters		Preparation condition				
		80 °C annealed	150 °C annealed	200 °C annealed	250 °C annealed	310 °C annealed
Lamellar stack (h00)	q_z (Å^{-1})	0.2613	0.2547	0.2614	0.2517	0.2636
	d-spacing (Å)	24.0	24.7	24.0	25.8	23.8
	FWHM (Å^{-1})	0.0685	0.0611	0.0603	0.0597	0.0403
	Coherence length (Å)	82.6	92.6	93.8	94.7	140.4
π-π stack (0k0)	q_z (Å^{-1})	1.7494	1.7450	1.7490	1.7610	1.7390
	d-spacing (Å)	3.59	3.60	3.59	3.57	3.61
Lamellar stack (h00)	q_{xy} (Å^{-1})	0.2668	0.2651	0.2637	0.2616	0.2616
	d-spacing (Å)	23.6	23.7	23.8	24.0	24.0
	FWHM (Å^{-1})	0.0378	0.0332	0.0260	0.0225	0.0148
	Coherence length (Å)	149.6	170.4	217.6	251.4	382.9
π-π stack (0k0)	q_{xy} (Å^{-1})	1.7723	1.7602	1.7423	1.7298	1.7292
	d-spacing (Å)	3.55	3.57	3.61	3.63	3.63

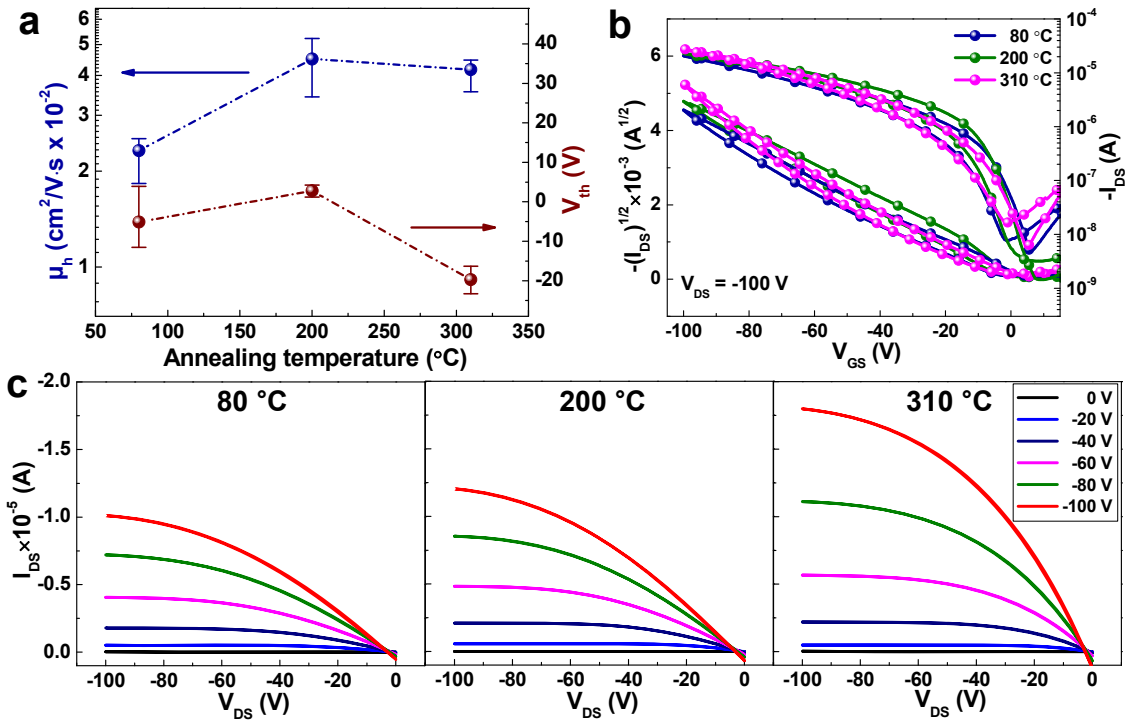

Figure 3.7. Electrical characteristics of solution-processed PTIIG-Np TFTs with bottom-gate and top-contact configuration (BG-TC). a, hole mobility and threshold voltage (V_{th}) distribution based on various annealing temperature. b, The representative transfer characteristics for PTIIG-Np TFTs at -100 V of V_{DS} (channel length (L): 50 μm, width (W): 1 mm). c, Output characteristics of PTIIG-Np films depending on the thermal-annealing temperatures (80, 200, and 310 °C).

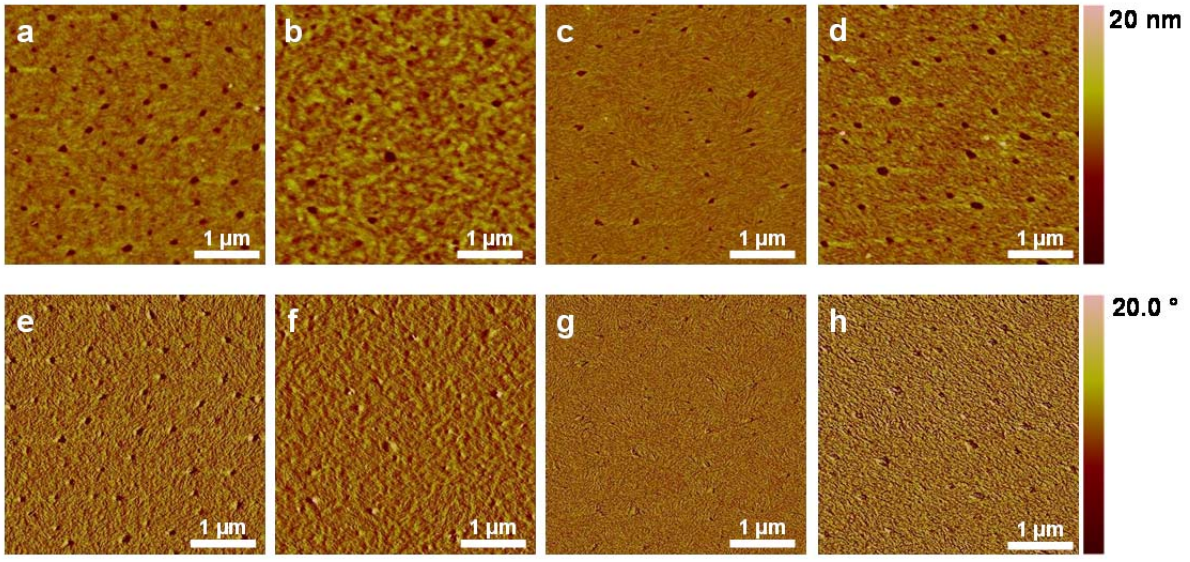

Figure 3.8. AFM (a–d) height and (e–h) phase images from PTIIG-Np thin films annealed at different temperatures. The thin films were annealed at (a and e) 80 °C, (b and f) 150 °C, (c and g) 200 °C and (d and h) 250 °C, respectively.

Table 3.6. Summary of TFT performance characteristics of PTIIG-Np in bottom-gate and top-contact (BG-TC) geometry

Condition[a]		*p*-channel[b]			*n*-channel		
Insulator	T [°C]	$\mu_{h,max}$ [$cm^2/V{\cdot}s$]	$\mu_{h,avg}$ [$cm^2/V{\cdot}s$]	V_{th} [V]	$\mu_{e,max}$ [$cm^2/V{\cdot}s$]	$\mu_{e,avg}$ [$cm^2/V{\cdot}s$]	V_{th} [V]
SiO_2[c] (300 nm)	80	2.53×10^{-2}	2.32×10^{-2}	-12–4	N. A.		
	200	5.23×10^{-2}	4.50×10^{-2}	1–4			
	310	4.47×10^{-2}	4.17×10^{-2}	-23–-16			

[a]The TFT performances of more than 20 devices were tested in nitrogen atmosphere; [b]The all electrical parameters were measured at -100 V of V_{DS} and extracted in the ranges from -80 to -100 V of V_{GS} except for the case of 200 °C annealing temperature, which was derived below -10 V of V_{GS} due to their different maximum charge-carrier mobility distributions; [c]The surfaces were treated with octadecyltrichlorosilane (OTS) monolayers before spin-coating of semiconductor layers to reduce the influences of hydroxyl groups of silicon wafers. The capacitance value per unit area of 300 nm SiO_2 layer is 10 nF/cm^2.

Moreover, to quantify the difference between the edge-on and face-on populations in the film annealed to 310 °C, we constructed a pole figure for the (100) reflection, and extracted the integrated intensity as a function of χ along the arcs, where χ (-90° to 90°) is defined as the semicircular angle between the crystallite orientation and the surface normal.[43] The diffraction data and intensity-corrected pole figure are plotted in Figure 3.6d. The peaks in intensity near $\chi = 0°$ (vertical-cut) and near $\chi = \pm90°$ (horizontal-cut) are associated with the edge-on and face-on crystallites, respectively. The area ratio of the two peaks ($\chi = 0°$–$45°$ and $\chi = 45°$–$90°$) is ≈ 7:3 (71.2% vs. 28.8%), implying a majority edge-on crystallite population in the entire film thickness since the incidence angle (α_i = 0.118°) used is just above the critical angle, ensuring that we sampled the full film depth. On the other hand, when the incidence angle (α_i = 0.088°) is set lower than the sample's critical angle, for accessing majority populations on the near-surface region of the film, the bi-modal distribution is changed to almost uni-modal distribution of the edge-on structure (97.6%) with the trace amount of the face-on structure (see Figure 3.6e). These findings signify that the region near the top surface of the polymer film has a stronger preference for the edge-on orientation compared to that of close to the substrate regions. Therefore, TG-BC TFT architecture used here is thought to be an ideal fit for achieving high mobility of PTIIG-Np, because, in general, the edge-on structure is considered favorable for charge transport.[44,45] The very lower mobilities (μ_h = ~10^{-2} $cm^2/V{\cdot}s$) in the PTIIG-Np-

based bottom-gate and top-contact (BG-TC) devices clearly confirmed the dependence of the device geometry (Figure 3.7 and Table 3.6).

As shown in Figure 3.6c, the AFM images illustrate that the film annealed at 310 ^{o}C consists of uniform polymer fibers that establish highly aligned nanofibrillar networks (see Figure 3.8 for the AFM images at different temperatures). The densely ordered structures are likely due to closer π-π stacking of polymer chains, similarly to other high-performance TFTs materials.[16,17,46-48] We believed that the tightened conformation could also play a critical role in the charge transport efficacy *via* hopping mechanism.

3.3 Conclusions

In order to meet the need for real-life TFTs based on polymer semiconductors as the linchpin of next-generation electronic devices, we present an easily synthesized D–A semiconducting polymer based on alternating the recently formulated thienoisoindigo (TIIG) and simple naphthalene (Np) units, PTIIG-Np, and investigate to determine application in TFTs. PTIIG-Np offers favorable property of charge-carrier mobility (up to 5.8 $cm^2/V{\cdot}s$) thanks to its inherently large co-planarity, favorable energetic levels for hole injection, as well as ideal film morphology that improves semicrystalline lamellar ordering and π-π stacking to achieve a high hopping rate between the polymer chains. More surprisingly, an ultra-high mobility of 14.4 $cm^2/V{\cdot}s$ is demonstrated for the TFT devices using PTIIG-Np with a high-*k* P(VDF-TrFE). This finding is sharply distinguished from most *p*-type organic semiconductors, which exhibit lower mobilities for higher gate dielectric constant. This charge-transport efficacy far beyond the current levels essentially comes courtesy of a winning combination of the rational design of the polymer backbone, the optimal selection of the device configuration, and the benign dielectric-molecule dynamics. Not only does this value by far exceeds those of both amorphous silicon semiconductors and solution-processed small molecular counterparts, but it is also competitive with the performance of TFTs based on organic single crystals and transparent metal oxides. Therefore, this result shows the power of important progress for solution-processed polymer TFTs, and spurs technological translation of practical plastic electronics from laboratory to marketplace.

3.4 Experimental Section

General procedures and methods: All chemicals were purchased either from Aldrich or Acros and used without further purification. The intermediates (1~3), (*E*)-2,2'-dibromo-4,4'-bis(2-octyldodecyl)-[6,6'-bithieno[3,2-*b*]pyrrolylidene]-5,5'(4*H*,4′*H*)-dione (monomer), and 2,6-bis(4,4,5,5-tetramethyl-1,3,2-dioxaborolan-2-yl)naphthalene (co-monomer) were synthesized according to the literature.[24, 29,

[49] ^{1}H NMR spectra were recorded on a Varian VNRS 400 MHz (Varian USA) spectrophotometer using $CDCl_3$ as solvent and tetramethylsilane (TMS) as the internal standard. UV-Vis NIR spectra were taken on UV-1800 (SHIMADZU) spectrometer. Number-average (M_n) and weight average (M_w) molecular weights, and polydispersity index (PDI) of the PTIIG-Np was determined by gel permeation chromatography (GPC) with Perkin-Elmer Series 200 using a series of mono disperse polystyrene as standards in THF (HPLC grade) at 313 K. Cyclic voltammetry (CV) measurement was performed on AMETEK VersaSTAT3 with a three-electrode cell in a nitrogen bubbled 0.1 M tetra-*n*-butylammonium hexafluorophosphate (*n*-Bu_4NPF_6) solution in acetonitrile at a scan rate of 100 mV/s at room temperature. Ag/Ag^+ (0.1 M of $AgNO_3$ in acetonitrile) electrode, platinum wire and polymer coated glassy carbon electrode were used as the reference electrode, counter electrode and working electrode, respectively. The Ag/Ag^+ reference electrode was calibrated using a ferrocene/ferrocenium redox couple as an external standard, whose oxidation potential is set at -4.8 eV with respect to zero vacuum level. The HOMO energy level was obtained from the equation HOMO (eV) = – ($E_{(ox)}^{onset}$ – $E_{(ferrocene)}^{onset}$ + 4.8). The LUMO level of PTIIG-Np was obtained from the equation LUMO (eV) = – ($E_{(red)}^{onset} - E_{(ferrocene)}^{onset}$ + 4.8). Ultraviolet photoelectron spectroscopy (UPS) was examined by AXIS-NOVA CJ109, Kratos. The polymer solution was prepared in chlorobenzene with 5 mg mL^{-1} for PTIIG-Np and the PTIIG-Np solution was spin-coated on ITO glass. Film fabrication was done in a N_2-atmosphere glovebox. The UPS analysis chamber was equipped with a hemispherical electron-energy analyzer (Kratos Ultra Spectrometer), and was maintained at 1.0×10^{-9} Torr. The UPS measurements were carried out using the He I ($h\nu$ = 21.2 eV) source.

Computational details: The geometries of trimer of TIIG-Np was optimized at the density functional theory (DFT) level using the Becke's three-parameter B3LYP exchange-correlation functional and the standard 6-31G** basis set. To reduce the computational costs, we replaced the alkyl chains by isobutyl groups in all cases. DFT calculation was carried out with the Gaussian 09 program package.

Synthesis of PTIIG-Np: In a Schlenk flask, (*E*)-2,2'-dibromo-4,4'-bis(2-octyldodecyl)-[6,6'-bithieno[3,2-*b*]pyrrolylidene]-5,5'(4*H*,4'*H*)-dione (99 mg, 0.1 mmol) and 2,6-bis(4,4,5,5-tetramethyl-1,3,2-dioxaborolan-2-yl)naphthalene (38 mg, 0.1 mmol) were dissolved in anhydrous toluene (5 mL); to this, a solution of K_3PO_4 (106 mg, 0.5 mmol), tri-*o*-tolylphosphine (4.4 mg, 14.4 μmol) and deionized water (1.5 ml) was added. The mixture was vigorously stirred at room temperature under argon. After 30 min, $Pd_2(dba)_3$ (2.7 mg, 3.0 μmol) was added to the reaction mixture and stirred at 90 ^oC for 3 d. The crude product was poured into a mixture of methanol and ammonia (4:1 v/v, 250 mL). The resulting solid was filtered off and subjected to sequential Soxhlet extraction with methanol (1 d), acetone (1 d), and hexane (1 d) to remove the low molecular weight fractions of the materials. The

residue was extracted with chloroform in order to produce a dark-green product after precipitating again from methanol and drying *in vacuo*. Isolated yield = 57 mg (59%). M_n = 21.0 kDa, M_w = 102.2 kDa, PDI = 4.87. ^{1}H NMR (400 MHz, $CDCl_3$, 348 K): δ (ppm) 8.33-6.96 (br, 8H), 3.76-3.69 (br, 4H) 2.02-2.00 (br, 2H), 1.25-1.23 (br, 64H), 0.84 (br, 12H). Elemental Analysis: Anal. Calcd: C, 77.55; H, 9.52; N, 2.92; O, 3.33; S, 6.68 Found: C, 77.45; H, 9.49; N, 2.82; O, 3.41; S, 6.67

AFM characterization: Agilent 5500 scanning probe microscope (SPM) running with a Nanoscope V controller was used to obtain AFM images of polymer thin films. AFM images were recorded in high-resolution tapping mode under ambient conditions. Premium silicon cantilevers (TESP) were used with a rotated tip to provide more symmetric representation of features over 200 nm.

GIXD characterization: Grazing incidence X-ray diffraction (GIXD) measurements were conducted at PLS-II 9A U-SAXS beamline of the Pohang Accelerator Laboratory in Korea. The X-rays coming from the in-vacuum undulator (IVU) are monochromated (wavelength λ = 1.10994 Å) using a double crystal monochromator and focused both horizontally and vertically (450 (H)×60 (V) μm^2 in FWHM @ sample position) using K-B type mirrors. The GIXD sample stage is equipped with a 7-axis motorized stage for the fine alignment of sample, and the incidence angle of X-ray beam was set to be either 0.118º or 0.088º for PTIIG-Np. GIXD patterns were recorded with a 2D CCD detector (Rayonix SX165) and X-ray irradiation time was 6–7 s, dependent on the saturation level of the detector. Diffraction angles were calibrated with a pre-calibrated sucrose (Monoclinic, P21, a = 10.8631 Å, b = 8.7044 Å, c = 7.7624 Å, β = 102.938°),[50] and the sample-to-detector distance was ~231 mm.

TFT fabrication and testing: TG-BC devices were fabricated and tested with PTIIG-Np in nitrogen atmosphere. Thin films of PTIIG-Np were spin-cast from 1,2,4-trichlorobenzene solutions (~5 mg mL^{-1}) on glass substrates with lithographically patterned Ni/Au source-drain electrodes (3 nm/12 nm), and subsequently dried at room temperature for 2 h before a thermal annealing at various temperatures (ranging from 80 to 310 °C) for 30 min and then allowed to cool down slowly. PMMA (Sigma-Aldrich, M_n: 120 kDa) was spin-coated at 2000 rpm from a 80 mg ml^{-1} solution in *n*-butyl acetate on top of the PTIIG-Np layer to form a dielectric layer (~500 nm thick), and subsequently baked at 80 °C for 30 min. In the case of P(VDF-TrFE) insulator layer, P(VDF-TrFE) (Solvay, 70:30 mol% random copolymer) was dissolved in methyl ethyl ketone (MEK) at a concentration of 70 mg ml^{-1}. Thereafter, the solution was spin-coated on the active layer at 4000 rpm (~600 nm thick), and followed by baking at 80 °C for 10 min. The devices were thermally re-annealed at 160 °C above the melting temperature of P(VDF-TrFE) (T_m: ~148 °C) for 30 min and subsequently slowly cooled to room temperature to restrict its ferroelectric properties.

Finally, Al gate electrodes were thermally evaporated on top of PMMA or P(VDF-TrFE) layers as gate electrodes to complete top-gate transistors. The devices were characterized through a Keithley 4200 parameter analyzer on a probe station in nitrogen atmosphere. The charge-carrier mobility was calculated from the data measured in the saturated regime of transistor operation according to the following equation:

$$I_{DS} = \frac{\mu C_{diel} W}{2L}(V_{GS} - V_{th})^2 \quad (1)$$

Where W and L are the channel width and length, C_{diel} is the gate dielectric layer capacitance value per unit area, and V_{GS} and V_{th} are the gate voltage and threshold voltage, respectively.

3.5 Reference

1. Beaujuge, P. M.; Fréchet, J. M. *J. Am. Chem. Soc.* **2011**, *133*, 20009.
2. Gelinck, G.; Heremans, P.; Nomoto, K.; Anthopoulos, T. D. *Adv. Mater.* **2010**, *22*, 3778.
3. Arias, A. C.; MacKenzie, J. D.; McCulloch, I.; Rivnay, J.; Salleo, A. *Chem. Rev.* **2010**, *110*, 3.
4. Yan, H.; Chen, Z.; Zheng, Y.; Newman, C.; Quinn, J. R.; Dötz, F.; Kastler, M.; Facchetti, A. *Nature* **2009**, *457*, 679.
5. Sirringhaus, H.; Brown, P.; Friend, R.; Nielsen, M. M.; Bechgaard, K.; Langeveld-Voss, B.; Spiering, A.; Janssen, R. A.; Meijer, E.; Herwig, P. *Nature* **1999**, *401*, 685.
6. Tsao, H. N.; Cho, D. M.; Park, I.; Hansen, M. R.; Mavrinskiy, A.; Yoon, D. Y.; Graf, R.; Pisula, W.; Spiess, H. W.; Müllen, K. *J. Am. Chem. Soc.* **2011**, *133*, 2605.
7. McCulloch, I.; Heeney, M.; Bailey, C.; Genevicius, K.; MacDonald, I.; Shkunov, M.; Sparrowe, D.; Tierney, S.; Wagner, R.; Zhang, W. *Nature Mater.* **2006**, *5*, 328.
8. Pan, H.; Li, Y.; Wu, Y.; Liu, P.; Ong, B. S.; Zhu, S.; Xu, G. *J. Am. Chem. Soc.* **2007**, *129*, 4112.
9. Dhoot, A. S.; Yuen, J. D.; Heeney, M.; McCulloch, I.; Moses, D.; Heeger, A. J. *Proc. Natl Acad. Sci. USA* **2006**, *103*, 11834.
10. Briseno, A. L.; Mannsfeld, S. C.; Ling, M. M.; Liu, S.; Tseng, R. J.; Reese, C.; Roberts, M. E.; Yang, Y.; Wudl, F.; Bao, Z. *Nature* **2006**, *444*, 913.
11. Muccini, M. *Nature Mater.* **2006**, *5*, 605.
12. Dimitrakopoulos, C.; Purushothaman, S.; Kymissis, J.; Callegari, A.; Shaw, J. *Science* **1999**, *283*, 822.

13. Hulea, I.; Fratini, S.; Xie, H.; Mulder, C.; Iossad, N.; Rastelli, G.; Ciuchi, S.; Morpurgo, A. *Nature Mater.* **2006**, *5*, 982.

14. Brown, A.; Pomp, A.; Hart, C.; De Leeuw, D. *Science* **1995**, *270*, 972.

15. Crone, B.; Dodabalapur, A.; Lin, Y.-Y.; Filas, R.; Bao, Z.; LaDuca, A.; Sarpeshkar, R.; Katz, H.; Li, W. *Nature* **2000**, *403*, 521.

16. Lee, J.; Han, A.-R.; Yu, H.; Shin, T. J.; Yang, C.; Oh, J. H. *J. Am. Chem. Soc.* **2013**, *135*, 9540.

17. Lee, J.; Han, A.-R.; Kim, J.; Kim, Y.; Oh, J. H.; Yang, C. *J. Am. Chem. Soc.* **2012**, *134*, 20713.

18. Li, J.; Zhao, Y.; Tan, H. S.; Guo, Y.; Di, C.-A.; Yu, G.; Liu, Y.; Lin, M.; Lim, S. H.; Zhou, Y. *Sci. Rep.* **2012**, *2*, 754.

19. Chen, H.; Guo, Y.; Yu, G.; Zhao, Y.; Zhang, J.; Gao, D.; Liu, H.; Liu, Y. *Adv. Mater.* **2012**, *24*, 4618.

20. Sirringhaus, H. *Adv. Mater.* **2005**, *17*, 2411.

21. Lei, T.; Dou, J. H.; Pei, J. *Adv. Mater.* **2012**, *24*, 6457.

22. Mei, J.; Kim, D. H.; Ayzner, A. L.; Toney, M. F.; Bao, Z. *J. Am. Chem. Soc.* **2011**, *133*, 20130.

23. Lei, T.; Cao, Y.; Fan, Y.; Liu, C.-J.; Yuan, S.-C.; Pei, J. *J. Am. Chem. Soc.* **2011**, *133*, 6099.

24. Ashraf, R. S.; Kronemeijer, A. J.; James, D. I.; Sirringhaus, H.; McCulloch, I. *Chem. Commun.* **2012**, *48*, 3939.

25. Koizumi, Y.; Ide, M.; Saeki, A.; Vijayakumar, C.; Balan, B.; Kawamoto, M.; Seki, S. *Polym. Chem.* **2013**, *4*, 484.

26. Van Pruissen, G. W.; Gholamrezaie, F.; Wienk, M. M.; Janssen, R. A. *J. Mater. Chem.* **2012**, *22*, 20387.

27. Chabinyc, M. L.; Toney, M. F.; Kline, R. J.; McCulloch, I.; Heeney, M. *J. Am. Chem. Soc.* **2007**, *129*, 3226.

28. DeLongchamp, D. M.; Kline, R. J.; Lin, E. K.; Fischer, D. A.; Richter, L. J.; Lucas, L. A.; Heeney, M.; McCulloch, I.; Northrup, J. E. *Adv. Mater.* **2007**, *19*, 833.

29. Dutta, G. K.; Han, A.-R.; Lee, J.; Kim, Y.; Oh, J. H.; Yang, C. *Adv. Funct. Mater.* **2013**, *23*, 5317.

30. Kim, Y.; Hong, J.; Oh, J. H.; Yang, C. *Chem. Mater.* **2013**, *25*, 3251.

31. Hou, J.; Tan, Z. a.; Yan, Y.; He, Y.; Yang, C.; Li, Y. *J. Am. Chem. Soc.* **2006**, *128*, 4911.

32. Xia, Y.; Cho, J. H.; Lee, J.; Ruden, P. P.; Frisbie, C. D. *Adv. Mater.* **2009**, *21*, 2174.

33. Veres, J.; Ogier, S. D.; Leeming, S. W.; Cupertino, D. C.; Mohialdin Khaffaf, S. *Adv. Funct. Mater.* **2003**, *13*, 199.

34. Naber, R. C.; Tanase, C.; Blom, P. W.; Gelinck, G. H.; Marsman, A. W.; Touwslager, F. J.; Setayesh, S.; De Leeuw, D. M. *Nature Mater.* **2005**, *4*, 243.

35. Li, J.; Sun, Z.; Yan, F. *Adv. Mater.* **2012**, *24*, 88.

36. Sekitani, T.; Zschieschang, U.; Klauk, H.; Someya, T. *Nature Mater.* **2010**, *9*, 1015.

37. Gundlach, D. J. *Nature Mater.* **2007**, *6*, 173.

38. Baeg, K. J.; Khim, D.; Jung, S. W.; Kang, M.; You, I. K.; Kim, D. Y.; Facchetti, A.; Noh, Y. Y. *Adv. Mater.* **2012**, *24*, 5433.

39. Mao, D.; Quevedo-Lopez, M.; Stiegler, H.; Gnade, B.; Alshareef, H. *Org. Electron.* **2010**, *11*, 925.

40. Patterson, A. *Phys. Rev.* **1939**, *56*, 978.

41. Rivnay, J.; Noriega, R.; Northrup, J. E.; Kline, R. J.; Toney, M. F.; Salleo, A. *Phys. Rev. B* **2011**, *83*, 121306.

42. Zhang, X.; Bronstein, H.; Kronemeijer, A. J.; Smith, J.; Kim, Y.; Kline, R. J.; Richter, L. J.; Anthopoulos, T. D.; Sirringhaus, H.; Song, K.; Heeney, M.; Zhang, W.; McCulloch, I.; DeLongchamp, D. M. *Nat. Commun.* **2013**, *4*, 2238.

43. Rivnay, J.; Steyrleuthner, R.; Jimison, L. H.; Casadei, A.; Chen, Z.; Toney, M. F.; Facchetti, A.; Neher, D.; Salleo, A. *Macromolecules* **2011**, *44*, 5246.

44. Schuettfort, T.; Thomsen, L.; McNeill, C. R. *J. Am. Chem. Soc.* **2013**, *135*, 1092.

45. Caironi, M.; Bird, M.; Fazzi, D.; Chen, Z.; Di Pietro, R.; Newman, C.; Facchetti, A.; Sirringhaus, H. *Adv. Funct. Mater.* **2011**, *21*, 3371.

46. Usta, H.; Newman, C.; Chen, Z.; Facchetti, A. *Adv. Mater.* **2012**, *24*, 3678.

47. Yuen, J. D.; Fan, J.; Seifter, J.; Lim, B.; Hufschmid, R.; Heeger, A. J.; Wudl, F. *J. Am. Chem. Soc.* **2011**, *133*, 20799.

48. Bronstein, H.; Chen, Z.; Ashraf, R. S.; Zhang, W.; Du, J.; Durrant, J. R.; Shakya Tuladhar, P.; Song, K.; Watkins, S. E.; Geerts, Y. *J. Am. Chem. Soc.* **2011**, *133*, 3272.

49. Omachi, H.; Segawa, Y.; Itami, K. *Org. lett.* **2011**, *13*, 2480.

50. Hynes, R.; Le Page, Y. *J. Appl. Crystallogr.* **1991**, *24*, 352.

Chapter 4 Side-Chain Modification in Isoindigo Polymer for Organic Photovoltaics

Chapter 4 is reproduced in part with permission of "Control of Charge Dynamics via Use of Non-Ionic Phosphonate Chains and Their Effectiveness for Inverted Structure Solar Cells" from Kim G. *et al*. *Adv. Energy Mater.*, **2015**, DOI: 10.1002/aenm.201500844.

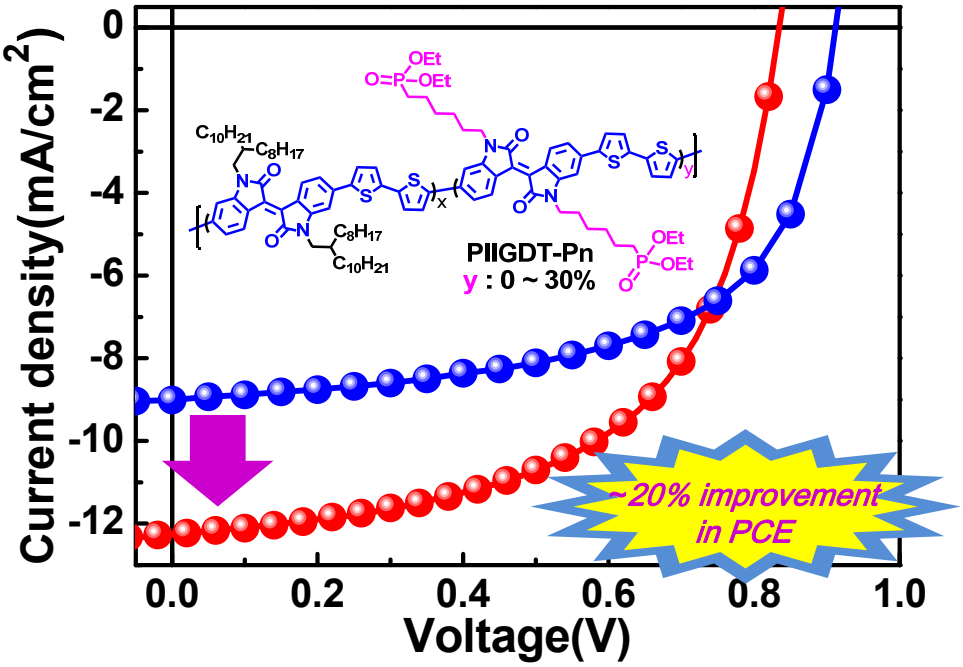

4.1 Introduction

Compared to conventional bulk-heterojunction (BHJ) polymer solar cells (PSCs), inverted PSCs (i-PSCs) demonstrate superior long-term stability by avoiding the need for the corrosive and hygroscopic hole-transporting poly(3,4-ethylenedioxythiophene):poly(styrene-sulfonate) (PEDOT:PSS) and low-work function metal cathodes, both of which are detrimental to device lifetime.[1-6] Furthermore, i-PSCs may offer additional advantages over the conventional configuration by taking advantage of vertical phase separation and donor / acceptor gradients in the photoactive layer,[2, 7] which make inverted device architectures an attractive approach for all types of PSCs. Reversing the polarity of charge-collecting electrodes in i-PSCs can be achieved by utilizing

appropriate electron-transporting and hole-transporting interlayers at the indium tin oxide (ITO)/active layer and active layer/metal interfaces, respectively.

As of today, transition metal oxides (MOs) constitute one of the most promising classes of interlayer materials due to their relatively high mobility, environmental stability, and high transparency. Significant progress has been reported not only for electron-transporting layer MOs, such as Cs_2CO_3, TiOx, and ZnO,[8-10] but also for various hole-transporting MOs, including MoO_3, V_2O_5, NiO, Sb_2O_3, and WO_3,[11-18] which have to be effective in improving power conversion efficiencies (PCEs) in i-PSCs. However, in principle, the polar surfaces of MOs may have poor interfacial contact with hydrophobic organic active layer, inhibiting electron extraction in i-PSCs.

To overcome phase compatibility issues at the hybrid organic/inorganic interfaces in i-PSCs, we have introduced a variable amount of phosphonate-terminated non-ionic side chain substitution into an isoindigo (IIG)-based model polymer. The polymers were designed with the following considerations: (i) The phosphonate groups have good compatibility with MOs due to their polar and hydrophilic character, which is expected to improve interfacial contact via interfacial dipole formation, improving charge transport and collection. (ii) The incorporation of phosphonate side-chains can both increase the dielectric constant of the donor polymer and suppress non-geminate recombination losses in i-PSCs, allowing the possibility of longer carrier lifetimes and improved short-circuit current (J_{SC}).[19] (iii) A further aspect of the non-ionic phosphonates is the possibility to avoid electrical field-induced redistribution of ions/electrode interfaces; a mechanism which leads to instability when conjugated polyelectrolytes with ionized functionalities are used in the same context.[20]

In this work, we have examined the effects that phosphonate side-chain substitution has on the semiconducting properties of IIG-based polymers. Several factors were taken into account in this study, including charge-collection efficacy, recombination dynamics, device performance and film morphology. Interestingly, we discovered that the polymer-packing orientation can be controlled by adjusting the phosphonate substitution to yield films that favor face-on (out-of-plane π-stacking) or edge-on (in-plane π-stacking) packing relative to the substrate. Notably, the 5% phosphonate-incorporated polymer exhibited a ~20% enhancement in PCE in i-PSCs (5.00% to 5.95%) compared to the reference polymer. This improvement was attributed to a combination of improved compatibility at the MO interface, favorable BHJ morphology, efficient charge-transport/collection, and reduced non-geminate recombination in the active layer.

4.2 Result and Discussion

Synthesis and Characterization Synthetic routes to the IIG monomers and target polymers are shown in Scheme 1. First, 2-octyldodecyl and diethyl hexylphosphonate side chains were attached to the 2,6-

dibromoisoindigo (Br_2-IIG), core via base-promoted *N*-alkylation, generating IIG monomers 1 and 2, respectively. Note that 1 was readily soluble in common organic solvents, whereas the introduction of hydrophilic phosphonate side chains led to limited solubility of 2 in non-polar solvents (*i.e*, pentane, hexane, etc.).

To investigate the influence of the phosphonate side chain substitution on i-PSC performance, a series of IIG-based statistical polymers PIIGDT-Pn were synthesized, where n refers molar percentages (0%, 5%, 15%, 30%) of phosphonate functionalized IIG-containing repeating units. The polymers were synthesized by Stille copolymerization of a bis-stannyl dithiophene (DT) co-monomer with different ratios of 1 and 2. Detailed synthetic routes and characterizations can be found in the Experimental Section. The solubility of polymers gradually decreased as the content of phosphonate-containing IIG increased, thus soluble products could not be isolated with high phosphonate substitution (greater than 30% of 2**)**.

Inspection of ^{1}H NMR spectra of the purified PIIGDT-P5, PIIGDT-P15, and PIIGDT-P30 products shows a broad set of resonances at δ = 4.0–4.4 ppm associated with the α hydrogens relative to the phosphonate units (O=$PO_2C_2\underline{H}_4$-) and their intensities correlated well with the feed ratio of the phosphonate-containing IIG units. However, integrating peak areas have previously been used to quantify aliphatic/aromatic proton ratio,[21] but can only be used to qualitatively identify the presence of ethyl phosphonate protons due to overlap with non-modified alkyl protons at the same chemical shift in ^{1}H NMR spectra. (Figure 4.1) Each polymer was purified by precipitation into methanol followed by Soxhlet extraction with methanol, acetone, and hexane to remove low molecular weight products. All polymerizations produced polymers with a high number-averaged molecular weights (M_n) in the ranges of 54−130 kDa.

X-ray photoelectron spectroscopy (XPS) was carried out to confirm the presence of phosphonate groups at upper organic-electrode interface. A narrow scan resolution of 0.1 eV was used to accurately characterize the P 2p (132-135) region of the photoelectron spectrum, as shown in Figure 4.2. The unsubstituted polymer shows no P 2p signal, while all of the phosphonated materials show peaks at ~133 eV, consistent with the element P existing in the phosphonate bonding state, while increasing the content of phosphonate group in the polymer leads to an increase in the P 2p signal which is consistent with the monomer feed ratio.

Scheme 4.1. Synthetic routes of IIGDT-based polymers with varying phosphonate content[a]

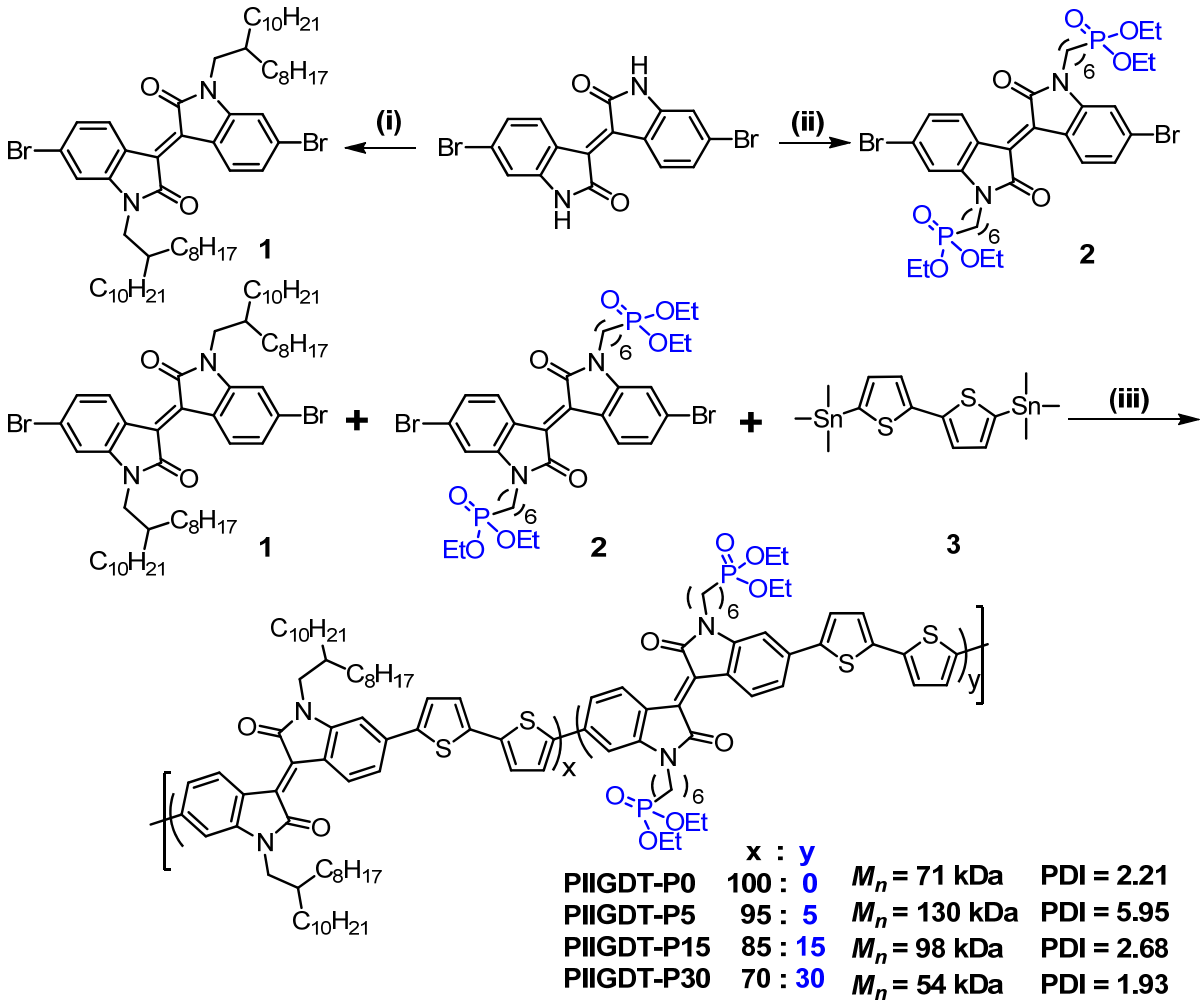

[a]Reagents and conditions: (i) 1-Iodo-2-octyldodecane, K_2CO_3, DMF, reflux, overnight; (ii) Diethyl(6-bromohexyl)phosphonate, K_2CO_3, DMF, reflux, overnight; (iii) DMF, toluene, P(*o*-tolyl)$_3$, $Pd_2(dba)_3$, 90°C, where, the compositions of the two types of repeating units in the polymer products (x:y) were determined by the molar ratio of the monomeric materials **1** and **2**.

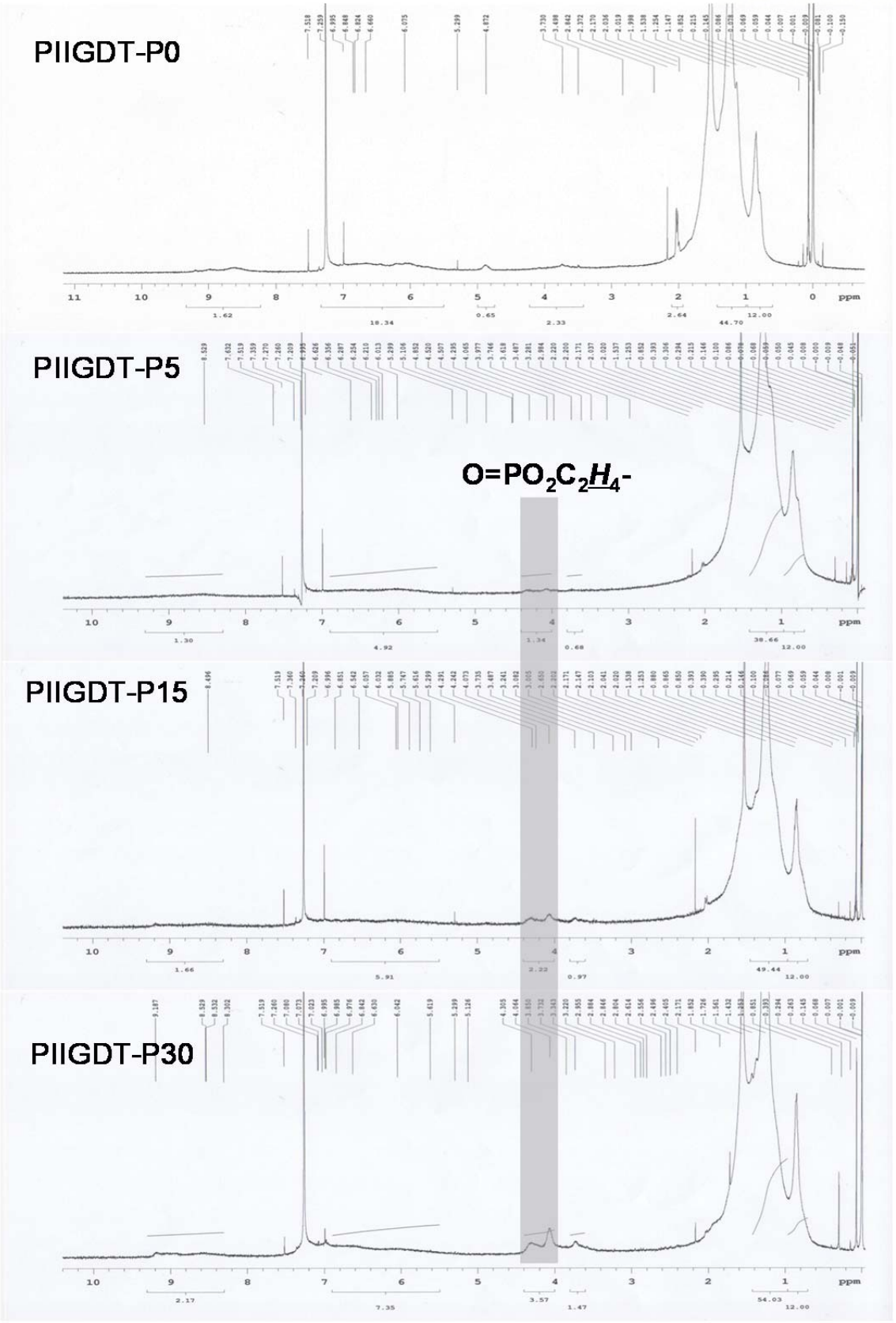

Figure 4.1. ^{1}H NMR result of PIIGDT-Pns

In order to substantiate the interfacial effect of the phosphonate groups, contact angle measurements were performed for PIIGDT-Pn-coated films. Changes in the surface energy of the films are manifested as a change in the wetability of the films, and can be quantified as changes in the contact angle. Images showing contact angles are reported in Figure 4.3. The series of polymers shows a clear decrease in contact angle with increasing PIIGDT-P0 (100.6°) >P5 (96.6°) >P15 (93.5°) >P30 (87.5°), confirming the increase in polarity of the polymer surface and suggesting improved compatibility with ionic metal oxides.

Optical and Electrochemical Properties UV-Vis spectra of the four polymers in chloroform solution and as spin-coated films on glass substrates are shown in Figure 4.4. The spectroscopic data for the polymers is summarized in Table 4.1. All polymers in both solution and thin films show a broad absorption that covers the range of 400 to 770 nm with a peak centered at ~700 nm. We noticed that the absorption peaks of the all polymers are almost identical, indicating that the incorporation of phosphonate side chains has a negligible effect on the polymer's optical properties. In addition, no red-shift was observed between their absorption spectra in solution and in the solid state, which implies that a certain degree of packing has already been formed even in the diluted solution.

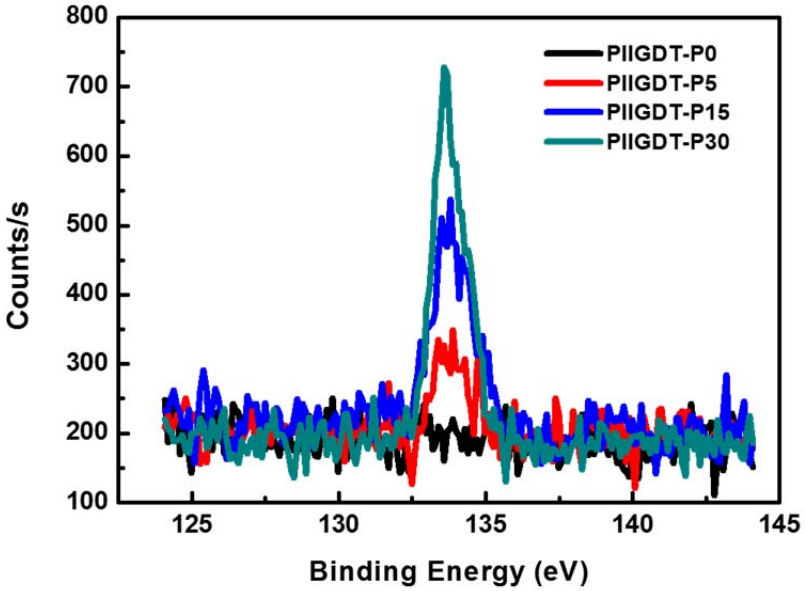

Figure 4.2. XPS spectra of the polymers showing the P 2p region.

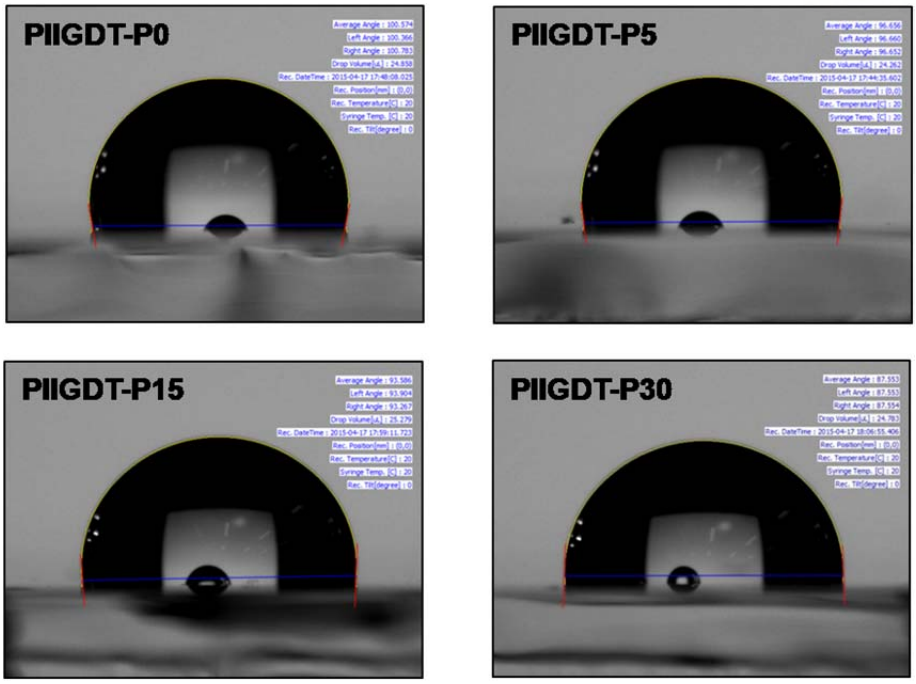

Figure 4.3. Water contact angle of PIIGDT-Pn films.

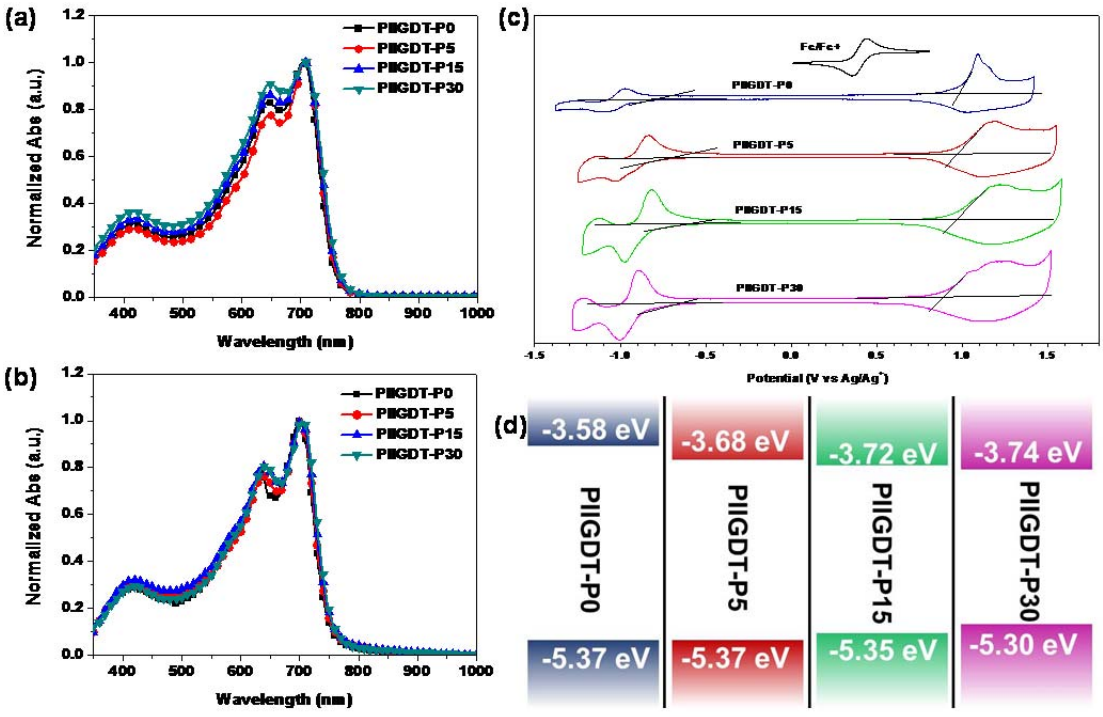

Figure 4.4. Normalized UV-Vis absorption spectra in (a) chloroform solution and (b) thin films, (c) cyclic voltammograms and (d) HOMO and LUMO energy diagrams (vs. vacuum) of PIIGDT-P0, PIIGDT-P5, PIIGDT-P15 and PIIGDT-P30.

The frontier molecular orbital energies (E_{HOMO} and E_{LUMO}) were determined using cyclic voltammetry (CV) measurements; the results are shown in Figure 4.4 and summarized in Table 4.1. Detailed conditions used for the measurements are given in Experimental Section, while their respective E_{HOMO}s and E_{LUMO}s (versus vacuum) are schematically illustrated in Figure 4.4. It appears that the phosphonate side-chain substitution exhibited a minor influence on the E_{HOMO} levels, as the oxidation potential decreased slightly with increasing phosphonate content, leading to calculated E_{HOMO} levels which increased from -5.37 eV to -5.30 eV with increasing substitution. In order to confirm this trend, the ionization potential (IP, |HOMO|) of the PIIGDT-Pn polymers was measured by ultraviolet photoelectron spectroscopy (UPS) indicating a very slight shift in IP from 5.54 eV to 5.50 eV for PIIGDT-P0 to PIIGDT-P30 (Table 4.1), consistent with the trend observed in the CV data. The increase in E_{HOMO} energy is also consistent with a decrease in V_{OC} for polymers with increasing phosphonate content, which is discussed later in the manuscript. Although the phosphonate groups are not directly attached to the conjugated π-system of the polymer backbone, the presence of phosphonate groups may affect the packing of the polymer backbone in the thin film state leading to a subtle influence on the energy bands; similar effects have been observed where the branching position in long aliphatic alkyl chains has slightly influenced energy levels via changes in the packing of conjugated polymer films.[22, 23]

Table 4.1. Optical and electrochemical properties of polymers.

	$\lambda_{max,sol}$ (nm)	$\lambda_{max,film}$ (nm)	E_{HOMO} (eV)[a]	E_{LUMO} (eV)[a]	E_g^{elec} (eV)[b]	IP[c]
PIIGDT-P0	705	700	-5.37	-3.56	1.81	5.54
PIIGDT-P5	708	702	-5.37	-3.57	1.80	5.52
PIIGDT-P15	707	704	-5.35	-3.58	1.77	5.51
PIIGDT-P30	708	706	-5.30	-3.57	1.73	5.50

[a]Thin films in CH_3CN/n-Bu_4NPF_6, versus Fc/Fc^+ at 0.1 Vs^{-1}. HOMO and LUMO estimated from the onset oxidation and reduction potentials, respectively, assuming the absolute energy level of ferrocene/ferrocenium to be 4.8 eV below vacuum. [b]E_g^{elec} (eV) = −(LUMO − HOMO). [c]Measured by an ambient ultraviolet photoelectron spectroscopy (UPS) technique.

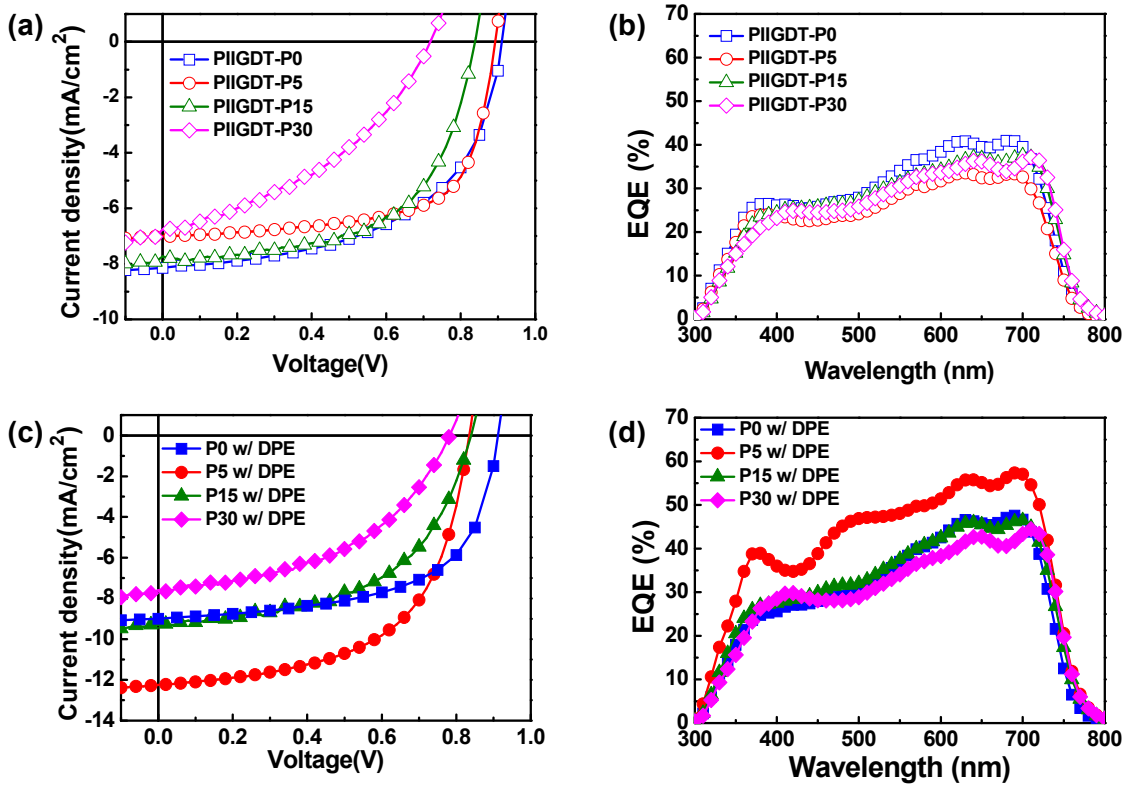

Figure 4.5. (a),(c) *J–V* characteristics of optimized i-PSCs without and with DPE additive, respectively and (b),(d) corresponding external quantum efficiency (EQE) spectra of the i-PSCs.

Photovoltaic Performance Single-junction BHJ i-PSCs were fabricated using PIIGDT-P0, PIIGDT-P5, PIIGDT-P10, or PIIGDT-P30 as the donor material in the active layer by spin-coating of a 1:1 polymer:$PC_{71}BM$ mixture from either chlorobenzene (CB) or *o*-dichlorobenzene (DCB). The architecture used was ITO (150 nm)/ZnO (60 nm)/polymer:$PC_{71}BM$/MoO_3 (5 nm)/Ag (80 nm) and tested under simulated 100 mW/cm^2 AM1.5G illumination. Device fabrication details are given in the Experimental Section. Devices were optimized by adjusting solvents, additives and material concentrations.

Solvent additives, such as 1,8-diiodooctane (DIO) additive have been shown to help optimize the blend morphology in many BHJ PSCs with fullerene derivatives.[24-29] In this work, we investigated diphenylether (DPE) as an additive, which proved more effective than DIO for all of our IIG-based polymers:$PC_{71}BM$ blends. Together with the representative devices without processing additives, the current density-voltage (*J-V*) curves of the best-performing cells and corresponding external quantum efficiency (EQE) spectra are shown in Figure 4.5. Their open-circuit voltages (V_{OC}), short-circuit currents (J_{SC}), fill factors (*FF*), and PCEs are summarized in Table 4.2. The devices without additives show a PCE of 4.06%, 4.17%, 3.87%, and 1.96% for PIIGDT-P0, PIIGDT-P5, PIIGDT-P15, and

PIIGDT-P30, respectively; the rather poor PCE for PIIGDT-P30 could be partially due to the marginal solubility and poor film quality during the BHJ films casting process from both CB and DCB.

Table 4.2. Photovoltaic performance of the IIGDT-based polymers[a]

Polymer	Additive[b]	J_{SC} (mA/cm^2)	V_{OC} (V)	*FF*	PCE_{best}(avg)[c] (%)	*Cal.* J_{SC} (mA/cm^2)
PIIGDT–P0	None	8.15	0.91	0.55	4.06 (3.82)	7.86
	DPE	9.01	0.91	0.61	5.00 (4.78)	8.71
PIIGDT-P5	None	7.00	0.89	0.67	4.17 (4.10)	6.60
	DPE	12.26	0.84	0.58	5.95 (5.85)	11.45
PIIGDT-P15	None	7.72	0.85	0.60	3.87 (3.56)	7.47
	DPE	9.24	0.85	0.55	4.30 (4.19)	9.04
PIIGDT-P30	None	6.77	0.72	0.40	1.96 (1.76)	7.20
	DPE	7.60	0.78	0.47	2.81 (2.72)	8.42

[a]Devices were measured under irradiation of AM 1.5G at 100 mW/cm^2 with inverted structure (ITO / ZnO / polymer:$PC_{71}BM$ (1:1) added DPE(additive) / MoO_3 (5nm) / Ag (80nm)). [b]3 % (v/v) Diphenylether (DPE) in chlorobenzene (CB). [c]Average values are reported in parentheses for 10 devices tested.

The PCEs of the films based on each polymer increased when 3% (v/v) DPE was used as a processing additive. The change of PCEs is mainly due to the improved J_{SC}s. In particular, a PCE of 5.95% was observed using PIIGDT-P5 which showed a large increase in J_{SC} upon processing with DPE, which is nearly 20% higher than the non-modified IIGDT polymer control device. EQE spectra confirmed the improved photocurrent generation efficiency of devices made with PIIGDT-P5 relative to the others. All J_{SC} values calculated from integration of external quantum efficiencies (EQEs) of the devices agreed within 10% of the J_{SC}s obtained from the *J-V* measurements (Figure 4.5); small differences between the J_{SC} values obtained during *J-V* measurement and EQE measurement can be attributed to spectral differences and temporal instabilities between the solar simulators, different light intensities used for each measurement and small variations in the illuminated device area. Although small amounts of phosophonate incorporation were observed to improve J_{SC}s, comparing the photovoltaic

parameters of the series indicates that the presence of phosphonate groups imposes an overall negative impact on both the V_{OC}*s* and *FFs* on the devices. It should be noted that polar interfacial layers such as conjugated polyelectrolytes or polyethylenimines[30, 31] typically have the effect of increasing V_{OC}s and *FF*s when deposited as discrete layers, via the formation of interfacial dipoles. One therefore might expect an increase in V_{OC}s and/or *FF*s when polar phosphonate groups are appended to the photovoltaic polymer, however, it appears that there is no beneficial interfacial dipole effect when polar phosphonate groups are distributed throughout the active layer.

At present, we presume that introducing a certain amount of polar, pendant phosphonate groups to the conjugated polymer has a beneficial effect on the active layer/MO interface, since the polymers otherwise possess the same structural features (almost similar absorptions and energy levels) and the observed increase in J_{SC} is consistent with improved charge collection efficiency as charge carriers are able to cross the organic/inorganic interface more readily.

Despite an improvement in J_{SC} with moderate phosphonate loading, the polymers with a large phosphonate content, *i.e*., PIIGDT-P15 and PIIGDT-P30, exhibited a less pronounced improvement in photovoltaic performance when the solvent additive DPE was used, as both polymers showed a lower PCE than the reference polymer, PIIGDT-P0. This implies that for PIIGDT-P15 and PIIGDT-P30, 'building in' optimal morphology induced by DPE in BHJ films is not as apparent as that of PIIGDT-P5, which could be attributed to the relatively lower solubility as the polar phosphonate group content increased. In order to gain a more precise and comprehensive picture of structure-property relationship in this system, we have conducted additional experiments to characterize the morphology, structural ordering and carrier transport in this series of polymers.

Charge Transport and Extraction Properties To investigate the vertical carrier transport properties of the devices, the space-charge limited current (SCLC) model was used to quantify hole mobilities in hole-only diodes (ITO/PEDOT:PSS/polymer:$PC_{71}BM$/Au) and electron mobilities in electron-only diodes (FTO/polymer:$PC_{71}BM$/Al) for each of the optimized devices with DPE additive. The SCLC plots and a summary of carrier mobilities included in the Figure 4.6 and Table 4.3, respectively. Interestingly, the electron mobilities were observed to increase (7.5×10^{-4} to 9.9×10^{-4} cm^2/Vs), while hole mobilities decreased (8.9×10^{-5} to 5.7×10^{-5} cm^2/Vs) with increasing phosphonate content. Relatively balanced charge transport ($\mu_{electron}/\mu_{hole}$ ratio of ~8) was observed for the reference polymer PIIGDT-P0. The ratio, however, became increasingly large with increasing phosphonate content due primarily to a decrease in hole mobility. Although the phosphonate chains facilitated electron transport and collection, mismatched $\mu_{electron}/\mu_{hole}$ ratio and low μ_{hole} values are consistent with the observed decrease in *FF* for high phosphonate content. For comparison, hole-only diodes were

prepared using the pure polymers. These devices yielded hole mobilities of 1.5×10^{-5}, 1.0×10^{-5}, 1.2×10^{-6} and 9.0×10^{-7} cm^2/Vs for P0, P5, P15 and P30, respectively, showing the same trend observed for the blend films with slightly somewhat lower absolute values.

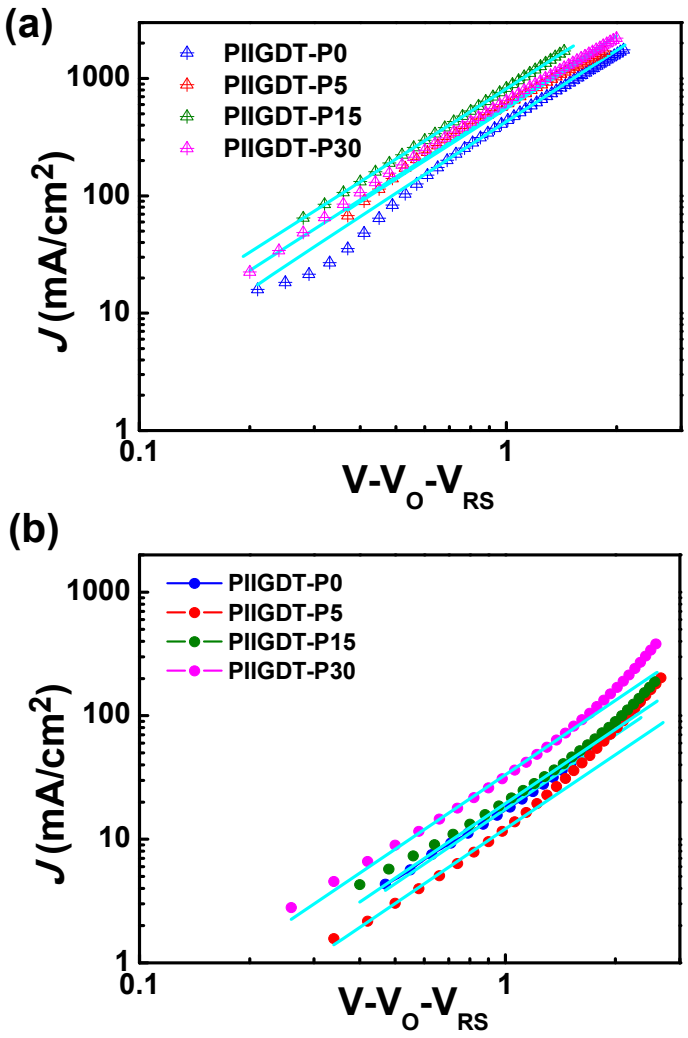

Figure 4.6. (a) hole-only devices (ITO /PEDOT:PSS/polymer:$PC_{71}BM$ added DPE/Au) (b) Double-logarithmic plot of dark *J–V* characteristics from electron-only devices (FTO/polymer:$PC_{71}BM$ added DPE/Al). Sky blue lines are fits of the curves using the Mott-gurney relationship.

Table 4.3. Hole and electron mobilities of blend films of IIGDT-based polymers derived using the SCLC method.

Polymer	Electron mobility (cm^2/Vs)	Hole mobility (cm^2/Vs)	μ_e/μ_{hole}
PIIGDT-P0	7.5×10^{-4}	8.9×10^{-5}	8.43
PIIGDT-P5	9.5×10^{-4}	6.9×10^{-5}	13.77
PIIGDT-P15	9.5×10^{-4}	6.5×10^{-5}	14.62
PIIGDT-P30	9.9×10^{-4}	5.7×10^{-5}	17.37

To further understand the movement of charge carriers for four optimized PSCs based the materials, we analyzed the light intensity dependence of the *J-V* characteristics in order to quantify recombination and charge extraction processes within the solar cells. Inverted PSCs based on PIIGDT polymers were characterized under various illumination intensities in range of 10 to100 mW/cm^2.

The dependence of J_{SC} on light intensity can be used to determine if the J_{SC} is limited by bimolecular recombination and/or trap-assisted recombination. By fitting photocurrent plots with Equation 4.1, where I is the light intensity, information about bimolecular recombination and space charge accumulation can be obtained through the fitting parameter α.[32]

$$(J_{SC} \propto I^{\alpha}) \qquad (4.1)$$

As shown in Figure 4.7, observed J_{SC}s exhibited logarithmic light intensity dependence in agreement with Eq.4.1. α values for PIIGDT-P0 and PIIGDT-P5 are close to unity (α =1), which indicates that there is weak bimolecular recombination at short circuit, thus carriers are swept out without substantial recombination. In contrast, PIIGDT-P15 and P30 exhibited higher bimolecular recombination than that of PIIGDT-P0 and PIIGDT-P5. Although these results show marginal difference with bimolecular recombination playing a minor role in both of PIIGDT-P0 and PIIGDT-P5 devices, it may be inferred that the increased bimolecular recombination stems from poor phase separation and morphology with higher phosphonate content.

Additionally, to investigate the influence of the phosphonate-terminated non-ionic side chains on the interface between active layer and metal oxide layer, we examined the dependence of the net photocurrent (J_{ph}) on the effective applied voltage (V_{eff}), where J_{ph} is the difference between the current density under illumination and dark conditions ($J_{ph} = J_L - J_D$) and $V_{eff} = V_o - V_a$ (V_o is voltage at $J_{ph} = 0$ and V_a is applied bias voltage).[33] These results indicate correlations between the molecular

structure and compatibility of the phosphonate groups at the interface between the organic and inorganic layers arising from polar and hydrophilic properties and device performance.[34, 35]

At sufficiently high V_{eff}, photocurrent is saturated with no recombination indicating dissociation of all photogenerated excitons and collection of all photogenerated charges at the electrodes. For PIIGDT-P0, J_{ph} becomes saturated at V_{eff} = 0.26 V (Figure 4.7), indicating that bimolecular recombination and the build-up of space charges began within device under 0.26 V. The saturation voltages of PSCs with increasing phosphonate content are extended to higher effective voltages; 0.28V (PIIGDT-P5) < 0.59 V (PIIGDT-P15) < 0.65 V (PIIGDT-P30). This is likely due to the increasing difference between electron and hole mobilities and is in agreement with the carrier mobilities measured by SCLC modeling.

At the short-circuit condition, PIIGDT-P0 and P5 exhibited J_{ph}/J_{sat} ratios of 98% and 99%, respectively, where the ratio of J_{ph} and J_{sat} is the product of charge dissociation and collection probabilities,[12] assuming J_{sat} at 1.2 V_{eff}. The ratio at short-circuit condition indicates a marginal difference in exciton dissociation between PIIGDT-P0 and P5-based PSCs. Interestingly, at the maximum power output condition, PIIGDT-P5 shows higher J_{ph}/J_{sat} than PIIGDT-P0, with J_{ph}/J_{sat} ratios of 82% and 76%, respectively, indicating that PIIGDT-P5-based PSCs exhibit enhanced charge extraction and collection, likely due to the improved organic/inorganic interface. In contrast, PIIGDT-P15 and P30 showed inferior charge dissociation and collection probability due to stronger bimolecular recombination. As a result, PIIGDT-P5-based PSCs lead to the best performance via enhancement of charge diffusion and charge transport and reduced bimolecular recombination.

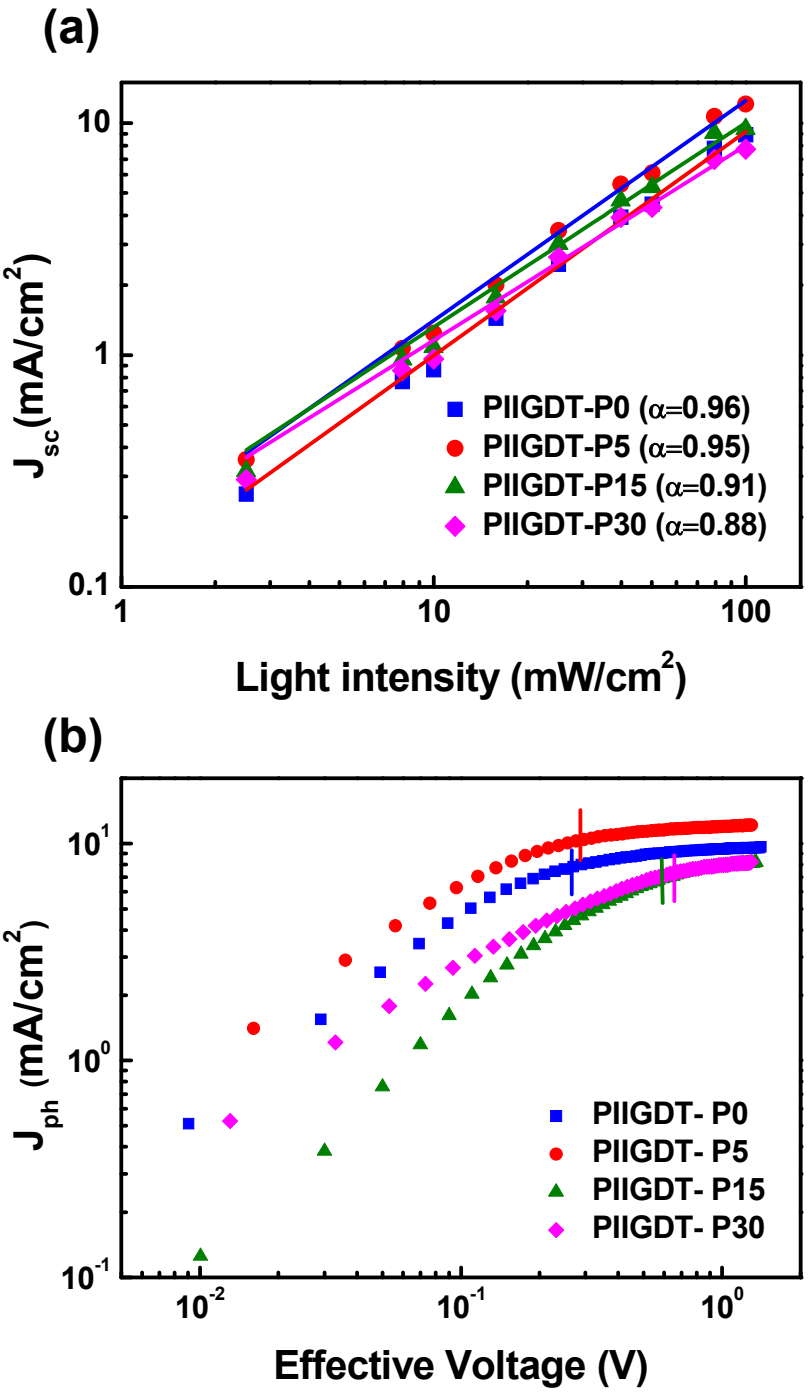

Figure 4.7. (a) Double-logarithmic scale of the short circuit current density as a function of light intensity and (b) photocurrent versus effective voltage of optimal PSCs with DPE: PIIGDT-P0 (blue), P5 (red), P15 (green) and P30 (magenta).

Thin-Film Microstructure Analyses To correlate the microstructural order in the thin film with device performance, we measured grazing-incidence wide-angle X-ray scattering (GIXD) using neat polymer films and polymer:$PC_{71}BM$ blends with and without DPE additive (Figure 4.8 and Figure 4.9). Detailed crystallographic parameters are summarized in Table 4.4.

All neat polymer films clearly exhibited multi-diffraction (*h00*) patterns up to the fourth order along the out-of-plane (q_z) axis corresponding to a highly ordered lamellar structure as well as (*010*) peaks along the in-plane (q_{xy}) axis arising from π-π stacking of the polymer backbones, which indicates preferential self-assembly into an edge-on orientation relative to the substrate surface. It is interesting to note that a new (*010*) peak along the q_z plane for PIIGDT-P0 was also observed, suggesting the co-existence of face-on and edge-on orientations. In addition, π-π stacking distances gradually shortened from PIIGDT-P0, PIIGDT-P5, PIIGDT-P15 to PIIGDT-P30 (3.85 Å to 3.65 Å). Based on these GIXD results, one concludes that the use of phosphonate side chains can cause polymers not only to adopt more organized packing among each other but also to tune a preference for polymer-packing orientation.

When IIG-based polymers were blended with $PC_{71}BM$ and spin-coated without additives, as shown in Figure 4.9, the diffraction peaks arising from the packing of the IIG-based polymers could still be distinguished, in addition to broad peaks at 1.24–1.30 $Å^{-1}$ assigned to $PC_{71}BM$. The (*010*) peaks along the q_{xy} plane are clearly visible, with intensities increasing according to the increasing amount of the phosphonate groups, while adversely affecting the (*010*) peaks along the q_z plane.

Even though the diffraction peaks in the polymer:$PC_{71}BM$ blend films processed with 3% DPE additive were observed at almost the same positions as those for the pristine polymer:$PC_{71}BM$ blends, their relative intensities became broader and weaker. This suggests that intercalation of $PC_{71}BM$ in the polymer side chains can occur upon adding DPE additive, in agreement with the device results above. Notably, in the case of PIIGDT-P5 processed with DPE, the (*010*) peak intensity is pronounced in the q_z plane with some lamellar packing in the q_{xy} direction, indicating the polymer backbones adopt a mixture of packing orientations, which in parallel should contribute to the higher PCE observed in PIIGDT-P5 system.

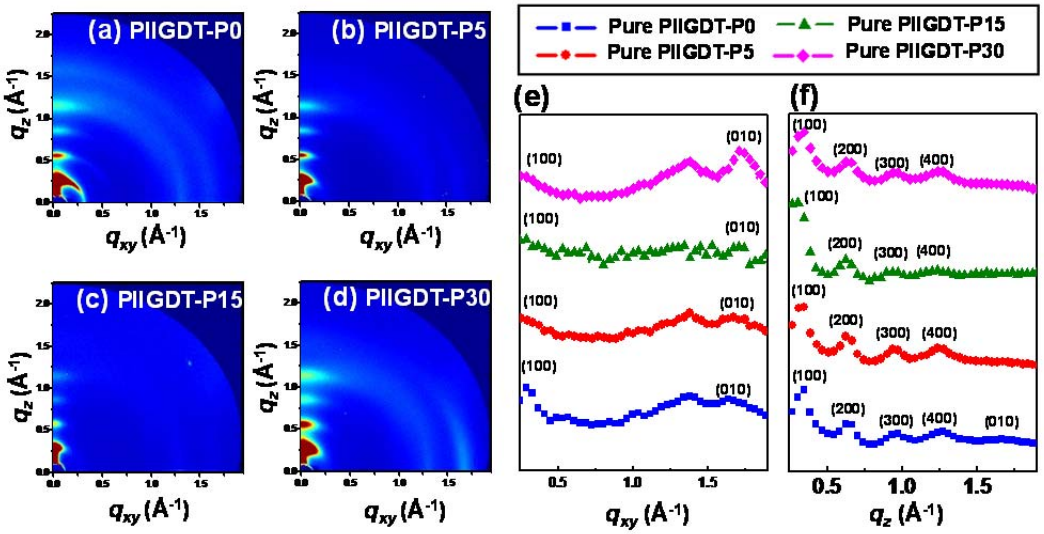

Figure 4.8. Grazing incidence wide angle X-ray scattering (GIXD) images of IIGDT-based polymer neat films: (a) PIIGDT-P0, (b) PIIGDT-P5, (c) PIIGDT-P15, (d) PIIGDT-P30. The corresponding GIXD diffractogram profiles: (e) in-plane and (f) out-of-plane GIXD patterns.

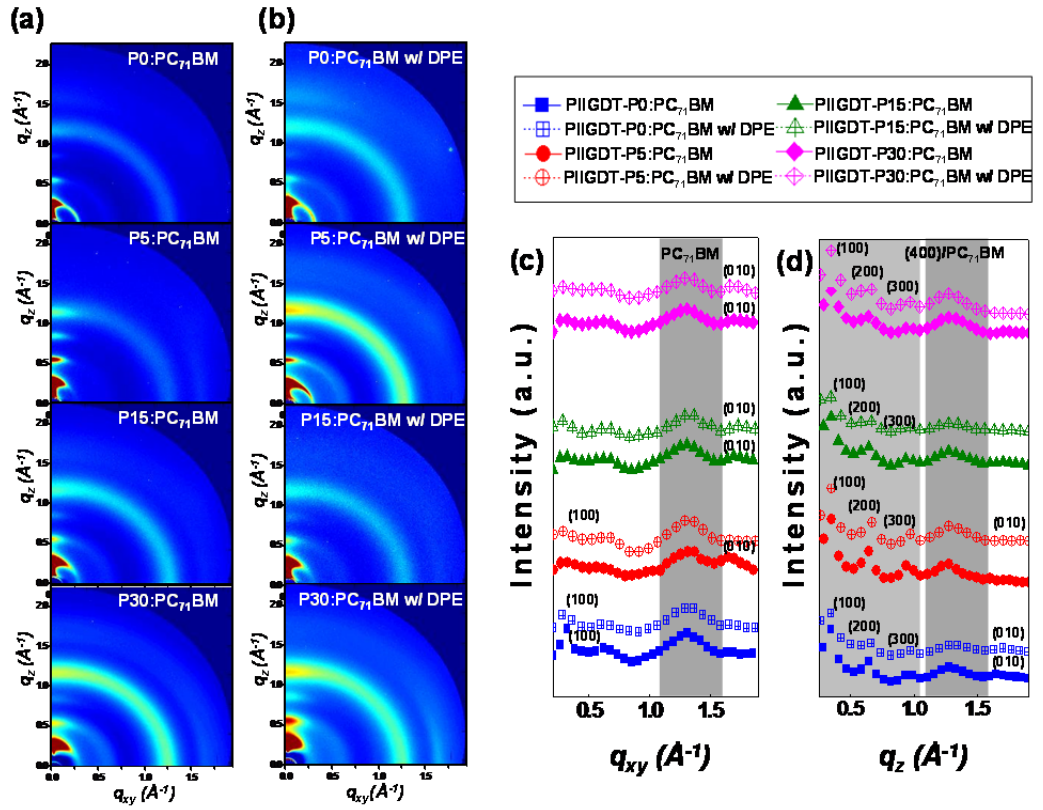

Figure 4.9. GIXD images of blended polymer films (a) without and (b) with DPE additive. Corresponding GIXD diffractogram profiles of (c) in-plane and (d) out-of-plane GIXD patterns. Solid lines represent polymer:$PC_{71}BM$ blends while dotted lines represent polymer:$PC_{71}BM$ blends processed with DPE.

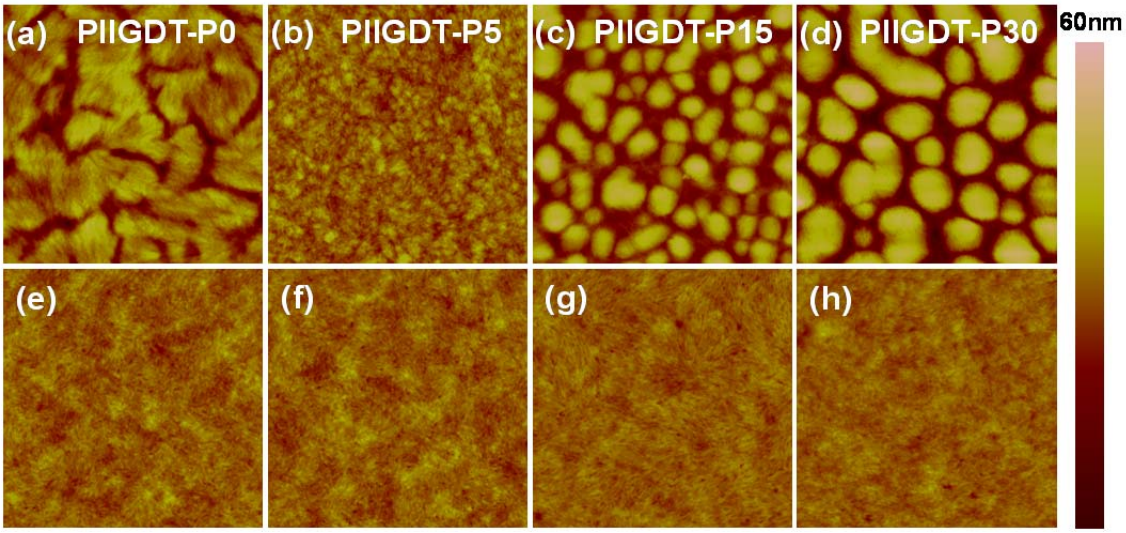

Figure 4.10. AFM images (3μm×3μm) of blended polymer:$PC_{71}BM$ films {(a) – (d)} without and {(e) – (f)} with DPE additive films. RMS values: (a) 5.21 nm, (e) 2.72 nm of PIIGDT-P0; (b) 2.55 nm, (f) 2.34 nm of PIIGDT-P5; (c) 8.18 nm, (g) 2.26 nm of PIIGDT-P15; (d) 11.14 nm, (h) 2.43 nm of PIIGDT-P30.

The surface morphologies of the polymer:$PC_{71}BM$ blends with and without DPE additive were measured by tapping-mode atomic force microscopy (AFM) (Figure 4.10). Topography images show the presence of rather large 'holes' for the blend films without DPE additive, which increase with phosphonate content. Their formation mechanism could be related to the increased hydrophilic nature with large phosphonate content. However, when the films were processed with DPE additive, despite the slightly different root mean roughness (RMS) values of these four polymers, a multi-length-scale phase-separated morphology was found for all cases, as evidenced by uniform fibrillar features. The smooth and homogeneous films processed with DPE are beneficial for obtaining large BHJ interface areas, which is also consistent with the J_{SC} and EQE spectra observed for the related solar cell devices.

Table 4.4. Crystallographic parameters calculated from GIXD profiles of IIGDT-based polymers.

Polymer	Crystallographic parameters				
	Axis	π-π stack [$Å^{-1}$]	d-spacing [Å]	Lamella stack [$Å^{-1}$]	d-spacing [Å]
Neat PIIGDT-P0	q_{xy}	1.63	3.85	0.31	20.33
	q_z	1.69	3.72	0.33	19.04
PIIGDT-P0:$PC_{71}BM$	q_{xy}	-	-	0.30	20.81
	q_z	1.70	3.70	0.34	18.48
PIIGDT-P0:$PC_{71}BM$ w/ DPE	q_{xy}	-	-	0.31	20.27
	q_z	1.70	3.70	0.34	18.48
Neat PIIGDT-P5	q_{xy}	1.67	3.76	0.28	22.44
	q_z	-	-	0.32	19.63
PIIGDT-P5:$PC_{71}BM$	q_{xy}	1.67	3.76	0.30	20.94
	q_z	-	-	0.33	19.04
PIIGDT-P5:$PC_{71}BM$ w/ DPE	q_{xy}	-	-	0.31	20.53
	q_z	1.77	3.55	0.34	18.48
Neat PIIGDT-P15	q_{xy}	1.70	3.70	0.28	22.77
	q_z	-	-	0.31	20.27
PIIGDT-P15:$PC_{71}BM$	q_{xy}	1.71	3.67	0.29	21.67
	q_z	1.75	3.59	0.33	19.04
PIIGDT-P15:$PC_{71}BM$ w/ DPE	q_{xy}	1.71	3.57	0.34	18.48
	q_z	-	-	0.33	19.04
Neat PIIGDT-P30	q_{xy}	1.72	3.65	0.27	23.53
	q_z	-	-	0.33	19.04
PIIGDT-P30:$PC_{71}BM$	q_{xy}	1.71	3.67	0.29	21.67
	q_z	-	-	0.34	18.48
PIIGDT-P30:$PC_{71}BM$ w/ DPE	q_{xy}	1.70	3.70	0.29	21.67
	q_z	-	-	0.34	18.48

4.3 Conclusions

In summary, we present a simple and effective molecular engineering strategy, via introduction of non-ionic phosphonate side chains into a given IIG-based model polymer, to induce a high compatibility at the hybrid organic/inorganic interfaces, while controlling charge transport/collection and recombination dynamics in i-PSCs. For a systematic investigation on the effect of phosphonate

side chains, a series of IIG-based statistical polymers (PIIGDT-Pn) were synthesized with varying phosphonate content (0%, 5%, 15%, and 30%). It is intriguing that despite drops in both V_{OC} and *FF* in the devices made from phosphonate-containing polymers, the use of 5% phosphonate brought about ~20% improvement in PCE relative to the non-modified reference polymer, due to a substantial increase in J_{SC}. Through a combination of detailed electrical measurements using the SCLC model, light intensity dependence, net photocurrent (J_{ph}) and film characterization (GIXD and AFM), we were able to elucidate how changes in phosphonate content influenced photovoltaic parameter. This in-depth study shows that the boost of PCEs in i-PSCs based on phosphonate-containing polymers appears to be linked to reduced non-germinate recombination and improved charge-transport/collection induced by the improved compatibility at hybrid interfaces. We highlight that this finding provides new insight into molecular design strategies that optimize charge dynamics in i-PSCs without compromising advantages provided by the photovoltaic polymer's structure.

4.4 Experimental Section

Materials and Instruments: 6,6'-(*N,N'*-2-octyldodecyl)-dibromoisoindigo (1) and diethyl(6-bromohexyl)phosphonate were synthesized according to the literature.[36-39] ^{1}H NMR and ^{13}C NMR spectra were recorded on a Varian VNRS 400 MHz (Varian USA) spectrometer using $CDCl_3$ as solvent and tetramethylsilane (TMS) as an internal reference. UV-Vis spectra were taken using a UV-1800 (SHIMADZU) spectrometer. Number-average (M_n) and weight average (M_w) molecular weights and polydispersity indices (PDI) of the polymer products were determined by gel permeation chromatography (GPC) with a Perkin-Elmer Series 200 using a series of mono disperse polystyrene standards in THF (HPLC grade) at 313 K. Cyclic voltammetry (CV) measurements were performed on an AMETEK VersaSTAT 3 with a three-electrode cell in a nitrogen bubbled 0.1 M tetra-*n*-butylammonium hexafluorophosphate (*n*-Bu_4NPF_6) solution in acetonitrile at a scan rate of 0.1 V/s at room temperature. Ag/Ag^+ (0.01 M of $AgNO_3$ in acetonitrile) electrode, platinum wire and polymer coated glassy carbon electrode were used as the reference electrode, counter electrode and working electrode, respectively. The Ag/Ag^+ reference electrode was calibrated using a ferrocene/ferrocenium redox couple as an external standard, whose oxidation potential is set at -4.8 eV with respect to zero vacuum level. The HOMO energy levels were obtained from the equation HOMO= $-(E_{ox}^{onset} - E_{(ferrocene)}^{onset} + 4.8)$ eV. The LUMO levels of polymers were obtained from the equation LUMO= $-(E_{red}^{onset} - E_{(ferrocene)}^{onset} + 4.8)$ eV.

Synthesis of 6,6'-(N,N'-hexyl-1-diethylphosphonate)-dibromoisoindigo (2): K_2CO_3 (1.97 g, 14.28 mmol) was added to a solution of 6,6'-dibromoisoindigo (2 g, 4.76 mmol) in anhydrous DMF (30 mL)

under an argon atmosphere. After 30 min, diethyl(6-bromohexyl)phosphonate (3.44 g, 11.42 mmol) was injected through a septum. The reaction mixture was stirred at 80 °C for overnight. After cooling to room temperature, water was added and extracted with ethyl acetate. The separated organic layer was washed with water and brine, then dried over $MgSO_4$ and the solvent was removed under reduced pressure. The crude product was purified by column chromatography (silica gel, ethyl acetate to 10 % methanol in ethyl acetate) to afford 2.3 g (56 %) of **2** as dark-red solid. ^{1}H NMR (400 MHz, $CDCl_3$) δ (ppm) 9.07 (d, 2H, *J*= 8.8 Hz), 7.18 (dd, 2H, J_1= 8.8 Hz, J_2= 2 Hz), 6.92 (d, 2H, *J*= 2 Hz), 4.12-4.02 (m, 8H), 3.75 (t, 4H, *J*= 7.6 Hz), 2.04-1.59 (m, 16H), 1.46-1.39 (m, 8H), 1.33-1.25 (m, 12H). ^{13}C NMR (100 MHz, $CDCl_3$) δ (ppm) 167.89, 145.82, 132.75, 131.36, 126.94, 125.35, 120.55, 111.42, 61.60, 40.25, 30.44, 27.35, 26.65, 25.07, 22.54, 16.66. Elemental Analysis: C, 50.25; H, 5.86; N, 3.26; O, 14.87; Found: C, 50.27; H, 5.88; N, 3.06; O, 14.98. MALDI-TOF-MS *m/z*: $[M]^{+\bullet}$ = 860.64; calcd, 860.55.

General procedure for synthesis of IIG-based polymers and purification through Stille coupling: In a Schlenk flask, a solution of monomers 1 (x mol), 2 (y mol), and 3 (x+y mol) in dry toluene (12 mL)/DMF (2 mL) were degassed with argon for 20 min. To this solution, tri-*o*-tolylphosphine (0.12 equiv. of 3) and $Pd_2(dba)_3$ (0.03 equiv. of 3) were added and then the reaction mixture was heated at 90 °C for 3 days. After cooling to room temperature, the solution was added dropwise into MeOH (200 mL). The crude polymer was collected and washed with with methanol (1d), acetone (1d), hexane (1d), and chloroform (1d) in a Soxhlet apparatus. The chloroform solution was concentrated and then added dropwise into MeOH. The precipitate was collected by filtration and dried under high vacuum before characterization.

PIIGDT-P0: Using the same procedure described above, a mixture of 1 (1.0 equiv.) and 3 (1.0 equiv.) was used to polymerized to give PIIGDT-P0. M_n = 71 kDa, PDI=2.21). Elemental Analysis: C, 77.99; H, 9.41; N, 2.84; S, 6.51; O, 3.25; Found: C, 77.83; H, 9.32; N, 2.79; S, 6.52; O, 3.44.

PIIGDT-P5: Using the same procedure described above, a mixture of 1 (0.95 equiv.), 2 (0.05 equiv.), and **3** (1.0 equiv.) were used to polymerized to give PIIGDT-P5. M_n = 130 kDa, PDI=5.95). Elemental Analysis: C, 77.15; H, 9.25; N, 2.86; S, 6.56; O, 3.83; Found: C, 77.19; H, 9.24; N, 2.85; S, 6.53; O, 3.85.

PIIGDT-P15: Using the same procedure described above, a mixture of 1 (0.85 equiv.), 2 (0.15 equiv.), and **3** (1.0 equiv.) were used to polymerized to give PIIGDT-P15. M_n = 98 kDa, PDI=2.68). Elemental

Analysis: C, 75.29; H, 8.94; N, 2.90; S, 6.65; O, 4.95; Found: C, 75.35; H, 8.93; N, 2.88; S, 6.54; O, 5.04.

PIIGDT-P30: Using the same procedure described above, a mixture of 1 (0.70 equiv.), 2 (0.30 equiv.), and **3** (1.0 equiv.) were used to polymerized to give PIIGDT-P30. M_n = 54 kDa, PDI=1.93). Elemental Analysis: C, 72.92; H, 8.47; N, 2.96; S, 6.78; O, 6.72; Found: C, 74.27; H, 8.52; N, 3.94; S, 5.94; O, 6.84.

Fabrication of inverted photovoltaic cells: Polymer solar cells were fabricated with an inverted structure (ITO/ZnO/polymer:$PC_{71}BM$/MoO_3/Ag). Patterned ITO glass substrates were cleaned by ultrasonic treatment in detergent, distilled water, acetone and isopropyl alcohol, then dried in an oven for overnight at 100 °C and treated with UV-ozone for 20 min to remove residues. Zinc oxide (ZnO) was deposited by spincoating a solution of diethylzinc (5 wt%) dissolved in a 1:2 mixture of toluene : tetrahydrofuran (THF) at 3000 rpm for 30 s onto cleaned ITO substrates then dried for 10 min at 110 °C in air. Subsequently, mixed solutions of polymer:$PC_{71}BM$ (1 wt% (w/w) in chlorobenzene (CB)) containing 0 – 3% (v/v) diphenylether were spin-casted on top of the ZnO film in a nitrogen (N_2) filled glove box. 5 nm MoO_3 (~0.1 Å/s) layer and 80 nm Ag (~0.6 Å/s) electrode were thermally evaporated at < 1.0×10^{-6} torr using a shadow mask (active area 13 mm^2). The current density-voltage (*J-V* curve) characteristics of the devices were measured using a Keithley 2635A source Measure unit under AM 1.5G solar irradiation at 100 mW/cm^2. EQE measurements were conducted in ambient air using an EQE system (Model QEX7) by PV measurements Inc. (Boulder, Colorado). Spectral mismatch factors were found to be 10% or less. Optimal active layer thicknesses were found to be 110, 120, 105 and 115 nm for active layers based on P0, P5, P15 and P30, respectively.

AFM characterization: An Agilent 5500 scanning probe microscope (SPM) running with a Nanoscope V controller was used to obtain AFM images of polymer thin films. AFM images were recorded in high-resolution tapping mode under ambient conditions. Premium silicon cantilevers (TESP-V2) were used with a rotated tip to provide more symmetric representation of features over 200 nm.

GIXD characterization: Grazing-incidence X-ray diffraction (GIXD) measurements were conducted at PLS-II 9A U-SAXS beamline of the Pohang Accelerator Laboratory in Korea. X-rays coming from the in-vacuum undulator (IVU) were monochromated (wavelength λ = 1.10994 Å) using a double crystal monochromator and focused both horizontally and vertically (450 (H)×60 (V) μm^2 in FWHM @ sample position) using K-B type mirrors. The GIXD sample stage was equipped with a 7-axis motorized stage for the fine alignment of sample, and the incidence angle of X-ray beam was set to be

0.13º to 0.135º for IIGDT-based polymer films and blended films. GIXD patterns were recorded with a 2D CCD detector (Rayonix SX165) and X-ray irradiation time was 6–9 s, dependent on the saturation level of the detector. Diffraction angles were calibrated using a sucrose standard (Monoclinic, P21, a = 10.8631 Å, b = 8.7044 Å, c = 7.7624 Å, β = 102.938°) and the sample-to-detector distance was ~231 mm.

3.5 Reference

1. Chen, L. M.; Hong, Z.; Li, G.; Yang, Y. *Adv. Mater.* **2009**, *21*, 1434.
2. Xu, Z.; Chen, L. M.; Yang, G.; Huang, C. H.; Hou, J.; Wu, Y.; Li, G.; Hsu, C. S.; Yang, Y. *Adv. Funct. Mater.* **2009**, *19*, 1227.
3. Hsieh, C.-H.; Cheng, Y.-J.; Li, P.-J.; Chen, C.-H.; Dubosc, M.; Liang, R.-M.; Hsu, C.-S. *J. Am. Chem. Soc.* **2010**, *132*, 4887.
4. Hau, S. K.; Yip, H.-L.; Jen, A. K.-Y. *Polym. Rev.* **2010**, *50*, 474.
5. Liu, S.; Zhang, K.; Lu, J.; Zhang, J.; Yip, H.-L.; Huang, F.; Cao, Y. *J. Am. Chem. Soc.* **2013**, *135*, 15326.
6. Kim, G.; Yeom, H. R.; Cho, S.; Seo, J. H.; Kim, J. Y.; Yang, C. *Macromolecules* **2012**, *45*, 1847.
7. Campoy-Quiles, M.; Ferenczi, T.; Agostinelli, T.; Etchegoin, P. G.; Kim, Y.; Anthopoulos, T. D.; Stavrinou, P. N.; Bradley, D. D.; Nelson, J. *Nat. Mater.* **2008**, *7*, 158.
8. Li, G.; Chu, C.-W.; Shrotriya, V.; Huang, J.; Yang, Y. *Appl. Phys. Lett.* **2006**, *88*, 253503.
9. Sun, Y.; Seo, J. H.; Takacs, C. J.; Seifter, J.; Heeger, A. J. *Adv. Mater.* **2011**, *23*, 1679.
10. Chen, Z.; Zhang, H.; Yu, W.; Li, Z.; Hou, J.; Wei, H.; Yang, B. *Adv. Energy Mater.* **2013**, *3*, 433.
11. Meyer, J.; Khalandovsky, R.; Görrn, P.; Kahn, A. *Adv. Mater.* **2011**, *23*, 70.
12. Murase, S.; Yang, Y. *Adv. Mater.* **2012**, *24*, 2459.
13. Xie, F.; Choy, W. C.; Wang, C.; Li, X.; Zhang, S.; Hou, J. *Adv. Mater.* **2013**, *25*, 2051.
14. Irwin, M. D.; Servaites, J. D.; Buchholz, D. B.; Leever, B. J.; Liu, J.; Emery, J. D.; Zhang, M.; Song, J.-H.; Durstock, M. F.; Freeman, A. J. *Chem. Mater.* **2011**, *23*, 2218.
15. Steirer, K. X.; Ndione, P. F.; Widjonarko, N. E.; Lloyd, M. T.; Meyer, J.; Ratcliff, E. L.; Kahn, A.; Armstrong, N. R.; Curtis, C. J.; Ginley, D. S. *Adv. Energy Mater.* **2011**, *1*, 813.
16. Stubhan, T.; Li, N.; Luechinger, N. A.; Halim, S. C.; Matt, G. J.; Brabec, C. J. *Adv. Energy Mater.* **2012**, *2*, 1433.

17. Terán-Escobar, G.; Pampel, J.; Caicedo, J. M.; Lira-Cantú, M. *Energy Environ. Sci.* **2013**, *6*, 3088.

18. Stubhan, T.; Ameri, T.; Salinas, M.; Krantz, J.; Machui, F.; Halik, M.; Brabec, C. J. *Appl. Phys. Lett.* **2011**, *98*, 253308.

19. Cho, N.; Schlenker, C. W.; Knesting, K. M.; Koelsch, P.; Yip, H. L.; Ginger, D. S.; Jen, A. K.-Y. *Adv. Energy Mater.* **2014**, *4*, DOI: 10.1002/aenm.201301857.

20. Hoven, C. V.; Yang, R.; Garcia, A.; Crockett, V.; Heeger, A. J.; Bazan, G. C.; Nguyen, T.-Q. *Proc. Natl. Acad. Sci. U.S.A.* **2008**, *105*, 12730.

21. Qi, J.; Zhou, X.; Yang, D.; Qiao, W.; Ma, D.; Wang, Z. Y. *Adv. Funct. Mater.* **2014**, *24*, 7605.

22. Mei, J.; Bao, Z. *Chem. Mater.* **2013**, *26*, 604.

23. Lei, T.; Dou, J. H.; Pei, J. *Adv. Mater.* **2012**, *24*, 6457.

24. Woo, C. H.; Beaujuge, P. M.; Holcombe, T. W.; Lee, O. P.; Fréchet, J. M. *J. Am. Chem. Soc.* **2010**, *132*, 15547.

25. Peet, J.; Kim, J.; Coates, N. E.; Ma, W. L.; Moses, D.; Heeger, A. J.; Bazan, G. C. *Nat. Mater.* **2007**, *6*, 497.

26. Lee, J. K.; Ma, W. L.; Brabec, C. J.; Yuen, J.; Moon, J. S.; Kim, J. Y.; Lee, K.; Bazan, G. C.; Heeger, A. J. *J. Am. Chem. Soc.* **2008**, *130*, 3619.

27. Moon, M.; Walker, B.; Lee, J.; Park, S. Y.; Ahn, H.; Kim, T.; Lee, T. H.; Heo, J.; Seo, J. H.; Shin, T. J.; Kim, J. Y.; Yang, C. *Adv. Energy Mater.* **2015**, DOI: 10.1002/aenm.201402044.

28. Dutta, G. K.; Kim, T.; Choi, H.; Lee, J.; Kim, D. S.; Kim, J. Y.; Yang, C. *Polym. Chem.* **2014**, *5*, 2540.

29. Lee, K. C.; Song, S.; Lee, J.; Kim, D. S.; Kim, J. Y.; Yang, C. *ChemPhysChem* **2014**, *16*, 1305.

30. Choi, H.; Park, J. S.; Jeong, E.; Kim, G. H.; Lee, B. R.; Kim, S. O.; Song, M. H.; Woo, H. Y.; Kim, J. Y. *Adv. Mater.* **2011**, *23*, 2759.

31. Khan, T. M.; Zhou, Y.; Dindar, A.; Shim, J. W.; Fuentes-Hernandez, C.; Kippelen, B. *ACS Appl. Mater. Interfaces* **2014**, *6*, 6202.

32. Kyaw, A. K. K.; Wang, D. H.; Gupta, V.; Leong, W. L.; Ke, L.; Bazan, G. C.; Heeger, A. J. *ACS Nano* **2013**, *7*, 4569.

33. He, Z.; Zhong, C.; Huang, X.; Wong, W. Y.; Wu, H.; Chen, L.; Su, S.; Cao, Y. *Adv. Mater.* **2011**, *23*, 4636.

34. Huang, F.; Wu, H.; Cao, Y. *Chem. Soc. Rev.* **2010**, *39*, 2500.

35. Sun, J.; Zhu, Y.; Xu, X.; Lan, L.; Zhang, L.; Cai, P.; Chen, J.; Peng, J.; Cao, Y. *J. Phys. Chem. C* **2012**, *116*, 14188.

36. Taffa, D.; Kathiresan, M.; Walder, L. *Langmuir* **2009**, *25*, 5371.

37. Catel, Y.; Degrange, M.; Le Pluart, L.; Madec, P. J.; Pham, T. N.; Picton, L. *J. Polym. Sci. A Polym. Chem.* **2008**, *46*, 7074.

38. Lei, T.; Cao, Y.; Fan, Y.; Liu, C.-J.; Yuan, S.-C.; Pei, J. *J. Am. Chem. Soc.* **2011**, *133*, 6099.

39. Kim, G.; Han, A.-R.; Lee, H. R.; Lee, J.; Oh, J. H.; Yang, C. *Chem. Commun.* **2014**, *50*, 2180.

Chapter 5 Acknowledgements

First of all, I gratefully thank my supervisor Prof. Changduk Yang, who gave me encouragement and compliment during master-Ph. D combined course at UNIST. Particularly, under his management, I have learned organic synthesis and various organic materials for optoelectronic application and fundamental knowledges of organic chemistry. Furthermore, he has not only guided me for research in Ph. D course, but also cultivates my personality. I am also thankful and would like to acknowledge my committee members, Prof. Jin Young Kim, Prof. Joon Hak Oh, Prof. Kwanyong Seo and Prof. Jiseok Lee. They are devoted guidance and support including professional discussions and collaboration opportunities.

Finally, I would like to thank ATOMS members for their supports during my master-Ph. D combined degree. As I thought, I successfully finished my Ph. D degree with many other helps and advices from professors, friends, colleagues and family. My thanks go to our Lab. “ATOMS” members including Kyu Cheol Lee and Kwang Hyun Park as eldest brothers, ShanShan Chen, Tanya Kumari, reliable manager Sang Myeon Lee, good technician Jungho Lee, and junior members such as So-Huei Kang, Yujin An, Daehee Han, Hyejin Cho Byongkyu Lee, Min Kyu Jeong and Yongjoon Cho, additionally my research colleagues and collaborated group members such as Dr. Bright Walker, Seyeong Song, Taehyo Kim, Hye Rim Yeom (Prof. Jin Young Kim’s Lab.), A-Reum Han, Hae Rang Lee (Prof. Joon Hak Oh’s Lab.), Dr, Seok-Ju Kang, Won-Tae Park (Prof. Yong Young Noh’s Lab.) and Prof. Tae Joo Shin. In addition, I would like to express my thanks to Dr. Yiho Kim, Dr Jonggi Kim, Dr. Junghoon Lee, Ms. Boram Kim as alumna from our Lab.

In the end, I really appreciate my father, mother, brother and relative.

I would like to really thank everyone once more.

감사의 글

처음으로, 지금까지 많은 관심과 애정으로 많은 지도편달을 해주신 저의 지도교수님이신 양창덕 교수님께 큰 감사를 드립니다. 잦은 실수와 연구의 실패에도 불구하고 사제의 연을 넘어서 아버지 같은 지도는 이후에도 잊지 않고 간직하도록 하겠습니다. 학문적 지식의 전달이나 연구의 지도가 아닌 한 사람으로서의 가르침은 다른 이에게도 널리 전달토록 하겠습니다. 저의 목표를 존중해주시고 그에 맞은 길을 제시해 주셨고, 개성에 맞는 연구 분야를 선정해 주시며 모든 실험적 지식과 기술을 전달해 주신 점 또한 가슴 깊이 새겨서 더욱 발전토록 하겠습니다.

제가 학위를 무사히 마칠 수 있도록 옆에서 많은 도움과 지원을 아끼지 않은 우리 연구실 구성원들께도 많은 감사 인사를 드립니다. 형임에도 불구하고 저에게 많은 존중을 해주며 의견을 들어주신 규철이형, 광현이형, 지금도 열심히 연구실 구성원들을 위해 불철주야로 희생하는 상면이, 지금 옆엔 없지만 항상 잘 따라주던 정호, 슬슬 자리를 잡아가면서 연구실을 이끌 대희, 묵묵히 책임감 있게 옆에서 연구하는 소희, 똑 부러지게 연구를 진행하는 유진이, 항상 웃는 혜진이, 지금은 아프지만 학문적으로 많은 도움을 주고받는 병규, 소소하게 웃음을 주며 매사에 최선을 다하는 민규, 뿐만 아니라, 중국에서 유학 와서 힘듦에도 웃으면서 항상 열심히 하는 Chen, 인도에서 유학 와서 소자 제작과 이론에 많은 지식을 공유한 Tanya, 그리고 용준이까지 모두에게 이 글을 빌려 감사의 인사를 전합니다.

항상 웃음으로 지도교수님 못지않은 조언과 충고해주신 김진영 교수님, 지금은 떨어져 계시지만 뵐 때마다 정확한 조언을 아끼지 않으신 오준학 교수님, 박사학위 심사하며 좋은 조언과 지도해 주신 서관용 교수님, 바쁘신 와중에도 뵐 때마다 친근하게 지도해 주신 이지석 교수님께 감사의 인사를 드립니다. 그리고 공동연구를 진행하면서 수시로 지도편달 해주신 동국대학교 노용영 교수님, 학부 때부터 많은 관심 주시던 백종범 교수님, 언제나 웃음으로 맞이해주신 송명훈 교수님, 언제나 편안하게 맞이하여 주시던 박수진 교수님께도 진심으로 감사 드립니다. 마지막으로 힘들 때 옆에서 같이 밤늦게까지 연구하시면 많은 조언과 도움을 마다하지 않으셨던 부경대 장동욱 교수님께도 진심으로 감사

드립니다.

또한, 좋은 연구를 진행할 수 있게 도와준 김진영 교수님 연구실에 Bright Walker 박사님, 태효형, 혜림이, 세영이, 오준학 교수님 연구실에 한아름, 이해랑, 장문정, 김효은, 노용영 교수님 연구실에 강석주 박사님과 박원태, 이 밖에도 항상 옆에서 꾸준히 도와준 백종범 교수님 연구실에 인엽이형, 현정이, 서윤이, 정민이, 선민이, 송현곤 교수님 연구실 영훈이형, 송명훈 교수님 연구실에 보람이형, 신현석 교수님 연구실에 동기 동우에게도 진심으로 감사 드립니다.

그리고 항상 주위에서 응원해준 기영이, 승로, 명흠이, 수현이, 병혁이도 고등학교 때부터 함께 해주어서 정말로 감사 드립니다. 대학교 재학시절 힘들 때 기쁠 때 함께해준 오산이형, 정훈이형, 영재형, 준형이형, 주현이형, 세범이형, 순철이형, 상문이형도 학번과 나이가 어림에도 항상 친구처럼 동기처럼 옆에서 있어줘서 정말로 감사합니다.

마지막으로 사랑하는 가족들에게도 감사의 마음을 전합니다. 아들의 요구를 흔쾌히 수용하시어 박사 과정을 무사히 마칠 수 있게 도와주신 부모님, 지금은 자랑스런 동생 용식이 그리고 친척들께 머리 숙여 감사 드립니다.

Appendix

Publication List

- First author
  - ✓ Kim, G. et al. Control of Charge Dynamics via Use of Non-Ionic Phosphonate Chains and Their Effectiveness for Inverted Structure Solar Cells. Adv. Energy Mater. DOI: 10.1002/aenm.201500844 (2015)
  - ✓ Kim, G. et al. A Thienoisoindigo-Naphthalene Polymer with Ultra-High Mobility of 14.4 cm2/V·s That Substantially Exceeds Benchmark Values for Amorphous Silicon Semiconductors. J. Am. Chem. Soc. 136, 9477 (2014)
  - ✓ Kim, G. et al. Use of Heteroaromatic spacers in Isoindigo-Benzothiadiazole Polymers for Ambipolar Charge. Phys. Chem. Chem. Phys. DOI: 10.1039/C4CP01787K (2014)
  - ✓ Kim, G. et al. Acceptor-Acceptor Type Isoindigo-Based Copolymers for High-Performance n-Channel Field-Effect Transistors. Chem. Commun. 50, 2180 (2014)
  - ✓ Kim, G. et al. An unprecedented [5,6]-Open Adduct via a Direct Benzyne-C60 Cycloaddition. Tetrahedron 69, 7354 (2013)
  - ✓ Kim, G. et al. Easily Attainable Phenothiazine-Based Polymers for Polymer Solar Cells: Advantage of Insertion of S, S-dioxides into its Polymer for Inverted Structure Solar Cells. Macromolecules 45, 1847 (2012)
- Co-author
  - ✓ Kim, Y. et al. A Balanced Face-on to Edge-on Texture Ratio in Naphthalene Diimide-Based Polymers with Hybrid Siloxane Chains Directs Highly Efficient Electron Transport. Macromolecules 48, 5179 (2015)
  - ✓ Kim, J. et al. Ambipolar Semiconducting Polymers with pi-Spacer Linked Bis-Benzothiadiazole Blocks as Strong Accepting Units. Chem. Mater. 26, 4933 (2014)
  - ✓ Lee. J. et al. Synthesis and photophysical properties of five-membered ring π-conjugated materials based on bisthiazol-2-yl-amine and their metal complexation studies. Tetrahedron 66, 9440 (2013)

- Patent (Korea)
  - ▪ Prof. Changduk Yang and Gyoungsik Kim. 표면 말단이 기능화된 그라파이트, Diels-Alder반응을 통한 그라파이트 표면 말단 기능화 방법 및 이의용도
  - ▪ Registration Number: 101262515
  - ▪ Registration Date: May 02, 2013

Permission from all cited journal in this dissertation (printed permission with font style and size change)

Chapter 1 *Macromolecules* 2012, **45**,1847

Copyright Clearance Center RightsLink®

Home | Account Info | Help | Live Chat

ACS Publications
Most Trusted. Most Cited. Most Read.

Title: Easily Attainable Phenothiazine-Based Polymers for Polymer Solar Cells: Advantage of Insertion of S,S-dioxides into its Polymer for Inverted Structure Solar Cells

Author: Gyoungsik Kim, Hye Rim Yeom, Shinuk Cho, et al

Publication: Macromolecules

Publisher: American Chemical Society

Date: Feb 1, 2012

Copyright © 2012, American Chemical Society

Logged in as:
Gyoungsik Kim
Account #:
3000981114
LOGOUT

PERMISSION/LICENSE IS GRANTED FOR YOUR ORDER AT NO CHARGE

This type of permission/license, instead of the standard Terms & Conditions, is sent to you because no fee is being charged for your order. Please note the following:

- Permission is granted for your request in both print and electronic formats, and translations.
- If figures and/or tables were requested, they may be adapted or used in part.
- Please print this page for your records and send a copy of it to your publisher/graduate school.
- Appropriate credit for the requested material should be given as follows: "Reprinted (adapted) with permission from (COMPLETE REFERENCE CITATION). Copyright (YEAR) American Chemical Society." Insert appropriate information in place of the capitalized words.
- One-time permission is granted only for the use specified in your request. No additional uses are granted (such as derivative works or other editions). For any other uses, please submit a new request.

BACK | CLOSE WINDOW

Chapter 2.1 *Chem. Commun.*, 2014, **50**, 2180 (printed permission with font style and size change)

Acceptor–acceptor type isoindigo-based copolymers for high-performance n-channel field-effect transistors

G. Kim, A. Han, H. R. Lee, J. Lee, J. H. Oh and C. Yang, *Chem. Commun.*, 2014, **50**, 2180
DOI: 10.1039/C3CC48013E

Chapter 2.2 *Phys. Chem. Chem. Phys.*, 2015, **17**, 26512

Use of heteroaromatic spacers in isoindigobenzothiadiazole polymers for ambipolar charge transport

G. Kim, A. Han, H. R. Lee, J. H. Oh and C. Yang, *Phys. Chem. Chem. Phys.*, 2015, **17**, 26512
DOI: 10.1039/C4CP01787K

Chapter 3 *J. Am. Chem. Soc.*, **2014**, *136*, 9477

Chapter 4 *Adv. Energy Mater.*, **2015**, DOI: 10.1002/aenm.201500844